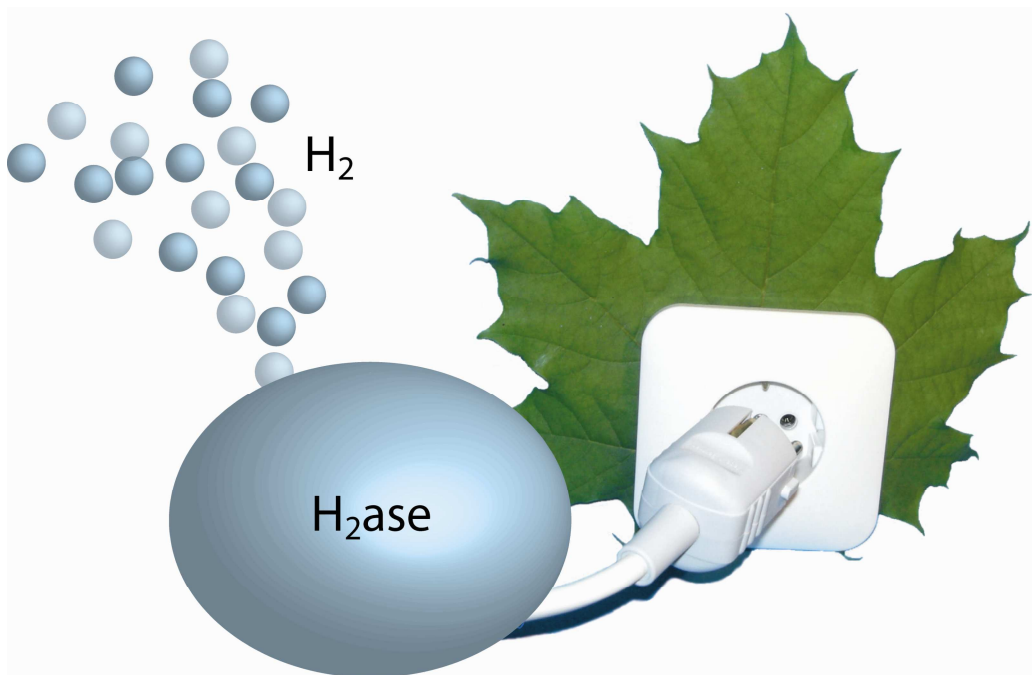


# Biomimetic Hydrogen Production



THESIS

Submitted in fulfilment of the requirements for the degree of Doctor of  
Science (Dr. rer. nat.) at Bielefeld University

Henning Krassen

May 2009

**Ph.D. Thesis**

**“Biomimetic Hydrogen Production”**

Submitted by: Henning Krassen

First Assessor: Prof. Dr. Joachim Heberle

Second Assessor: Prof. Dr. Thomas Koop

*One of the grand challenges of twenty-first century chemistry  
is to convert abundant energy-poor molecules to energy-rich molecules  
using sunlight as the energy source.*

*Harry B. Gray, California Institute of Technology*

*(Nature Chemistry Vol.1, April 2009)*

---

# Table of Contents

<b>1</b>	<b>Abstract</b>	<b>1</b>
<b>2</b>	<b>Introduction</b>	<b>3</b>
2.1	Energy supply and climate problem	3
2.2	Learning from nature: photosynthesis & hydrogen production	3
2.2.1	Photosynthesis	3
2.2.2	Hydrogenases	5
2.3	The perfect cycle	7
2.4	Objectives	8
2.4.1	Conversion of electrical into chemical energy	8
2.4.2	Direct coupling of photosynthesis and hydrogen production	8
<b>3</b>	<b>Materials and methods</b>	<b>9</b>
3.1	Protein purification	9
3.1.1	[FeFe]-Hydrogenase from <i>Chlamydomonas reinhardtii</i>	9
3.1.2	[NiFe]-Hydrogenase from <i>Ralstonia eutropha</i>	9
3.1.3	Photosystem I from <i>Synechocystis PCC 6803</i>	11
3.1.4	Cytochrome c oxidase from <i>Rhodobacter sphaeroides</i>	11
3.2	<i>In vitro</i> activity of hydrogenases (in solution)	12
3.3	Modification of gold surfaces	12
3.3.1	Ni-NTA-terminated surface	13
3.3.2	Protein immobilization	13
3.3.3	Reconstitution in a lipid bilayer	14
3.3.4	Modification of the protocol for different monitoring techniques	15
3.4	Fourier transform infrared spectroscopy	16
3.4.1	Transmission setup	16
3.4.2	Attenuated total reflection setup	17
3.4.3	Surface-enhanced infrared absorption spectroscopy	18
3.5	UV/Vis spectroscopy	22
3.6	Surface plasmon resonance	22
3.7	Electrochemistry	23
3.7.1	Cyclic voltammetry	24
3.7.2	Amperometry	25
3.8	Gas chromatography	26

---

3.9	Atomic force microscopy	27
3.10	Scanning near-field infrared microscopy	29
<b>4</b>	<b><u>Results and discussion</u></b>	<b>31</b>
4.1	Electrocatalytic surface for hydrogen production	31
4.1.1	Immobilization of the [FeFe]-hydrogenase	31
4.1.2	Electro catalytic activity	35
4.1.3	Specific activity of immobilized [FeFe]-hydrogenase	41
4.1.4	Monolayer-mediated electron transfer	45
4.1.5	Hydrogen evolution potential	57
4.1.6	Conclusions	58
4.2	Coupling of hydrogen production and photosynthesis	59
4.2.1	Assembly of photosystem I and [NiFe]-hydrogenase	60
4.2.2	Quantification of the hybrid complex	64
4.2.3	Functional testing - Photocurrent	65
4.2.4	Light-induced hydrogen evolution	69
4.2.5	Hydrogen evolution potential	70
4.2.6	Mimic the native environment	71
4.2.7	Conclusions	73
4.3	Spatially-resolved analysis of a protein monolayer	75
4.3.1	Model system “Cytochrome c oxidase”	76
4.3.2	Topography	78
4.3.3	Near-field imaging	80
4.3.4	Conclusions	84
4.4	Structural investigation of the H-cluster	85
4.4.1	Marker bands of the H-cluster	85
4.4.2	Structural changes during hydrogen production	90
4.4.3	Conclusions	93
<b>5</b>	<b><u>Concluding discussion</u></b>	<b>94</b>
5.1	Hydrogenase as electrocatalyst	94
5.2	Coupling of photosynthesis and hydrogen production	95
5.3	Structural investigation of protein monolayers	96
<b>6</b>	<b><u>References</u></b>	<b>97</b>
<b>7</b>	<b><u>Acknowledgements</u></b>	<b>111</b>
<b>8</b>	<b><u>Curriculum vitae</u></b>	<b>113</b>

---

<b>9</b>	<b>Supplementary information</b>	<b>114</b>
9.1	Sample changer for transmission setup	114
9.2	Anaerobic SEIRAS setup	118
<b>10</b>	<b>Lists</b>	<b>122</b>
10.1	List of Tables	122
10.2	List of Figures	122
10.3	List of Abbreviations	125

# 1 Abstract

Hydrogenases catalyze the reduction of protons to molecular hydrogen with outstanding efficiency. An electrode surface which is covered with active hydrogenase molecules becomes a promising alternative to platinum for electrochemical hydrogen production.

To immobilize the hydrogenase on the electrode, the gold surface was modified by heterobifunctional molecules. A thiol headgroup on one side allowed the binding to the gold surface and the formation of a self-assembled monolayer. The other side of the molecules provided a surface with a high affinity for the hydrogenase *CrHydA1* from *Chlamydomonas reinhardtii*. With methylviologen as a soluble energy carrier, electrons were transferred from carboxy-terminated electrodes to *CrHydA1* and conducted to the active site (H-cluster), where they reduce protons to molecular hydrogen. A combined approach of surface-enhanced infrared absorption spectroscopy, gas chromatography, and surface plasmon resonance allowed quantifying the hydrogen production on a molecular level. Hydrogen was produced with a rate of  $85 \text{ mol H}_2 \text{ min}^{-1} \text{ mol}^{-1}$ . On a 1'-benzyl-4,4'-bipyridinium (BBP)-terminated surface, the electrons were mediated by the monolayer and no soluble electron carrier was necessary to achieve a comparable hydrogen production rate (approximately 50% of the former system). The hydrogen evolution potential was determined to be -335 mV for the BBP-bound hydrogenase and -290 mV for the hydrogenase which was immobilized on a carboxy-terminated mercaptopropionic acid SAM. Therefore, both systems significantly reduce the hydrogen production overpotential and allow electrochemical hydrogen production at an energy level which is close to the commercially applied platinum electrodes (hydrogen evolution potential of -270 mV).

In order to couple hydrogen production and photosynthesis, photosystem I (PS1) from *Synechocystis PCC 6803* and membrane-bound hydrogenase (MBH) from *Ralstonia eutropha* were bound to each other. To accomplish tight binding of both proteins the PS1 subunit PsaE was genetically fused to the C-terminal end of the small subunit of MBH, i.e. close to the electron acceptor site of MBH. This fusion protein spontaneously assembled with the PsaE-deletion mutant of PS1. Crucial for a high hydrogen evolution rate of the system is an efficient electron transfer between both proteins. To allow this measurement, the PsaE-deletion mutant of PS1 was immobilized on a Ni-NTA-terminated monolayer via a genetically introduced His-tag. The specificity of the assembly of fusion protein and deletion mutant was verified by SEIRAS. Surface plasmon resonance, gas chromatography and electrochemistry complemented this

measurement and yielded the specific activity of the functional hybrid complex:  $4500 \text{ mol H}_2 \text{ min}^{-1} \text{ mol}^{-1}$ . The investigated complex allowed hydrogen evolution at potentials up to 85 mV, i.e. hydrogen production at a lower energy level than on a platinum electrode.. In addition, the hydrogen production rate was higher than for hydrogenase-modified electrodes without PS1.

Beyond these specific results, the experimental setup can be used to quantify the hydrogen evolution rate on a molecular level for variable hydrogenases and hybrid complexes. This information will be used to choose the most efficient catalysts for introduction into the native system for *in vivo* hydrogen production.



## 2 Introduction

### 2.1 Energy supply and climate problem

Our future energy supply is one of the grand challenges of the twenty-first century, if not the greatest. Available fossil fuels will be consumed within decades and we need alternative energy sources to maintain life as we know it.

In addition, burning fossil fuels means to produce the greenhouse gas carbon dioxide. The world's energy requirement will increase along with population growth and industrialization of emerging nations. If we use fossil fuels to provide this energy, the carbon dioxide concentration in the atmosphere will dramatically increase and cause strong global warming (Hellwig et al., 2009). Only renewable energy sources will satisfy the growing global energy demand without creating severe environmental problems.

Our sun is the largest and longest-lasting energy source. It has the potential to power our planet with solar fuels (Gray, 2009). A promising approach is to use Nature's catalytic converter of solar energy into chemical energy - the photosynthetic apparatus (Jordan et al., 2001) converts solar energy into biomass with a rate of  $90 \text{ TJ s}^{-1}$  in total (Alivisatos et al., 2004). 20% of this energy would be sufficient to meet the world's current energy requirement of about  $5 \times 10^{20} \text{ J year}^{-1}$  (EIA, 2008).

### 2.2 Learning from nature: photosynthesis & hydrogen production

During evolution, nature figured out how to use abundant metallic elements to activate small molecules (Gray et al., 2000). These metallocenters are embedded in their protein cages and form highly specific catalysts – most times more efficient than any catalyst we can produce.

#### 2.2.1 Photosynthesis

Photosynthesis is subdivided into light and dark reaction. In the light reaction, nicotinamide adenine dinucleotide phosphate ( $\text{NADP}^+$ ) is reduced to NADPH, oxygen is produced, and protons are pumped through a membrane. The proton-motive force is used by the ATP-synthase to generate energy-rich adenosine triphosphate (ATP). While eight photons are absorbed, 1  $\text{O}_2$ , 2 NADPH, and 3 ATP are formed. In the dark

reaction (Calvin cycle) ATP and NADPH are used for carbon fixation. CO<sub>2</sub> is converted into hexoses and other organic compounds (Berg et al., 2003; Doenecke et al., 2005).

Electron transfer during the light reaction (Figure 1) is important within the scope of this work and described in detail.

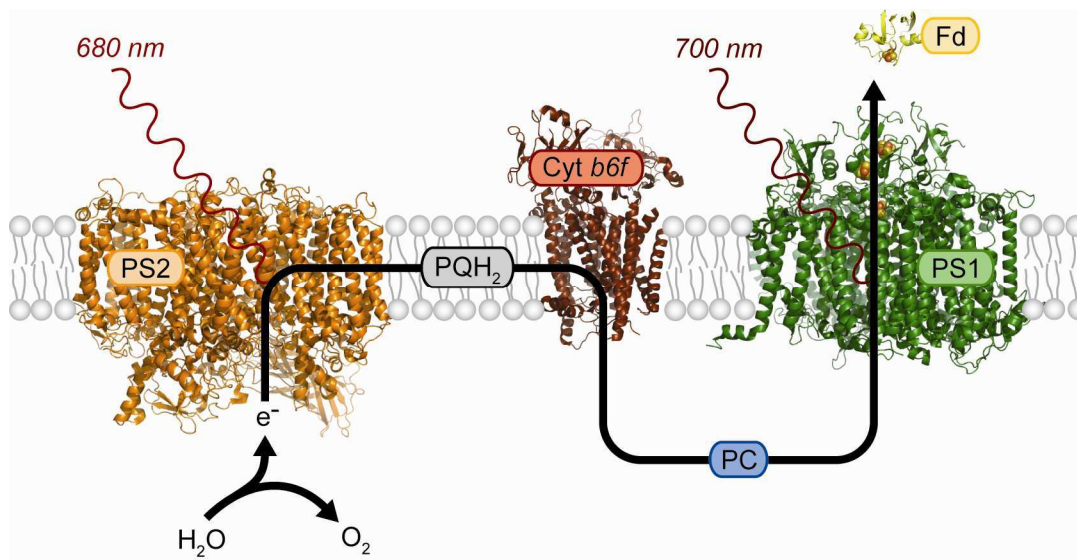


**Figure 1** *Light reaction of photosynthesis* | Water is oxidized to oxygen by photosystem II (PS2, PDB ID: 1S5L). The obtained electrons are transferred via plastoquinol (PQH<sub>2</sub>) to cytochrome b6f (Cyt b6f, PDB ID: 2ZF9). Plastocyanin (PC) transports the electrons to photosystem I (PS1, PDB ID: 1JB0), where they reduce ferredoxin (Fd, PDB ID: 1A70). During the catalytic cycle of PS1 and PS2 red light is absorbed.

Two large protein complexes, photosystem I (PS1) and photosystem II (PS2), are the major parts of the photosynthesis apparatus. PS2 catalyzes the first step of the light reaction, the reduction of plastoquinone (PQ) to plastoquinol (PQH<sub>2</sub>), see equation (1). Water oxidation provides the required electrons.

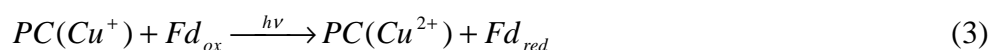


Upon absorption of a photon, a so-called “special pair” of chlorophyll *a* molecules (P680) transfers an electron to pheophytin (Ph, a porphyrin derivate without central metal ion). The electron is conducted from Ph to a bound PQ at Q<sub>A</sub>-position and further towards an exchangeable PQ at Q<sub>B</sub>-position. P680<sup>+</sup> is a strong oxidant and removes an electron from water, which is bound to the manganese cluster. The cycle is repeated and a second electron is used for the second reduction of the exchangeable PQ. PQH<sub>2</sub> dissociates from PS2 and is oxidized by the cytochrome *b6f* complex. The electrons are

used to reduce the copper protein plastocyanin (PC), see equation (2). The protons are released on the luminal side of the membrane and contribute to the proton-motive force.



PS1 catalyzes the terminal step of the light reaction. PC is oxidized and the electron is transferred to ferredoxin (Fd), a soluble 2Fe-2S protein, see equation (3).



The electron acceptor site of PS1 is the special pair of chlorophyll *a* molecules (P700) with a redox potential of +0.44 V (Webber et al., 2006). Absorption of a 700 nm photon leads to a charge separation. An electron is transferred via a chlorophyll molecule at A<sub>0</sub> position and a quinone at A<sub>1</sub> position to an arrangement of 4Fe-4S clusters. The electron donor site of PS1 consists of the two clusters F<sub>A</sub> and F<sub>B</sub> which have a redox potential of -0.54 V and -0.59 V, respectively (Evans and Heathcote, 1980). From here the electron is transferred to Fd. The redox potentials of PC and Fd are +0.37 V and -0.45 V, respectively. The change of the free enthalpy of this reaction is +79.1 kJ mol<sup>-1</sup>. The driving force of this reaction is the absorption of a 700 nm photon, which provides energy of 171 kJ mol<sup>-1</sup> (Berg et al., 2003).

The ferredoxin-NADP<sup>+</sup>-reductase transfers the electron from Fd to NADP<sup>+</sup>, which is consumed in various metabolic pathways.

### 2.2.2 Hydrogenases

Hydrogenases catalyze the reduction of protons to molecular hydrogen (Adams et al., 1980). They are widely distributed among anaerobic living bacteria and some eukaryotic unicellular organisms (Horner et al., 2002).

Most of these enzymes are iron-sulfur proteins, which contain two metal atoms at their active site, either two iron atoms (as in [FeFe]-hydrogenases) (Peters et al., 1998; Nicolet et al., 1999) or one iron and one nickel (as in [NiFe]-hydrogenases) (Volbeda et al., 1995; Higuchi et al., 1997). Here, the structure of the active site of the former ones is described in detail (see below) as a basis for the later investigation of the [FeFe]-hydrogenase CrHydA1 from *Chlamydomonas reinhardtii* (Chapter 4.4). Advantages and disadvantages of both hydrogenase families are discussed.

### Active site of [FeFe]-hydrogenases

Based on the two initial structural reports of [FeFe]-hydrogenases and FTIR studies (Pierik et al., 1998) a consensus model of the active site (H-cluster) could be built (Nicolet et al., 2000).

Both iron centers are ligated by a CO and a CN<sup>-</sup> molecule, respectively. The CO ligands are located in hydrophobic pockets, whereas the CN<sup>-</sup> ligands form hydrogen bonds with the protein network. The two iron centers are bridged by one CO molecule and two sulfurs. The bridging sulfurs belong to a small organic molecule which was initially modelled as 1,3-propanedithiolate (Peters et al., 1998) and later as di(thiomethyl)amine. The nitrogen bridgehead atom would provide an alkaline function, which is not available in the protein environment in the vicinity of the H-cluster (Nicolet et al., 2001). This nitrogen atom could be involved in the proton transfer between H-cluster and protein surface. In *Clostridium pasteurianum* hydrogenase I for example, the bridgehead atom is located close to Cys178, which was postulated to be part of the proton transfer pathway (Peters et al., 1998).

A water molecule completes the coordination sphere of the distal “Fe2” and a cubane [4Fe4S] cluster is connected to the proximal “Fe1” via sulfur of a cysteine residue (Figure 2).

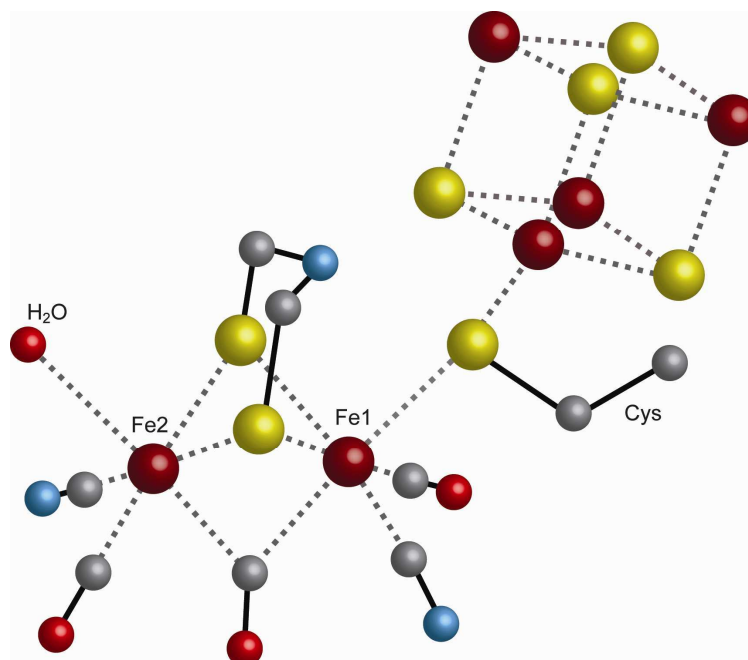


**Figure 2** Active site of [FeFe]-hydrogenases | The so-called H-cluster consists of two iron centers, which are coordinated by several ligands. The atoms are colour-coded: carbon (grey), nitrogen (blue), oxygen (red), sulfur (yellow), iron (dark red). Hydrogen atoms are not included in the scheme. See text for further details.

### *Comparison of [FeFe] and [NiFe]-hydrogenases*

[FeFe]-hydrogenases function as electron valves hence “burning” evolved reduction equivalents. They have a higher hydrogen production activity (Adams, 1990; Peters et al., 1998; Nicolet et al., 1999) and benefit from only weak product inhibition in the direction of  $H^+$  reduction (Léger et al., 2004), but they are irreversibly damaged by  $O_2$ .

Physiologically, [NiFe]-hydrogenases cleave molecular hydrogen and the hydrogen production activity *in vitro* is lower compared to [FeFe]-hydrogenases. As advantage, [NiFe]-hydrogenases are oxygen-tolerant and can be reactivated by reduction with  $H_2$  or dithionite (Cammack et al., 2001).

The structure/function relationship of both hydrogenase classes was reviewed in the literature (Fontecilla-Camps et al., 2007).

## **2.3 The perfect cycle**

The combination of photosynthesis, electrochemical hydrogen production, and fuel cells forms a so-called “perfect cycle”. This cycle of water converts solar energy into electrical energy.

One approach is to fix the biological catalysts to appropriate electrodes. Both photosystems have been used in electrochemical setups to convert light energy into electrical energy – in solid-state devices (Das et al., 2004), as surface-tethered monolayers (Badura et al., 2006; Carmeli et al., 2007) on gold nano particles (Terasaki et al., 2006), and on nanoporous gold electrodes (Ciesielski et al., 2008).

In order to store the (photo-)electrical energy as chemical energy, molecular hydrogen is considered as a high energetic fuel. Noble metals like platinum are able to reduce protons to hydrogen at the potential which is provided at the donor site  $F_A/F_B$  of PS1. Platinum nano particles were covalently linked to PS1 (in the vicinity of the donor site) and light-induced hydrogen production took place (Grimme et al., 2008).

A more efficient catalyst than noble metals is provided by nature. Hydrogenases (Vignais and Billoud, 2007) are enzymes which are able to generate hydrogen with an overpotential close (or equal) to 0 V (Armstrong and Fontecilla-Camps, 2008). This has been shown for a variety of hydrogenase enzymes including the [NiFe]-hydrogenases of *Ralstonia* species on a rotating disk graphite electrode (Goldet et al., 2008) and the [FeFe]-hydrogenases of *Desulfovibrio desulfuricans* (Vincent et al., 2005), *Clostridium acetobutylicum* (Baffert et al., 2008) and *Chlamydomonas reinhardtii* (Krassen et al., 2009).

Molecular hydrogen and oxygen are consumed in fuel cells to generate electricity with unrivalled conversion efficiency (Cammack et al., 2001; Karyakin et al., 2005) and without emission of carbon dioxide. The only product is water which was initially consumed by photosystem II.

## 2.4 Objectives

### 2.4.1 Conversion of electrical into chemical energy

The world's need for energy is basically a need for fuels. The hydrogenase *CrHydA1* from *Chlamydomonas reinhardtii* shall be used as catalyst in an electrochemical device to use electrical energy for the production of hydrogen.

The setup shall be based on a gold electrode to allow the investigation by surface-enhanced infrared spectroscopy (SEIRAS) and surface plasmon resonance (SPR). These techniques shall be used to provide detailed information about the enzyme-modified surface and about *CrHydA1* in its catalytic-active state.

### 2.4.2 Direct coupling of photosynthesis and hydrogen production

A hybrid complex of membrane-bound hydrogenase MBH from *Ralstonia eutropha* and the photosystem I from *Synechocystis PCC 6803* shall be investigated in detail. Specificity of the assembly, efficiency of the electron transfer between both proteins, and the hydrogen production rate are in the focus of this work.

The surface-bound hybrid complex shall be quantified on a molecular level. This will allow the comparison between hybrid complexes which use different hydrogenases and/or coupling strategy.

## 3 Materials and methods

### 3.1 Protein purification

#### 3.1.1 [FeFe]-Hydrogenase from *Chlamydomonas reinhardtii*

Recombinant [FeFe]-hydrogenase CrHydA1 Strep-tag<sup>exp</sup> was produced as described before (von Abendroth et al., 2008) by Sven Stripp and Gregory von Abendroth in the workgroup of Prof. T. Happe (Ruhr-Universität Bochum, Germany). Briefly, *Clostridium acetobutylicum* ATCC 824 recombinant strains were grown in CGM medium (minimum medium, containing erythromycin, calcium carbonate, iron sulfate, nickel chloride and zinc sulfate) in a 2.5 L MiniFors<sup>®</sup>-bioreactor (Infors, Augsburg, Germany) (Girbal et al., 2005; Wiesenborn et al., 1988). An optimized purification protocol was established for the heterologously synthesized CrHydA1 Strep-tag<sup>exp</sup> enzyme. Ultracentrifugation and affinity chromatography on a 10 ml Strep-Tactin Superflow<sup>®</sup> column (IBA, Göttingen, Germany) were applied. Cell growth and protein purification were carried out under strict anaerobic conditions. Isolated protein was concentrated to 5 mg ml<sup>-1</sup> on Vivaspin 6<sup>®</sup>-columns (Sartorius Stedim Biotech, Göttingen, Germany) and stored in 10 mM potassium phosphate buffer (pH 6.8), containing 10% glycerol and 2 mM sodium dithionite (Sigma-Aldrich) for stabilization. Dithionite was used to protect the hydrogenase against oxidative damage by possible oxygen contaminations. But dithionite would disturb the monolayer experiments, which are presented in this work, and had to be removed prior to use in spectroscopic or electrochemical experiments. Therefore, the sample was dialysed for 30 minutes on 0.025 µm V-series<sup>®</sup> membranes (Millipore, Schwalbach, Germany) against 10 mM sodium phosphate buffer solution (pH 6.8). During the dialysis the activity of the hydrogenase decreased by up to 80%. For later experiments (Chapter 4.1.4), the hydrogenase was purified in the absence of dithionite and used within days after the purification. This procedure maintained almost the full activity of the hydrogenase.

#### 3.1.2 [NiFe]-Hydrogenase from *Ralstonia eutropha*

Membrane-bound hydrogenase (MBH) from *Ralstonia eutropha* was purified by Alexander Schwarze in the workgroup of Prof. B. Friedrich (Humboldt-University Berlin, Germany).

### *His-tagged hydrogenase*

A His<sub>6</sub>-tag coding sequence was fused to the 3' end of *hoxK* the gene for the MBH's small subunit HoxK. *Ralstonia eutropha* cells were aerobically cultivated in mineral salt medium, containing 0.2% (w/v) fructose and glycerol, at 30 °C in a 10 L-fermenter (Biostat MD, Braun Biotech, Melsungen, Germany). The cells were harvested after 50 hours (OD<sub>436</sub> ≈ 11) by centrifugation (5,000 x g, 4 °C). The cell pellet was resuspended in 50 mM Tris-HCl buffer (pH 8.0) containing 150 mM NaCl, protease inhibitor cocktail (Roche), and DNase I (Roche). The resuspended cells were disrupted by two passages through a cooled French pressure cell (SLS Aminco, SLM Instruments, Rochester, USA). Soluble proteins were separated by ultracentrifugation (100,000 x g, 4 °C). Afterwards, membrane proteins were solubilized by the addition of 2% Triton X-114 and isolated by ultracentrifugation (100,000 x g, 4 °C). The hydrogenase was purified by affinity chromatography (Ni-NTA superflow columns, QIAGEN, Hilden, Germany) and concentrated by centrifugation (Amicon Ultra-15 (PL-30), Millipore, Billerica, USA).

### *Fusion protein of hydrogenase and photosystem I subunit PsaE*

The photosystem I subunit PsaE from *Synechocystis PCC 6803* was genetically fused to the C-terminus of HoxK, the small subunit of the MBH, thereby replacing the membrane anchor (Leu310-His360).

*Ralstonia eutropha* strains HF653 and HF768 were cultivated in mineral salt medium, containing 0.2% (w/v) fructose and glycerol, at 30 °C in flask cultures. Gene expression was induced after 24 hours by the addition of 2 mM acetoin. After a total cultivation time of 48 hours, an OD<sub>436</sub> of 8-10 was reached and the cells were harvested by centrifugation (4,000 x g, 4 °C). The cell pellet was resuspended in 50 mM Tris-HCl buffer (pH 8.0) containing 150 mM NaCl, protease inhibitor cocktail (Roche), and DNase I (Roche). The resuspended cells were disrupted by two passages through a cooled French pressure cell (SLS Aminco, SLM Instruments, Rochester, USA).

The soluble proteins were isolated by ultracentrifugation (88,000 x g, 4 °C) and applied onto a Ni-NTA superflow column (4 ml BV, QIAGEN, Hilden, Germany) to remove all His-tagged proteins. The flow-through was directly loaded onto a Strep-Tactin Superflow column (IBA, Göttingen, Germany). The fusion protein was eluted by 5 mM desthiobiotin, concentrated using a centrifugal filter device (Amicon Ultra-15 (PL-30), Millipore, Billerica, USA), and stored at -80 °C in 50 mM Tris-HCl (pH 8.0) containing 50 mM NaCl and 20% (v/v) glycerol.



### 3.1.3 Photosystem I from *Synechocystis PCC 6803*

The PsaE-depleted photosystem I (PSI<sub>ΔPsaE</sub>) was designed and purified by Alexander Schwarze in the workgroup of Prof. B. Friedrich (Humboldt University Berlin, Germany). A His<sub>10</sub>-tag was fused to the N-terminal end of the subunit PsaF. The purification of the cyanobacterial PS1 was done according to a protocol developed for PS1 from *Thermosynechococcus elongatus* (El-Mohsnawy and Rögner, will be published elsewhere) with slight modifications.

Thylakoid membranes were homogenized in 20 mM HEPES buffer (pH 7.5) containing 10 mM MgCl<sub>2</sub>, 10 mM CaCl<sub>2</sub>, 0.5 M mannitol, and 0.05% (w/v) β-dodecyl maltoside. 0.9% β-dodecyl maltoside was added and ultracentrifugation (257,000 x g, 4 °C) was applied to separate the soluble proteins from the membranes. A chelating sepharose fast flow column (GE Healthcare, Uppsala, Sweden) was charged with a 100 mM NiCl<sub>2</sub> solution containing 10% acetic acid. His<sub>10</sub>-PSI<sub>ΔPsaE</sub> complexes were eluted by a linear gradient of 1-100 mM histidine, concentrated, and dialyzed against histidine-free buffer (50 mM MES pH 6.5, 300 mM NaCl, 10 mM MgCl<sub>2</sub>, 10 mM CaCl<sub>2</sub>, 0.25 M mannitol, 0.03% β-dodecyl maltoside). The protein was further purified by a hydrophobic interaction column (Poros 50 OH, Applied Biosystems, Foster City, USA) and separated in trimeric and monomeric PSI<sub>ΔPsaE</sub> fractions by size exclusion chromatography (TSK 3000 column, LKB Instrument, Gräfelfing, Germany).

PSI<sub>ΔPsaE</sub> samples were adjusted to 3-5 μg chlorophyll ml<sup>-1</sup> (in 20 mM HEPES (pH 7.5), 10 mM MgCl<sub>2</sub>, 10 mM CaCl<sub>2</sub> and 0.03% β-dodecyl maltoside) and frozen in liquid nitrogen.

### 3.1.4 Cytochrome c oxidase from *Rhodobacter sphaeroides*

Cytochrome c oxidase from *Rhodobacter sphaeroides* was expressed and purified via Ni-NTA affinity chromatography as described before (Mitchell & Gennis, 1995; Hosler et al., 1992). Prior to use, the protein was stored at -80 °C in 50 mM potassium phosphate buffer (pH 8), which contained 0.01% β-dodecylmaltoside (Anatrace).

The enzyme concentration was determined by UV/Vis spectroscopy (Gennis et al., 1982; Chance et al., 1957). Spectra of the air-oxidized and the sodium dithionite reduced protein solution were recorded and the protein concentration was calculated, using the differential extinction coefficient  $\Delta\epsilon_{605-630} = 24 \text{ mM}^{-1} \text{ cm}^{-1}$ .

### 3.2 *In vitro* activity of hydrogenases (in solution)

1 – 10  $\mu\text{g}$  CrHydA1 was added to 2 mL of a 100 mM sodium phosphate buffer solution (pH 6.8), containing 1 mM methylviologen dichloride (MV, Sigma-Aldrich) and 100 mM sodium dithionite, to probe hydrogen evolution activity under optimal conditions. This solution was sealed gas-tight in an 8 mL glass tube, purged with argon and incubated at 37 °C for 15 minutes afterwards. The amount of produced hydrogen was measured by gas chromatography and the specific hydrogen evolution activity of the hydrogenase (in  $\mu\text{mol H}_2 \text{ min}^{-1} \text{ mg}^{-1}$ ) was calculated.

### 3.3 Modification of gold surfaces

Thiols spontaneously form a self-assembled monolayer (SAM) on a gold surface through covalent linkage to the sulfur group (Figure 3). Heterobifunctional molecules which carry a thiol group on one end and a second functional group on the other end are used to change the chemical properties of the surface.

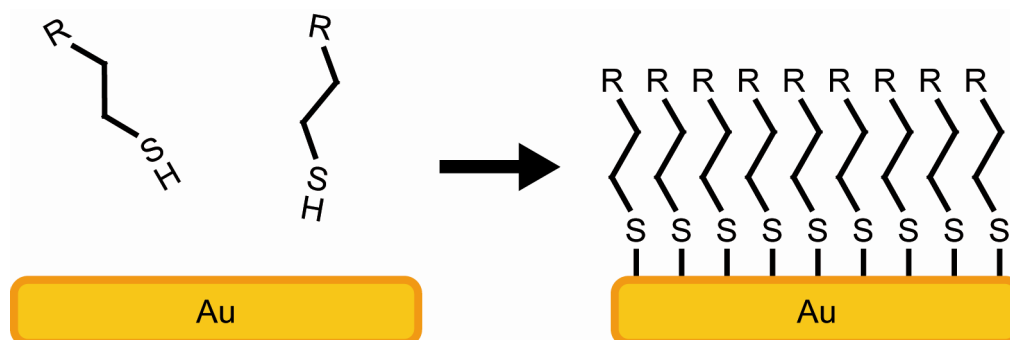


**Figure 3** *Self-assembled monolayer* | Molecules with an exposed thiol group spontaneously bind to a bare gold surface and form an oriented monolayer.

In this work, the bare gold surface was incubated with an aqueous solution of 2 mM 3-mercaptopropionic acid (MPA, Sigma-Aldrich), an ethanolic solution of 2 mM 11-mercaptoundecanoic acid (MUA, Sigma-Aldrich) (Song et al., 1993; Sun et al., 1993; Chen et al., 2002; Xu and Bowden, 2006; Jiang et al., 2008), or 1 mM 1-(10-mercaptodecyl)-1'-benzyl-4,4'-bipyridinium-dibromid (BBP) in dimethyl sulfoxide (DMSO) for 30-90 minutes to produce a carboxy-terminated surface. Surface-enhanced infrared absorption spectroscopy (SEIRAS, Chapter 3.4.3) was used to monitor the adsorption process *in situ*.

### 3.3.1 Ni-NTA-terminated surface

The gold surface was exposed to a solution of 2.5 mM dithio-bis(succinimidyl propionate) (DTSP, Sigma-Aldrich) in (waterless) DMSO for 15 minutes. The sulfur bridge was split in the vicinity of the gold surface and both thiosuccinimidyl propionates (TSP) were immobilized on the surface. The surface was washed with DMSO (3x) to remove excess DTSP and with aqueous 0.5 M potassium carbonate solution (3x) to remove the DMSO. Then, the surface was incubated with 150 mM  $N_{\alpha},N_{\alpha}$ -bis(carboxymethyl)-L-lysine (ANTA, Fluka). The succinimidyl ring of the TSP was substituted by the amino group of the lysine and a nitrilo triacetic acid monolayer was formed. After washing with double distilled water, nickel sulfate was added to a final concentration of 50 mM. The synthesis of the Ni-NTA surface was finished after 1 minute of incubation. Surface-enhanced infrared absorption spectroscopy (SEIRAS, Chapter 3.4.3) was used to monitor the single reaction steps *in situ* (Ataka et al., 2004).

### 3.3.2 Protein immobilization

Proteins were immobilized on the surface by two different approaches: (1) Electrostatic interactions were used to bind the hydrogenase CrHydA1 to carboxy- or BBP-terminated surfaces. (2) Proteins, which carried a His-tag, adsorbed to the Ni-NTA-group via the coordination of the nickel with two nitrogen of two imidazole side chains (Figure 4).

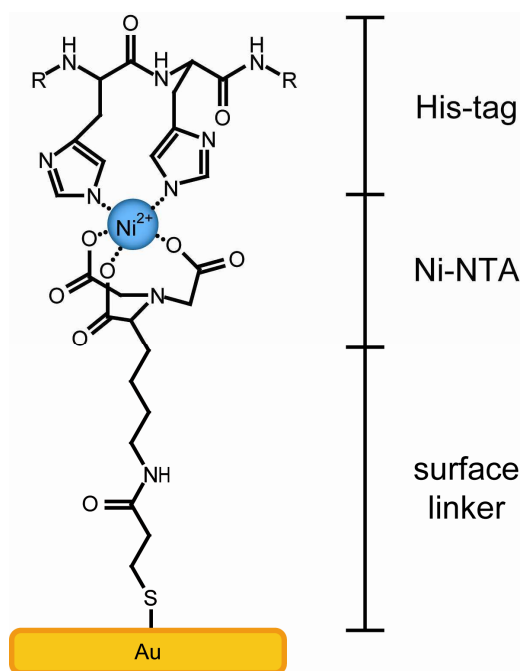


**Figure 4** His-tag binding to Ni-NTA | Two nitrogen atoms of two successive Histidin residues coordinate a nickel ion, which is tethered to the gold surface by an organic NTA linker.

In each experiment the chemically-modified electrode was incubated with the respective protein solution. The used protein concentrations for each experiment are summarized in Table 1.

Table 2 lists the used protein buffers.

Table 1 Protein binding conditions

Protein	Surface modifier	Protein concentration
<i>CrHydA1</i>	bare gold	3.5 $\mu$ M
	MPA	3.5-6 $\mu$ M
	MUA	3.5 $\mu$ M
	BBP	3.5-6 $\mu$ M
	100:1 MPA:BBP	3.5 $\mu$ M
PS1	Ni-NTA	0.5 $\mu$ M
PS1 $_{\Delta$ PsaE	Ni-NTA	0.5 $\mu$ M
PsaE	PS1 $_{\Delta$ PsaE	1.4 $\mu$ M
MBH $_{\text{PsaE}}$	PS1 $_{\Delta$ PsaE	1.4 $\mu$ M
	PS1	1.4 $\mu$ M
	Ni-NTA	1.4 $\mu$ M
MBH	Ni-NTA	2 $\mu$ M
CcO	Ni-NTA	2 $\mu$ M

Table 2 Protein buffers

Protein	Buffer
<i>CrHydA1</i>	10 mM potassium phosphate (pH 6.8) (oxygen-free)
PS1, PS1 $_{\Delta$ PsaE & PsaE	20 mM HEPES (pH 7.5) + 10 mM MgCl <sub>2</sub> +10 mM CaCl <sub>2</sub> + 0.03% (w/v) $\beta$ -dodecyl-maltosid (DDM)
MBH $_{\text{PsaE}}$ & MBH	20 mM HEPES (pH 7.5) + 1 mM MgCl <sub>2</sub> +1 mM CaCl <sub>2</sub> + 0.03% (w/v) $\beta$ -dodecyl-maltosid (DDM)
CcO	50 mM potassium phosphate (pH ) + 0.1% (w/v) $\beta$ -dodecyl-maltosid (DDM)

### 3.3.3 Reconstitution in a lipid bilayer

The membrane proteins CcO and the PsaE deletion mutant of PS1 were immobilized on a Ni-NTA-modified surface. The hydrophobic areas, which were embedded in the lipid membrane in nature, were covered with detergent molecules ( $\beta$ -dodecyl-maltoside). The surface-tethered protein layer was incubated with a solution of detergent-destabilized lipid vesicles (liposomes) of dimyristoyl-phosphatidylcholine (DMPC, Sigma-Aldrich). Upon addition of macroporous bio-beads (SM2, Bio-Rad Laboratories) the detergent

molecules were removed and the lipids spontaneously assembled around the protein to form a protein-tethered bilayer lipid membrane (Giess et al., 2004). The reconstitution process is schematically depicted in Figure 5.

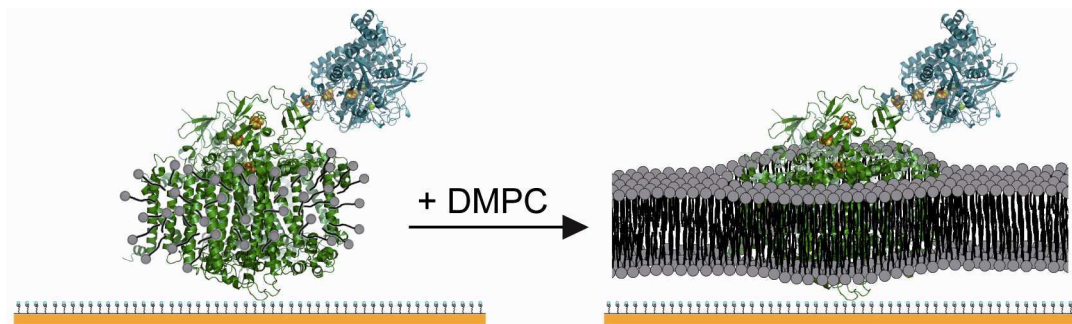


**Figure 5** *Reconstitution of a membrane protein in a lipid bilayer* | The hybrid complex of photosystem I and membrane-bound hydrogenase (PSI-MBH) is immobilized on a Ni-NTA-terminated self-assembled monolayer (SAM) via a His-Tag. Detergent molecules, which are bound to the transmembrane region of PSI, are removed by the addition of bio-beads and allow the formation of a lipid bilayer of DMPC.

### 3.3.4 Modification of the protocol for different monitoring techniques

In the surface-enhanced infrared absorption spectroscopy (SEIRAS) cell and the quartz crystal microbalance (QCM), the solution on top of the gold surface was accessible by a pipette. First, the surface was covered with the solvent for the respective modification step to allow for the measurement of background spectra (for SEIRAS) or a sufficient equilibration time (for QCM). Then, the surface modifier was added to the stated final concentration.

The surface plasmon resonance (SPR) system was equipped with a flow system. The surface was continuously rinsed with the respective solvent and the surface modifier was injected into the flow. The flow system was not certified for the use of DMSO or aqueous 0.5 M  $K_2CO_3$  solution. Therefore, the protocol for the synthesis of a Ni-NTA-modified surface had to be modified as follows: (1) A 2 mM aqueous solution of MPA was injected. (2) A hydrochloric solution (pH 4) of 5 mM 1-ethyl-3-(3-dimethylaminopropyl)carbodiimide (Sigma-Aldrich) was injected to activate the carboxy-terminated surface and allow the binding of amino groups. (3) The latter step was immediately followed by an injection of a 150 mM solution of  $N_{\alpha},N_{\alpha}$ -bis(carboxymethyl)-L-lysine (ANTA) in 0.2 M  $K_2CO_3$ . Details about the amide formation by carbodiimide in aqueous media are described in literature (Nakajima and Ikada, 1995).

### 3.4 Fourier transform infrared spectroscopy

Infrared (IR) spectroscopy provides the possibility to monitor vibrational transitions in molecules. Every vibration, which induces a change in the dipole moment, is IR-active and can be detected by this technique.

In Fourier transform infrared (FTIR) spectrometers polychromatic IR radiation is emitted by a globar. In the Michelson interferometer, the IR beam is split into two beams by a semi-reflective beam splitter. One beam is perpendicularly reflected to the fixed mirror, the other one is transmitted to the moving mirror, which induces a path length difference with respect to the other beam. Both beams are reflected back to the beam splitter where they recombine with constructive or destructive interference (depending on the path length difference). This combined IR beam passes through a sample and the light intensity is measured as a function of the mirror position by a mercury cadmium telluride (MCT) detector. The correlation between mirror position and frequency is given by the Fourier transformation. This process provides the light intensity as function of the frequency (Herres and Gronholz, 1985). In the resulting single channel spectrum, the light intensity is commonly plotted as a function of the wavenumber. The spectra, which are presented in this work, were recorded on an IFS 66v/S or a Vertex 70 (Bruker Optik GmbH, Ettlingen, Germany) FTIR spectrometer.

FTIR difference spectroscopy allows to selectively measure the vibrations, which are changed during a reaction. A reference single channel spectrum is recorded before the reaction is triggered and subtracted from a second single channel spectrum, which is measured after the reaction is finished. The bands in the resulting difference spectrum are solely attributed to changes in the molecules.

#### 3.4.1 Transmission setup

A 1  $\mu\text{L}$  droplet of a 420  $\mu\text{M}$  solution of *CrHydA1* was placed in the center of a  $\text{BaF}_2$  window and dried to a final concentration of approximately 1 mM. Vacuum grease was applied to the border area of the  $\text{BaF}_2$  and a second window was placed on top to seal the sample (Figure 6(A)). Afterwards, the sample was placed in the focus of the IR beam (Figure 6(B)). A home-made sample changer was used to exchange the sample for two stacked  $\text{BaF}_2$  windows for the reference measurement. The samples were rotated through 20 degrees with respect to the IR beam to avoid internal reflections between the  $\text{BaF}_2$  windows.

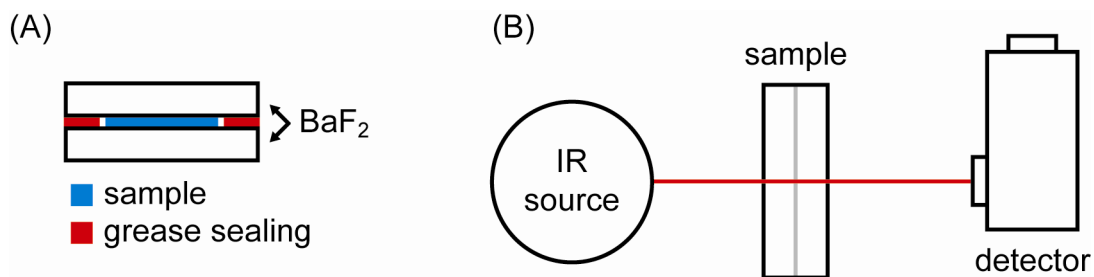


**Figure 6** *Transmission setup* | (A) The sample is placed between two BaF<sub>2</sub> windows (so called: sandwich sample) (B) Principle setup for transmission measurements.

CrHydA1 is irreversibly inhibited by oxygen and even traces of oxygen had to be avoided during sample preparation and measurement. BaF<sub>2</sub> windows, grease, sample holder and glass pipette were placed in an exsiccator and evacuated for 20 minutes. The exsiccator was filled with argon and transferred into a glove bag (Sekuroka Glove Bag, Carl Roth GmbH, Karlsruhe, Germany), which was purged with argon for 20 minutes before the exsiccator was opened. During this time, the glove bag was inflated and deflated in turns to assure complete exchange of the atmosphere. A small over pressure in the glove bag prevented the contamination with oxygen from the atmosphere during the preparation.

#### 3.4.2 Attenuated total reflection setup

In attenuated total reflection (ATR) spectroscopy the IR beam is coupled through a ZnSe crystal into an internal reflection element (IRE). The IR beam is totally reflected inside the IRE and guided towards the detector of the spectrometer. The sample is placed on top of the IRE and is probed by an evanescent IR wave (Figure 7). This wave is generated at the interface between IRE and sample and penetrates into the medium of lower refractive index with a distance of approximately one wavelength.

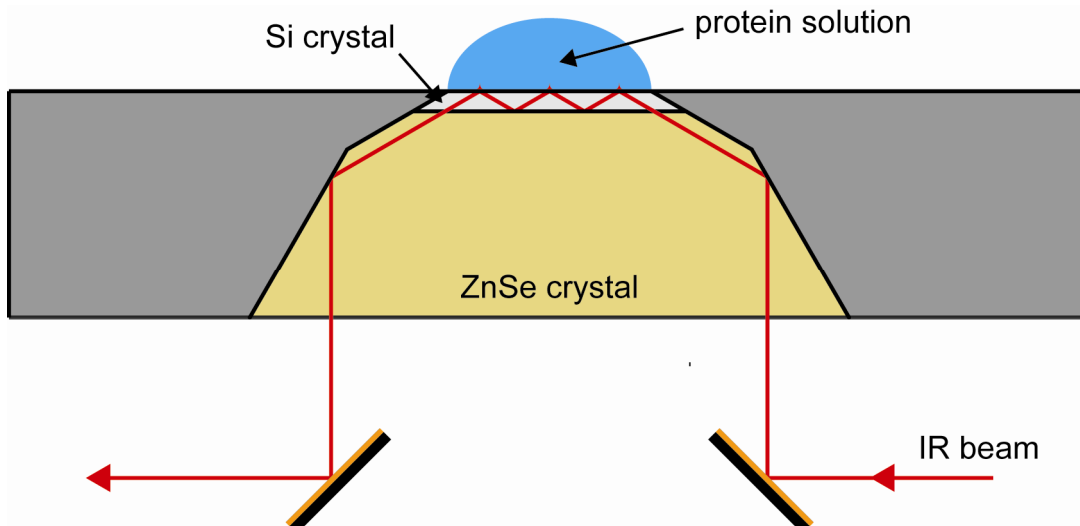


**Figure 7** *Attenuated total reflection setup* | The sample is placed on top of the internal reflection element and probed by the evanescent wave.

ATR infrared spectroscopy was used to record absorption spectra of *CrHydA1* during the drying process. Spectra of the dry crystal were measured for up to 8 minutes and stored as background. Then, approximately 50  $\mu\text{L}$  of a 0.4  $\mu\text{M}$  solution of *CrHydA1* were placed on top of the Si crystal as a droplet. The droplet was slowly dried under argon atmosphere and spectra were continuously recorded – each spectrum was averaged over a time interval of 1 minute. The ATR optics (DuraSamplIRII, Smiths, USA) were purged with argon during the measurement.

To allow the handling of the sample under anaerobic conditions a glove bag (Sekuroka Glove Bag, Carl Roth GmbH, Karlsruhe, Germany) was connected to the top of the sample chamber of the FTIR spectrometer by a home-made holder. It was continuously purged with argon to maintain oxygen-less atmosphere. The ATR optics was purged at a higher pressure to avoid the transfer of water vapour traces into the optical pathway.

### 3.4.3 Surface-enhanced infrared absorption spectroscopy

The signals of IR-absorbing molecules in the vicinity (<10 nm) of a nano-structured gold film are enhanced by a factor of approximately 100 (Anderson, 2003) – compared to the common ATR setup (Chapter 3.4.2). This enhancement allows the investigation of organic molecules and/or proteins on a (sub-)monolayer level by IR spectroscopy (Osawa et al., 1993; Ataka et al., 1996; Ataka and Osawa, 1998, 1999; Osawa, 2002).



### *Surface enhancement*

The intensity amplification in surface-enhanced IR spectroscopy (SEIRAS) results from an enhancement of the electric field in the vicinity of small, interacting gold particles which are illuminated with light close to the resonance frequency of the local surface plasmons (Moskovits, 1985). Such surface plasmons have been observed in the near and middle infrared region (4000-800  $\text{cm}^{-1}$ ) on silver island films (Osawa and Ikeda, 1991) and on ordered arrays of (silver) nanoparticles (Jensen et al., 2000). The surface plasmons coincide with the enhancement. The electromagnetic enhancement has been extensively discussed (Yang et al., 1995).

An increase in the absorption rate occurs which is proportional to the density of the electric field and the enhanced local field augments in regions where molecules are adsorbed to the surface. Size, shape and packing density of the gold particles and the dielectric function influence the local fields. Thus, the enhancement varies from point to point on the surface and the average value is detected (Aroca and Ross, 2004).

### *Surface selection rules*

The electromagnetic field produced by the local surface plasmon excitation is comprised with the electric vector perpendicular to the surface. Thus, only vibrational modes which induce a change in the dipole moment perpendicular to the surface are visible in SEIRAS. This can also be explained in terms of induced image dipoles (Pearce and Sheppard, 1976; Hexter and Albrecht, 1979).

### *Chemical gold film deposition*

A triangular silicon prism was used as the internal reflection element. For the SEIRA spectroscopy a thin gold film (so called gold island film or nano-structured gold film) was deposited on one of the rectangular sides by chemical deposition (Osawa, 1997; Miyake et al., 2002; Ataka and Heberle, 2003, 2007).

First, the old gold film was removed in a solution of 12% (v/v) hydrogen peroxide and 11% (v/v) hydrochloric acid at 80 °C. The gold was oxidized and solubilized as a chloro complex. The prism was rinsed with double-distilled water and carefully polished with aluminium oxide powder ( $\text{Al}_2\text{O}_3$ , <10 micron, Sigma-Aldrich) in turns until the surface became hydrophobic. Afterwards, the prism was incubated with an aqueous 40% (w/v) ammonium fluoride solution (Fluka) at 80 °C for approximately 1 minute in order to remove the silicon oxide layer and terminate the surface with hydrogen. By the etching with  $\text{NH}_4\text{F}$  solution, the formation of silicide between silicon and gold in the next step was enhanced.

The prism was rinsed with double-distilled water and placed in a water bath at 80 °C. A home-built Teflon holder was used to orient the hydrophobic side parallel to the ground and to keep it 5 mm higher than the water surface. After 10 minutes of thermal equilibration the hydrophobic side of the prism was covered with a (freshly mixed) 1:1:1 mixture of (1) 0.3 M Na<sub>2</sub>SO<sub>3</sub> (Riedel-deHaën), 0.1 M Na<sub>2</sub>S<sub>2</sub>O<sub>3</sub> (Sigma-Aldrich), and 0.1 M NH<sub>4</sub>Cl (Merck), (2) 0.03 M NaAuCl<sub>4</sub> (Sigma-Aldrich), and (3) 2% (v/v) hydrofluoric acid (Merck) (Figure 8). Under these conditions, gold was reduced and silicon was oxidized and solubilized as SiF<sub>6</sub><sup>2-</sup>.

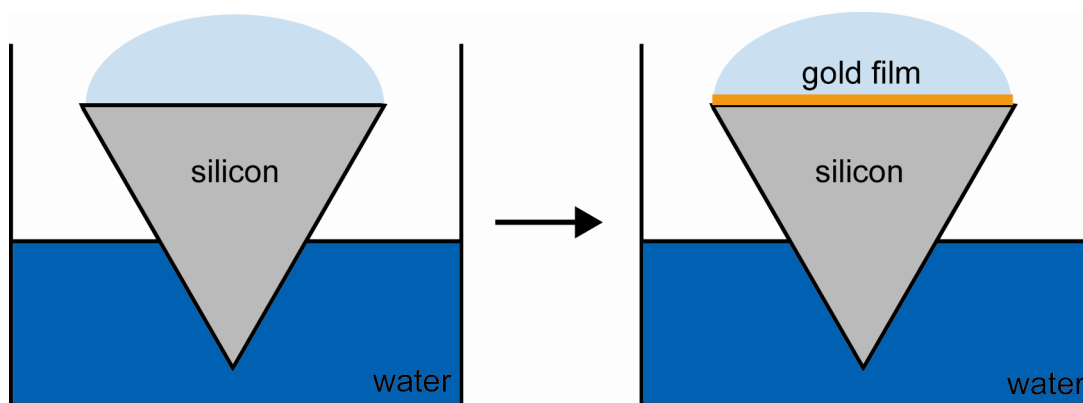


**Figure 8 Chemical gold film deposition** | The prism is fixed with the hydrophobic side parallel to the ground in contact to a water bath. The “gold deposition” solution is placed on top a gold film is spontaneously formed.

Cyclic voltammetry (Chapter 3.7.1) was used to remove organic contaminations on the gold film. The gold film was used as the working electrode and the potential was cycled three times between 300 and 1700 mV (vs NHE) at a sweep rate of 50 mV s<sup>-1</sup>.

#### *Customization of the setup*

A glass cell was mounted on top of the silicon prism and allowed the incubation of the gold film in different solutions. The solution was accessible during the measurement and the pH could be changed or substances could be added. In addition, the gold film was connected as a working electrode and electrochemical measurements were possible on the same surface, which was monitored by SEIRAS. An optical fibre bundle allowed light-induced experiments (Figure 9). A glove bag was used as described earlier (Chapter 3.4.2) to perform anaerobic experiments.

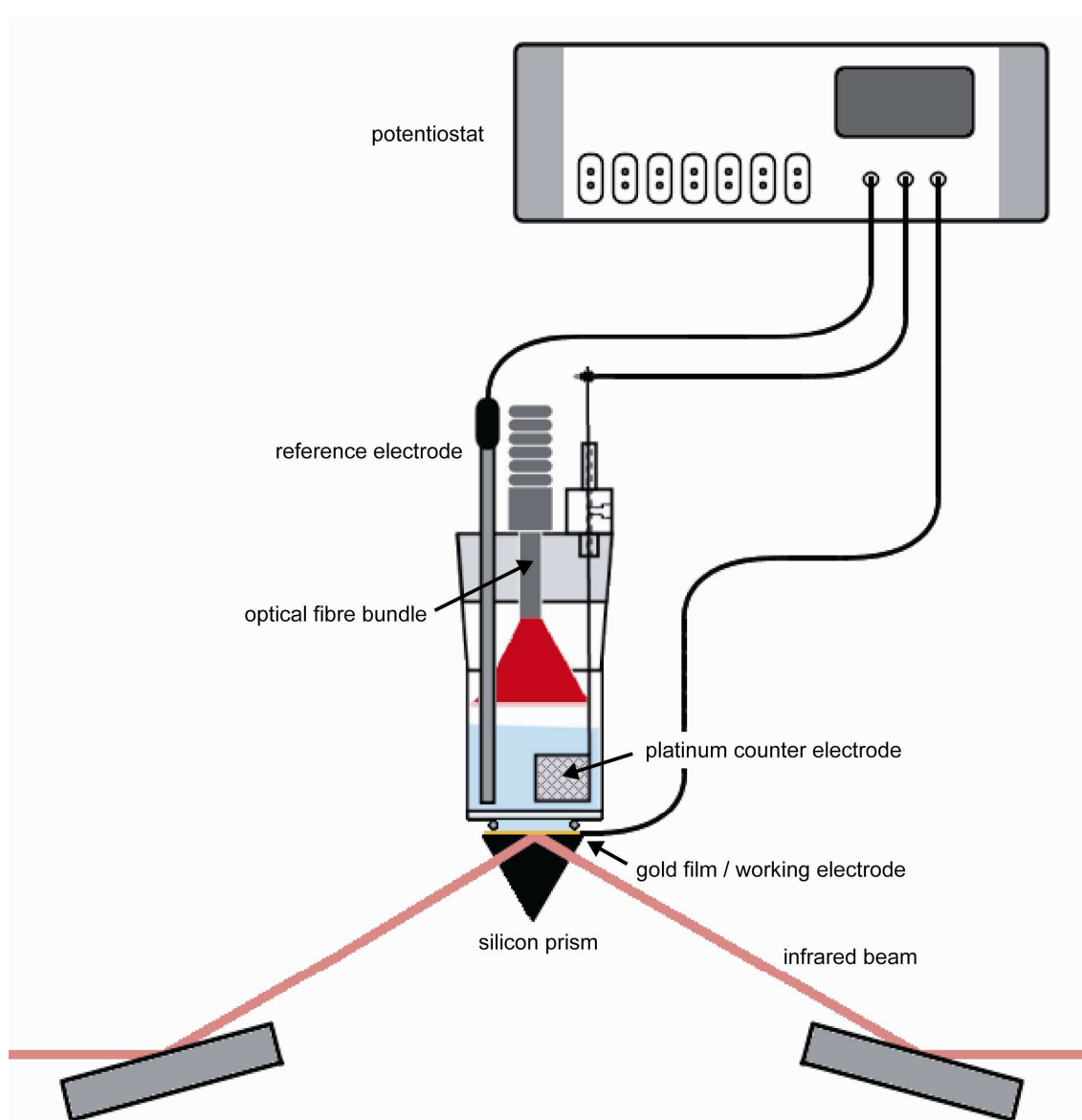


**Figure 9** *Electrochemical SEIRAS setup* | The IR beam is coupled into a triangular, single-reflection silicon prism. The equipped electrodes complete the electrochemical setup; the fibre bundle allows light-induced experiments.

#### *Comparability of different measurements*

Although all gold films were prepared according to the same protocol, the surface enhancement factor was not the same for each gold film. The surface enhancement factors of the used gold films deviated from each other at maximum by a factor of 5. In order to compare SEIRA spectra from different gold films, the spectra were normalized to the intensity of a prominent band of the first surface modification step (e.g. the C=O vibration of the succinimidyl ring of DTSP at  $1739\text{ cm}^{-1}$ ).

The surface enhancement factor is principally defined by the structure of the gold film. In addition, chemical modifications of the surface change the optical properties of the gold-water interface and might affect the surface enhancement factor as well - although they are commonly neglected in electromagnetic enhancement models (Aroca and Ross, 2004). In the used normalization procedure, the chemical contribution of the first modification step was taken into account. Data which were normalized by this procedure were noted as “relative absorbance”. This normalization procedure is based on the assumption that thiols form highly-reproducible self-assembled monolayers.

### 3.5 UV/Vis spectroscopy

A prism or diffractive grating was used to separate single wavelengths from a beam of visible and/or UV light and scan the defined wavelength region with time. The emitted light was split into two beams of equal intensity. One beam passed through the sample cuvette, which contained the protein solution, the other one passed through the reference cuvette, which contained only the solvent. The absorbance  $A$  of the protein at each wavelength was calculated from the intensity  $I$  of both beams, according to equation (4).

$$A = -\lg \frac{I_{Sample}}{I_{Reference}} \quad (4)$$

A 0.5  $\mu\text{M}$  solution of PS1 in PS1 buffer (

Table 2) was measured with an Uvikon 943 spectrometer (Tresser Instruments, Groß-Zimmern, Germany).

### 3.6 Surface plasmon resonance

Surface plasmon resonance (SPR) measurements were performed in collaboration with the workgroup of Prof. N. Sewald (Bielefeld University, Germany).

SPR technique was used to quantify binding events to a gold surface. The experiments were performed on a Biacore 3000 (GE Healthcare, Uppsala, Sweden) with a constant flow rate of 5  $\mu\text{L min}^{-1}$ . Au Sensorchips were used to provide an untreated gold surface for each experiment and modified as described in chapter 3.3. The measured response (in response units R.U.) is correlated to changes in the refractive index, caused by an increase of the protein concentration at the surface.

SPR is a phenomenon which can be observed at the interface between two transparent media of different refractive indices. Depending on the angle of incident, light, which comes from the side of higher refractive index, is partly refracted and partly reflected. If the angle  $\alpha$  between the interface plane and the incoming light becomes small enough the light is totally reflected. In the area of the total reflection an evanescent wave penetrates into the medium of lower refractive index with a distance of approximately one wavelength (Figure 10).

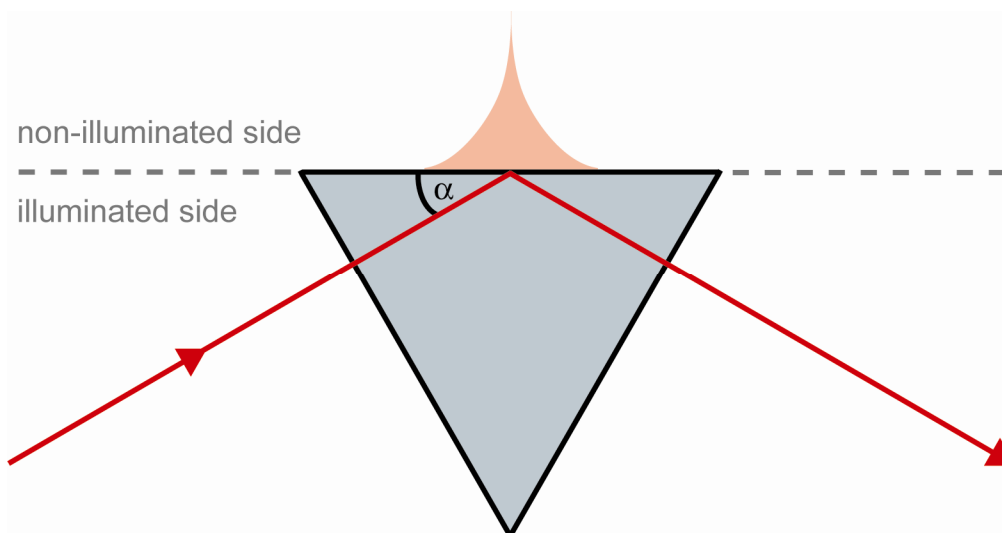


**Figure 10** *Evanescent wave* | An IR beam is coupled into an internal reflection element at an angle of  $30^\circ$ . The IR beam is totally reflected and an evanescent wave occurs at the place of total reflection and penetrates into the non-illuminated side.

The sample is illuminated with different incident angles at the same time and the angle-dependent intensity of the reflected light is recorded. If a thin gold film is deposited on the interface between both media (and monochromatic p-polarized light is used) the intensity of the reflected light is significantly reduced at a specific incident angle. This phenomenon is called SPR. The angle changes with the surface concentration of solutes (e.g. immobilized protein) (Kretschmann and Raether, 1968).

### 3.7 Electrochemistry

The electrochemical experiments were performed in a three electrode setup. A gold film or a massive gold electrode was used as a working electrode. Ag/AgCl/3M KCl (WPI, Sarasota, USA) and a platinum mesh were used as the reference and counter electrodes, respectively (Figure 9). The current flow was measured between working and counter

electrode and the voltage was controlled between working and reference electrode. The ohmic drop between working and reference electrode could be neglected, because almost no electrons were transferred between these electrodes. A potentiostat (Autolab PGSTAT 12, Eco Chemie B.V., Utrecht, Netherlands) was used to record the data. All potentials in this work are reported versus the normal hydrogen electrode (NHE).

### 3.7.1 Cyclic voltammetry

In cyclic voltammetry an external potential was applied and the resulting current was recorded. The potential was changed with a constant sweep rate (e.g.  $10 \text{ mV s}^{-1}$ ) until the reversal potential was reached and the scan rate was inverted. The scan rate was reversed again at the second reversal potential and the resulting waveform (for one cycle) had the form of two, connected isosceles triangles (Figure 11). The current response is discussed later in detail (Chapter 4).

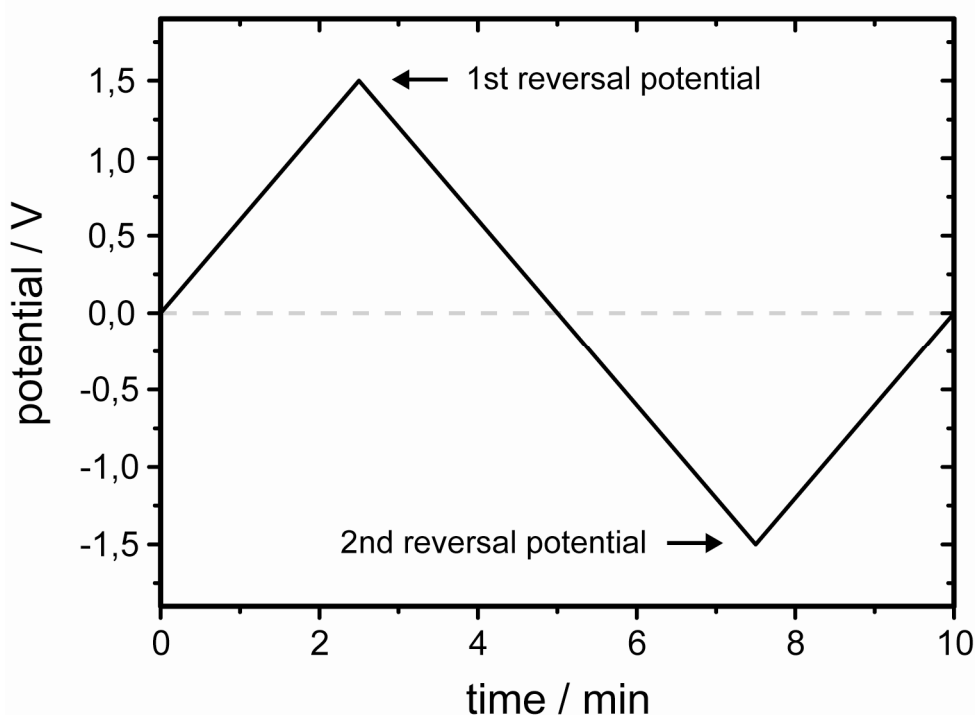


**Figure 11** Waveform for cyclic voltammetry | The potential is cycled between 1.5 V and -1.5 V with a constant sweep rate of  $10 \text{ mV s}^{-1}$ . One full cycle is presented – starting at a potential of 0 V.

The electrochemical investigation of the [FeFe]-hydrogenase CrHydA1 was performed in an anaerobic chamber (Coy Laboratory Products, Grassland, MI, USA) containing

95% nitrogen and 5% hydrogen. Palladium catalysts were used to remove oxygen contaminations by reduction with hydrogen. All solutions were degassed in vacuum for at least 30 minutes and stored in the anaerobic chamber for at least two weeks prior to use. Other equipment, which was transferred to the anaerobic chamber, was evacuated for at least 30 minutes. In this environment, the recorded cyclic voltammograms were totally stable and not influenced by oxygen during the measurement.

Less oxygen-sensitive compounds were prepared under normal atmosphere and bubbled with argon for 20 minutes prior to use. During the experiment these samples were covered by an argon stream.

### 3.7.2 Amperometry

Amperometry was used to determine the functionality of surface-tethered molecules and to control the conditions during electrochemical hydrogen production. In general, a constant potential was applied to a chemically-modified electrode and the time-dependent current response was monitored.

#### *Light-induced hydrogen production*

A monolayer of the hybrid complex of photosystem I and membrane-bound hydrogenase (PS1-MBH) was bound to the Ni-NTA modified surface. N-methylphenazonium methyl sulfate (PMS, Fluka) was used as soluble electron carrier between the gold surface and photosystem I (PS1) in a concentration of 75  $\mu\text{M}$ . The monolayer was equilibrated at defined pH and under potential control until the current flow through the solution became approximately constant and most of the PMS was reduced. The increase of the current was measured under illumination (KL 1500 electronic, Schott, Mainz Germany) and noted as photocurrent. Each experiment was performed with a suitable interference filter (most frequent:  $\lambda_{\text{max}}=702$  nm,  $hw=16$  nm) and under argon atmosphere.

For the detection of hydrogen the electrochemical setup was embedded in a home-made, gas-tight measuring cell with a total volume of 20 mL. The setup was purged with argon until no traces of hydrogen could be detected by gas-chromatography (Chapter 3.8). Then a constant potential (most frequent: -90 mV) was applied and the sample was illuminated by red light for a defined time (20-40 minutes). The produced hydrogen was quantified by gas chromatography.

#### *Potential-induced hydrogen production*

After immobilization of the [FeFe]-hydrogenase CrHydA1 and addition of 100  $\mu\text{M}$  methylviologen dichloride the setup was purged with argon for at least 10 minutes to

remove the atmospheric hydrogen of the anaerobic chamber. 1 mL of the gas phase in the measuring cell was injected into a gas chromatograph (Chapter 3.8) to gauge if the hydrogen-containing atmosphere was completely exchanged. Then a potential of -450 mV was applied for 20 minutes while the current was monitored. 1 mL of the gas mixture was injected into a gas chromatograph to determine the amount of evolved hydrogen.

### 3.8 Gas chromatography

Gas chromatographic experiments were performed in collaboration with the workgroups of Prof. T. Happe (Ruhr-Universität Bochum, Germany) and Prof. O. Kruse (Bielefeld University, Germany).

The amount of produced hydrogen was determined by gas chromatography. 1 mL of the gas phase in the measurement cell was injected into the chromatographic column and analyzed. The sample was transported through the column of the gas chromatograph by an argon flow and the thermal conductivity was monitored after the chromatographic separation (Figure 12).

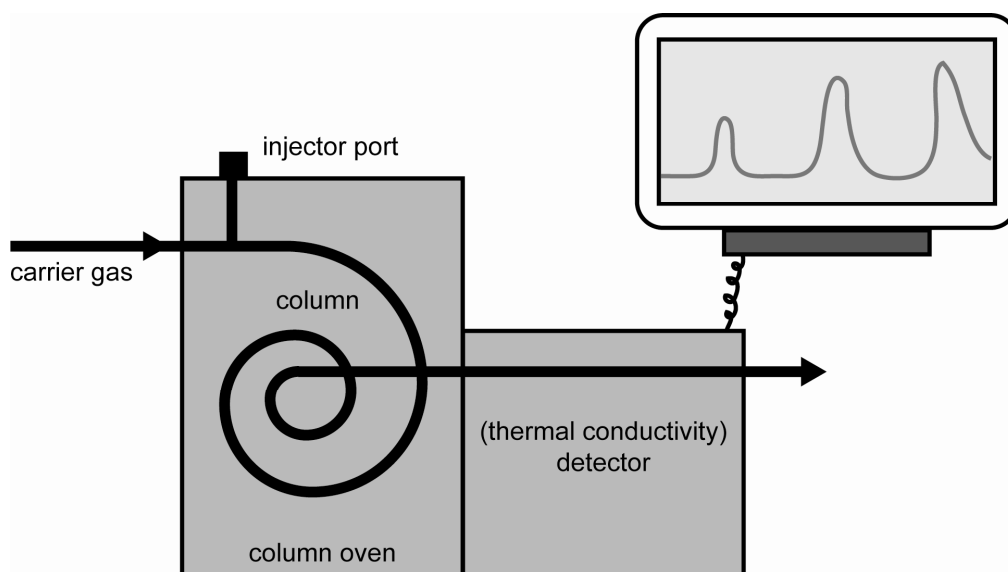


**Figure 12** *Gas chromatography setup* | A gas sample is injected into a chromatographic column and separated into its components. The thermal conductivity of each component is used for identifying and quantifying.

Different gases were separated depending on their interaction with the column. Among the three analyzed gases, hydrogen had the shortest retention time, nitrogen had the



longest retention time, and oxygen was eluted in between. The retention times were determined from reference measurements of the pure gases, and used to assign the measured peaks. The absolute retention times were not compared between different devices, because they varied with column length, column packing, temperature, and flow rate of the carrier gas.

The amount of the injected hydrogen was calculated from the integral area of the hydrogen peak. The required conversion factor was determined by measuring small, defined amounts of hydrogen. Therefore, hydrogen was diluted 1:3000 in a 2 L steel barrel. The steel barrel was evacuated, refilled with hydrogen, evacuated to 2 mbar and filled with nitrogen to a final pressure of 6 bar. Volumes of approximately 1 mL of this mixture (at 1 bar) were used for the reference measurements to yield area values in the same order of magnitude as in the sample measurements.

For all experiments with the [FeFe]-hydrogenase *CrHydA1* a GC-2010 (Shimadzu, Kyoto, Japan) gas chromatograph was used, while a 3000A Micro GC (Agilent Technologies, Santa Clara, United States) gas chromatograph was used for all other experiments.

### 3.9 Atomic force microscopy

Atomic force microscopy (AFM) experiments were done in collaboration with the workgroup of Prof. M. Havenith (Ruhr-Universität Bochum, Germany).

Topographical information about different chemically-modified surfaces were recorded. The setup was based on a commercial tapping mode atomic force microscope (Nanotec Electronica) where the AFM head was modified to meet specific applications utilizing the Nanotec electronics and software (Software: WSxM, Horcas et al., 2007). A gold-coated cantilever (NSC16 Cr-Au, Mikro Masch, Tallinn, Estonia) with a tip curvature radius of 40 nm was used. The tip was fixed with respect to the x-y plane of the sample, but oscillated vertically with a resonance frequency of approximately 170 kHz. The sample was moved in the x-y plane by piezoelectric transducers (PZT scanner) to allow the interaction between the oscillating tip and every part of the sample area. The influence on the oscillation was not measured directly, but measured by a beam deflection system. A laser beam was reflected on the back of the cantilever and measured by a position-sensitive detector (Figure 13). The position (in z-direction, perpendicular to the sample plane) of the cantilever was calculated from this information.

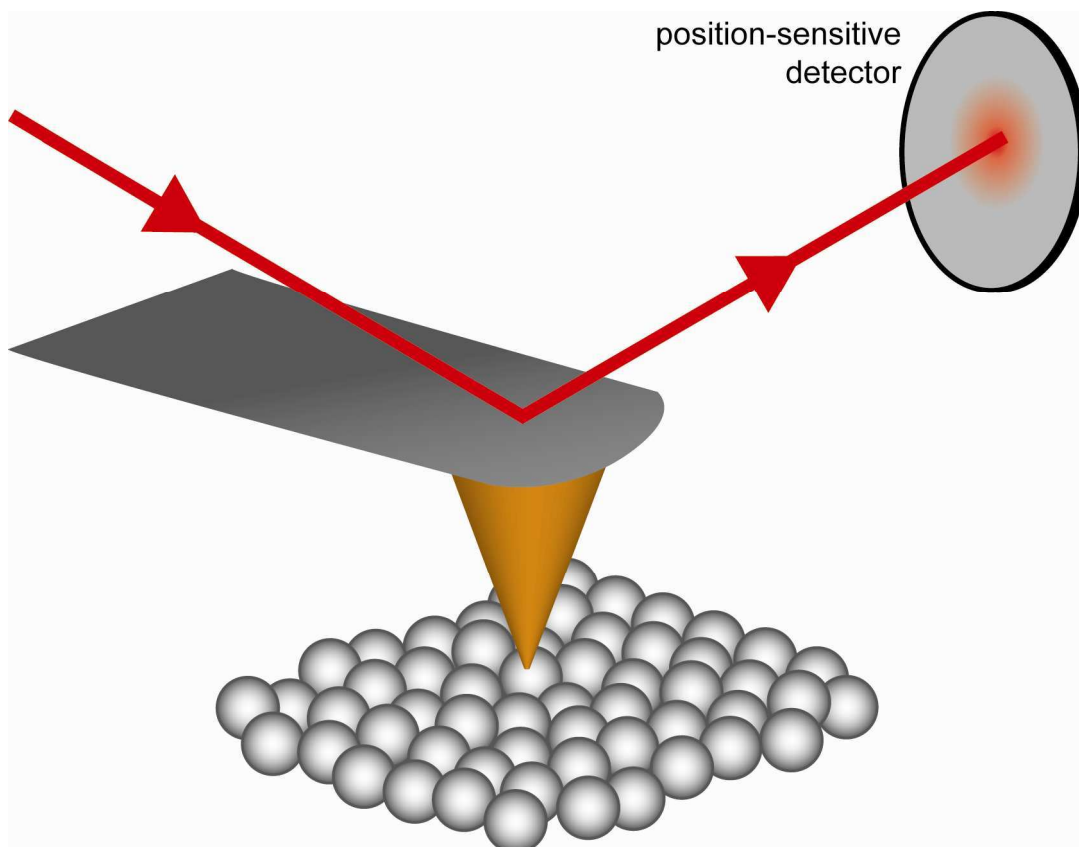


**Figure 13** *Atomic force microscopy setup* | The AFM tip probes a rough surface, while a laser beam is reflected on the back of the cantilever. A position-sensitive detector is used to indirectly monitor the oscillation of the cantilever.

The AFM samples were prepared on template-stripped gold as described in chapter 3.3. To prepare template-stripped gold, a 150 nm thick gold film was evaporated on an atomically flat silicon wafer (Anfatec, Oelsnitz, Germany) (without adhesive layer in between). Glass slides (~5x10 mm) were glued on top of the gold with Epotek 377 for 90 minutes at 150 °C. Afterwards, the glass slides were removed and the gold film stuck to the glass slides (Figure 14(A)). The exposed gold surface had differences in height of at most 1.5 nm (Figure 14(B)). The investigated protein films were dried prior to measuring.

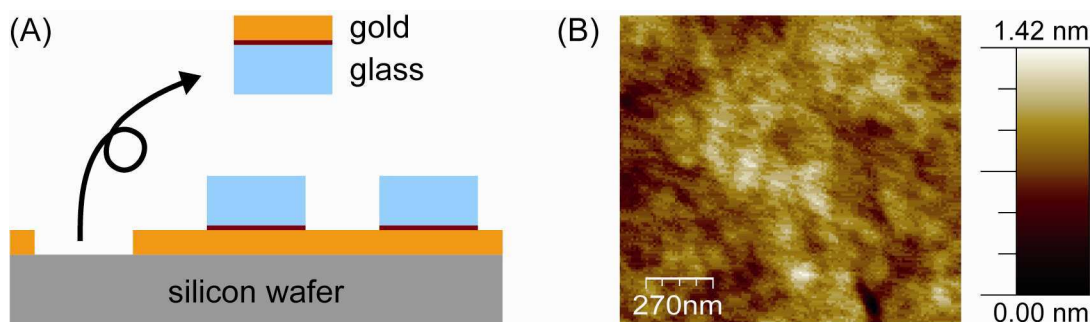


**Figure 14** *Template-stripped gold* | (A) Glass slides are glued to a gold-coated silicon wafer. The glass is removed and the gold sticks to the glass. (B) Topography of template-stripped gold measured by AFM.

### 3.10 Scanning near-field infrared microscopy

Scanning near-field infrared microscopy (SNIM) experiments were performed in collaboration with the workgroup of Prof. M. Havenith (Ruhr-Universität Bochum, Germany).

This technique was applied with the aim to measure a chemical image of a reconstituted protein monolayer – a two dimensional resolved infrared spectrum, which can be correlated with topographical information.

The home-built SNIM setup (Figure 15) was based on the AFM setup which was described before (Chapter 3.9). As a radiation source served a home-built liquid nitrogen-cooled sealed-off CO-laser system with an output power  $>1\text{W}$  and an emission range from  $1600$  to  $2100\text{ cm}^{-1}$ . The laser system provided about 400 laser lines with an average line spacing of about  $1.2\text{ cm}^{-1}$ . In the SNIM experiments a power output of approximately 300 mW (measured at the laser output) was used to avoid strong heating of the sample. The laser was coupled into a beam expander telescope and focused on the AFM tip by a parabolic mirror. The IR beam was scattered from the oscillating tip and focused by a  $\text{CaF}_2$  lens onto a mercury cadmium telluride detector (MCT, Judson Technologies, Montgomeryville, USA) (Kopf et al., 2007). A lock-in amplifier was used to isolate the light, which was scattered by the oscillating AFM tip, from the light, which was scattered on non-oscillating objects.

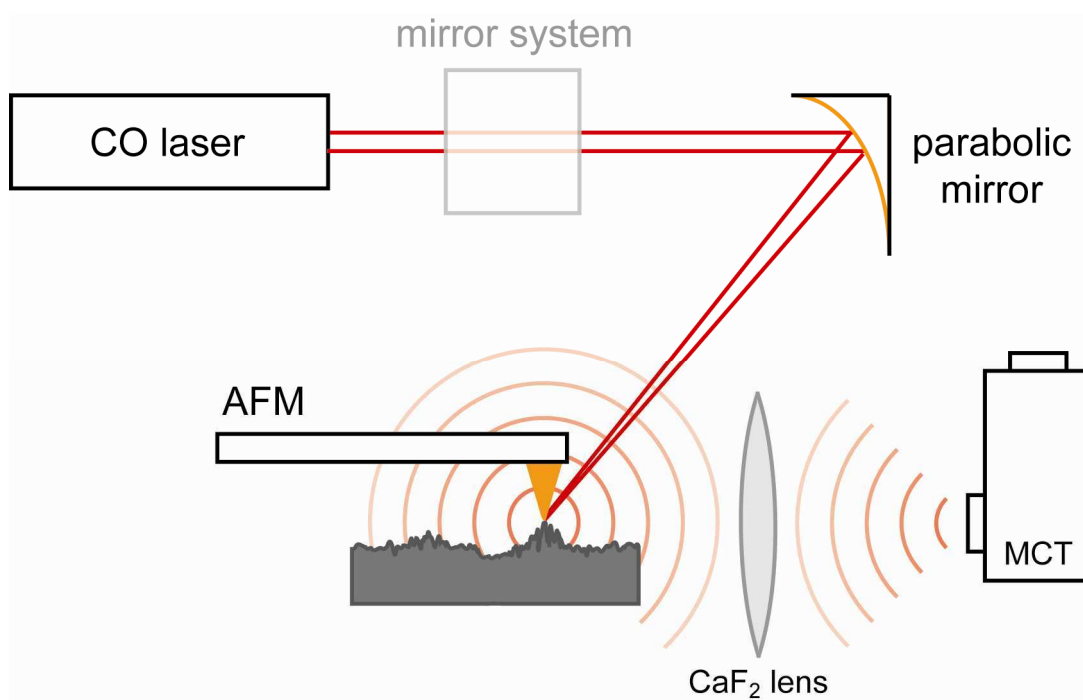


**Figure 15** *Scanning near-field infrared microscopy setup* | The scheme depicts a scattering-type SNIM. An IR beam is emitted by a tuneable CO and focused on the tip of an AFM. The scattered light is focused on a MCT detector by a CaF<sub>2</sub> lens.

In this aperture less or scattering SNIM, the resolution was not limited by Abbe's diffraction limit ( $\lambda/2$ ). As long as the sample was in the near-field region of the light-scattering AFM tip a spatial resolution of less than  $\lambda/100$  could be demonstrated (Knoll and Keilmann, 1999). Gold nano particles were dried on the sample as a contrast reference (Chapter 4.3).

## 4 Results and discussion

### 4.1 Electrocatalytic surface for hydrogen production

In this chapter, I present the development of an enzyme electrode which is able to catalyze the reduction of protons to molecular hydrogen at minuscule overpotential.

A fundamental problem in protein electrochemistry is that the electron transfer reactions of proteins occur slowly at bare metal electrodes. Cytochrome *c*, a small redox protein, is the most intensively studied protein with regard to its electrochemical properties, but the redox cycle could not be detected at gold (Heineman et al., 1975) or platinum (Kôno et al., 1958) electrodes. Irreversible responses were also reported for other electrodes such as mercury (Scheller et al., 1975), nickel (Kuznetsov et al., 1979), silver (Cotton et al., 1980), and silicon (Lewis and Wrighton, 1981). The major breakthrough came in 1977, when a reversible electron transfer between cytochrome *c* and a 4,4'-bipyridyl-modified electrode was reported (Eddowes and Hill, 1977). Since this time surface modifiers have been used to provide suitable interfaces for the interaction with proteins.

Here, the surface modification and immobilization of the [FeFe]-hydrogenase (*CrHydA1*) from *C. reinhardtii* was probed *in situ* by surface-enhanced infrared absorption spectroscopy (SEIRAS). Electrochemistry provided evidence for the catalytic activity of surface-bound *CrHydA1* in the production of hydrogen. Surface plasmon resonance (SPR) and gas chromatography were used to determine the specific hydrogen evolution activity of the immobilized enzymes.

*CrHydA1* was used for this prototype electrode because it is stable at ambient temperatures and deals with a wide range of buffers and salt concentrations. *CrHydA1* has one of the highest reported hydrogen evolution activities (Happe and Naber, 1993; Forestier et al., 2003; Girbal et al., 2005) and shows only minor product inhibition. In addition, the enzyme only consists of the catalytic active H-cluster, but lacks any kind of accessory [FeS]-cluster (Happe and Kaminski, 2002). The exceptionally small size (48kDa) will result in a higher number of catalytic centers per electrode area compared to other hydrogenases.

#### 4.1.1 Immobilization of the [FeFe]-hydrogenase

To design a surface which is able to reduce protons to molecular hydrogen, the catalyst, *CrHydA1* is immobilized on the surface of a carboxy-terminated gold electrode by

electrostatic interaction. Electrons are transferred from the gold surface, via the soluble electron carrier methylviologen, to the hydrogenase, where they reduce protons to molecular hydrogen (Figure 16).

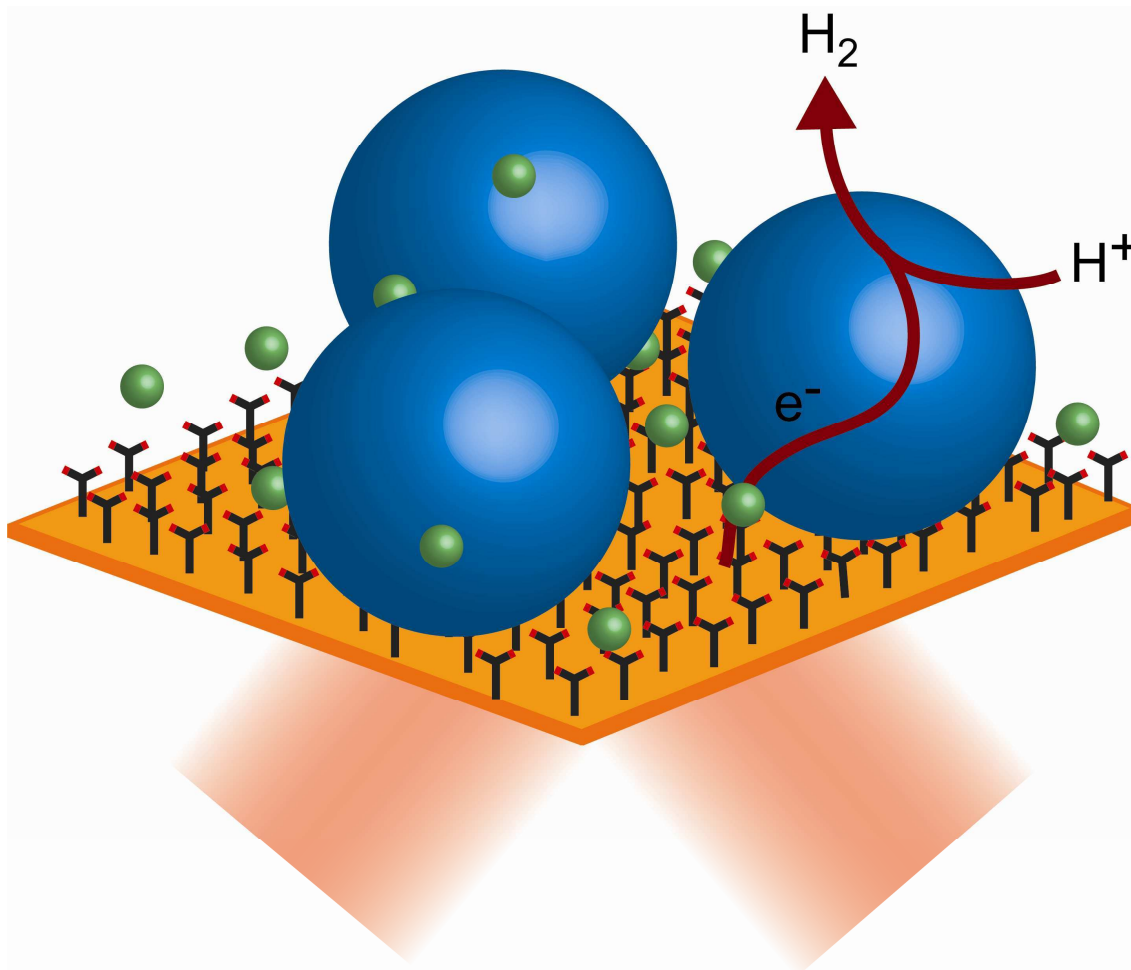


**Figure 16** *CrHydA1 on a mercaptopropionic acid monolayer* | The [FeFe]-hydrogenase CrHydA1 (blue) is immobilized on a mercaptopropionic acid monolayer. The soluble electron carrier MV (green) transports electrons from the surface to the hydrogenase. The monolayer is probed by IR spectroscopy. For sake of visual clarity, the size of CrHydA1 is reduced by a factor of about 2 with respect to the mercaptopropionic acid molecules.

Mercaptopropionic acid (MPA) or mercaptoundecanoic acid (MUA) is used to form a carboxy-terminated surface. At pH 6.8, these surfaces are negatively charged and allow electrostatic binding of CrHydA1. The surface structure of CrHydA1 is shown in Figure 17. Positively charged amino acids (blue) and negatively charged amino acids (red) are distributed over the surface and only a slight accumulation of positive charges exists in the vicinity of the active site (yellow/orange). It seems likely that this area is oriented

towards the carboxy-terminated surface under the used conditions - but the orientation can not be measured by the available techniques.

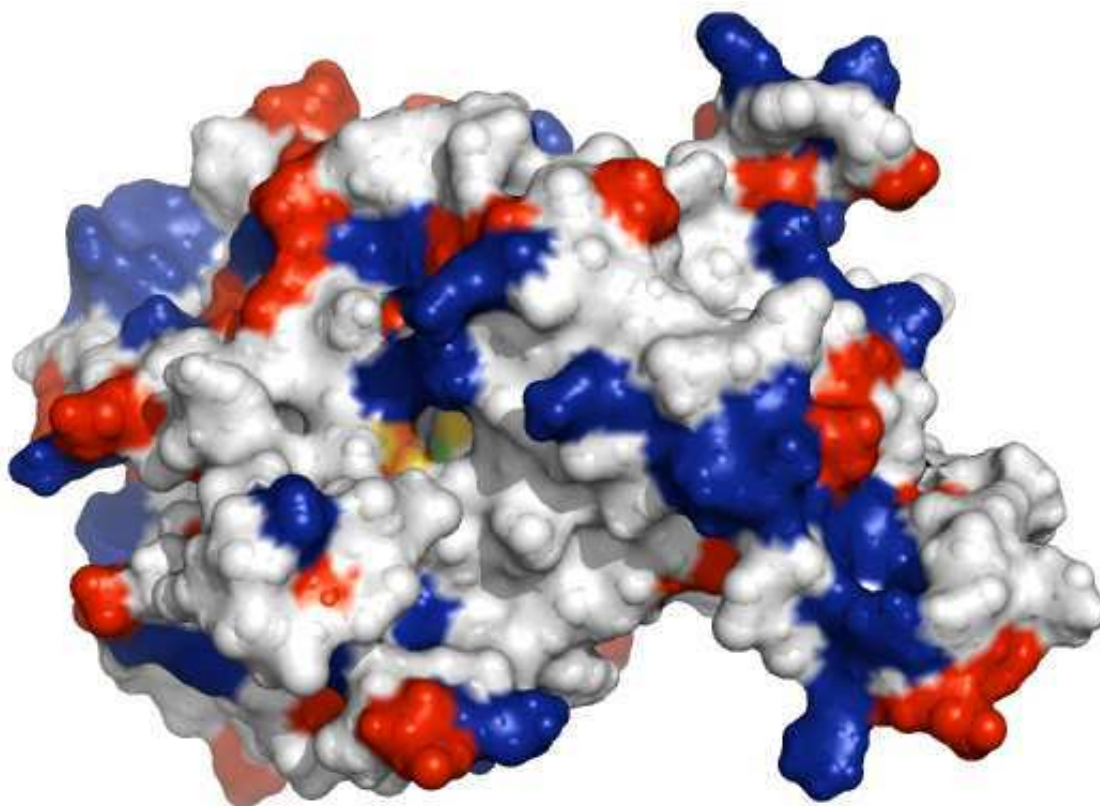


**Figure 17 Surface charges of CrHydA1** | The surface structure of CrHydA1 is based on the homologous hydrogenase CpI from *Clostridium pasteurianum* (PDB-ID: 1FEH (Peters et al., 1998)). The H-cluster is shown in yellow/orange, positively charged amino acids (arginine, histidine, lysine) are coloured in blue, and the negatively charged amino acids (aspartic acid, glutamic acid) are coloured in red.

The strength of the electrostatic interaction between protein and surface varies with the chosen surface modifier. Although both surface modifiers, MUA and MPA, assemble negatively charged, carboxy-terminated monolayers, the adsorption time of CrHydA1 greatly varies (The adsorption kinetics are presented in Figure 32). 90% of the maximum coverage with CrHydA1 on an MUA monolayer is reached after 5 min, while it takes 50 min on an MPA monolayer. The monolayers form inhomogeneous surface structures, which vary with the adsorption time (Krause et al., 2008). These substructures most likely are different for MUA and MPA. They influence the interaction with the protein and explain the different adsorption kinetics. On both monolayers, the immobilized protein film is stable. Rinsing with buffer (10 mM potassium phosphate, pH 6.8) only removes the unspecifically bound protein. The

amount of adsorbed protein decreases by less than 5% at the beginning, while further washing does not lead to a further decrease in intensity (data not shown).

The immobilization of *CrHydA1* on an MPA-modified surface is monitored *in situ* by SEIRAS (Figure 18(A)). The bands, which arise at  $1659\text{ cm}^{-1}$  and  $1550\text{ cm}^{-1}$ , are assigned to the amide I (predominantly C=O stretching vibration of the peptide bond) and amide II (C=N stretching coupled to N-H bending vibration) modes of the protein backbone, respectively (Krimm and Bandekar, 1986; Lewis and McElhaney, 2002). The band intensities reflect the amount of protein adsorbed to the surface and therefore increase during the adsorption process. While the proteins bind to the surface, a negative band arises at frequencies  $> 1700\text{ cm}^{-1}$ , which overlaps with the amide I band. This band is assigned to water (H-O-H bending mode), which is displaced from the vicinity of the surface. Signals from the bulk phase are negligible as the surface-enhancement decays exponentially with distance (decay length  $\sim 10\text{ nm}$ ). The absence of any amide bands upon injecting a *CrHydA1* solution to an unmodified gold surface in Figure 18(B) shows that *CrHydA1* does not bind to a bare gold surface.



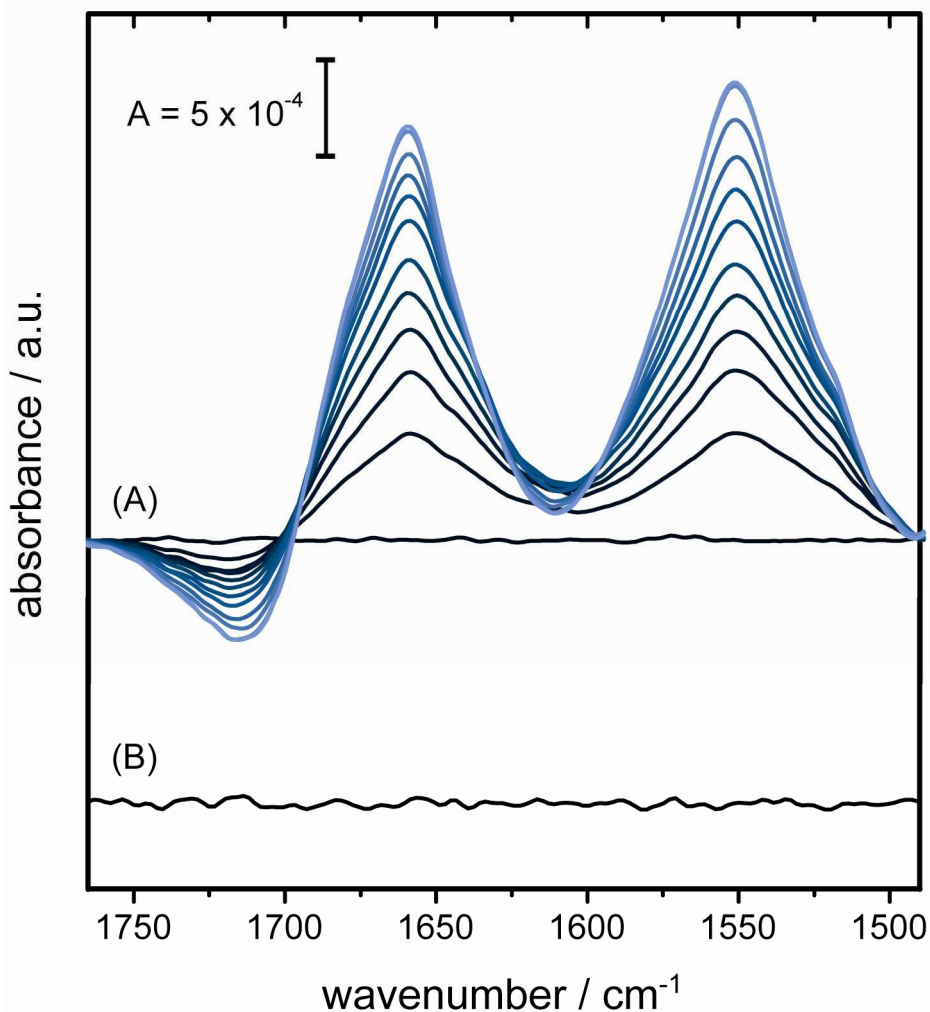


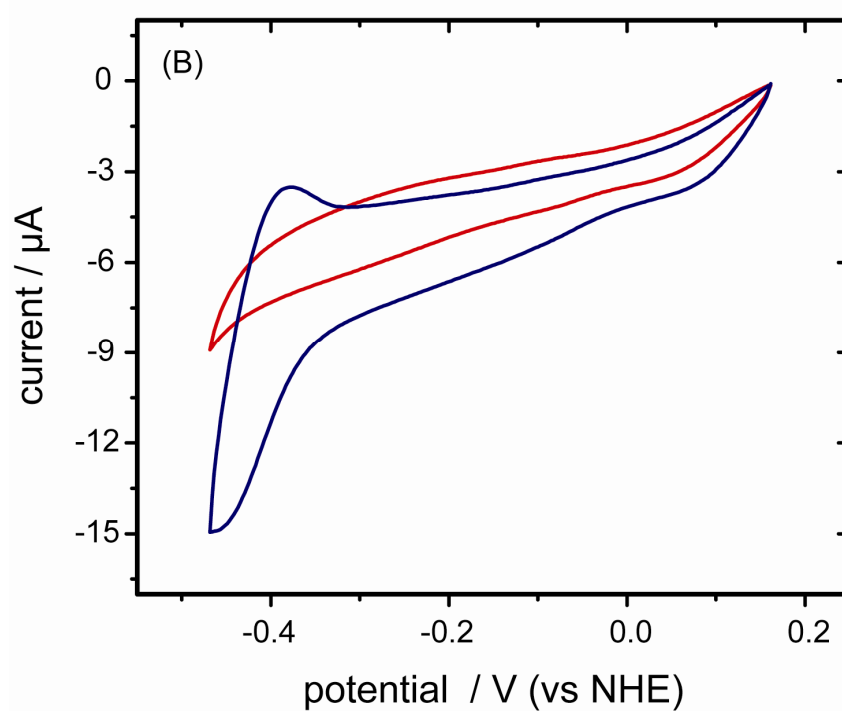
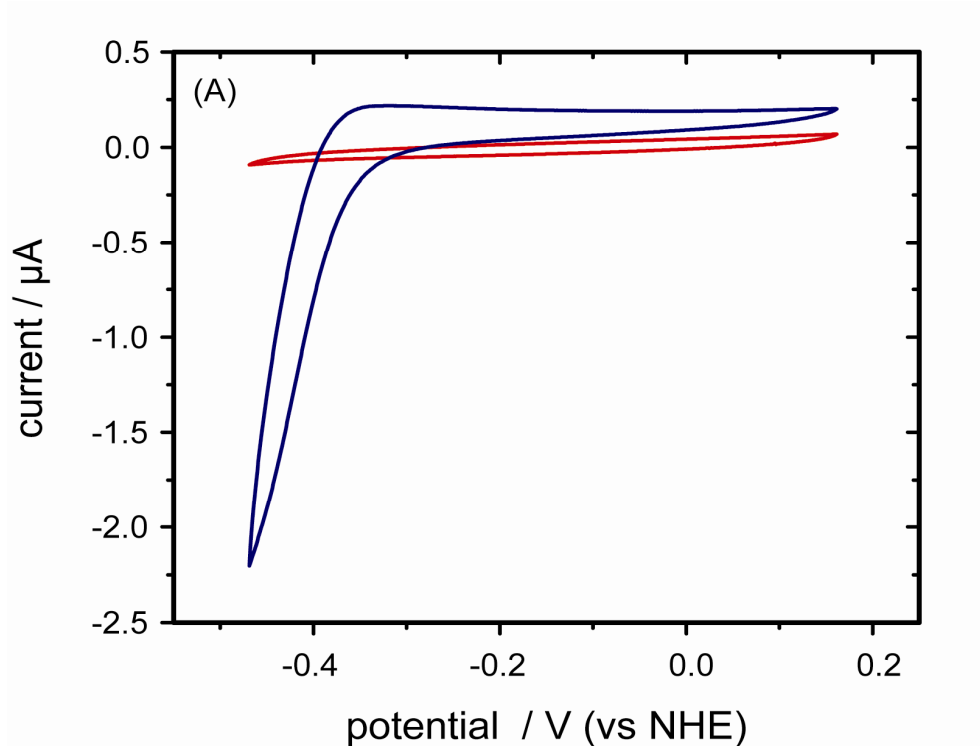
**Figure 18** SEIRA spectra of the binding of CrHydA1 / (A) SEIRA spectra of the binding to an MPA-modified surface. The displayed spectra are recorded at 0 (black), 0.5, 1, 2, 5, 10, 20, 30, 45, 60, 75, and 90 min (light blue) after addition of the protein. The rising bands indicate the binding process and are discussed in the text. (B) SEIRA spectrum of a bare gold surface after incubation with CrHydA1 for 30 minutes. The absence of bands indicates that CrHydA1 does not bind to the bare gold surface.

#### 4.1.2 Electro catalytic activity

The electrochemical response of two different types of CrHydA1-modified gold surfaces is compared by means of cyclic voltammetry. In the cyclic voltammograms of CrHydA1 on an MUA-modified surface (Figure 19(A), red curve), no increase in the reductive current (at low potential) is observed. This observation indicates that electrons are not directly transferred from the electrode to the hydrogenase. After addition of the

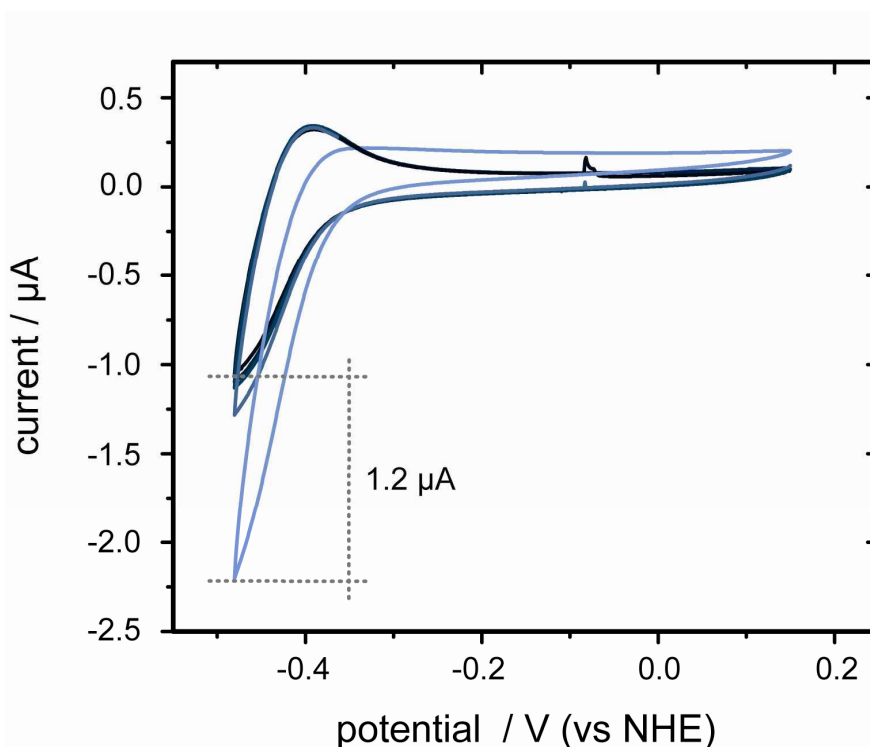
electron mediator methylviologen ( $MV^0$ : reduced form,  $MV^{2+}$ : oxidized form) the reductive current increases (Figure 19(A), blue curve) due to electron transfer from the electrode to  $MV^{2+}$ . When increasing the potential, no oxidation peak appears, indicating that  $MV^0$  is oxidized by transferring electrons to the hydrogenase, where electrons are used to reduce protons to molecular hydrogen.

Figure 19(B) shows the cyclic voltammogram of *CrHydA1* on a bare gold electrode (red curve). If electrons were transferred to the hydrogenase the amplitude of the reductive (“negative”) current would increase below the necessary potential. The absence of this feature proves that there is no direct electron transfer from a bare gold electrode to *CrHydA1* in solution. The addition of MV (blue curve) leads to a pair of reduction and oxidation peak with a mid-point potential of -423 mV, as expected from literature for MV (Stombaugh et al., 1976). The oxidation peak at -383 mV is assigned to the re-oxidation of MV at the electrode and its appearance shows, that  $MV^0$  is not (or at a negligible rate) oxidized by the hydrogenase. No (or negligible) mediated electron transfer takes place between a bare gold electrode and *CrHydA1* if the protein is not immobilized on the surface.



**Figure 19** Cyclic voltammograms of CrHydA1 on an MUA-SAM and a bare gold electrode | (A) CrHydA1 is immobilized on an MUA-SAM. The red curve shows the cyclic voltammogram before addition of  $100 \mu\text{M}$  MV, the blue curve after the addition. (B) Cyclic voltammograms of CrHydA1 on a bare gold electrode. The red line is measured before, the blue line 5 min after addition of  $100 \mu\text{M}$  MV.

An additional control experiment was performed to assign the reductive current to hydrogenase activity: Carbon monoxide, the classic inhibitor of hydrogenases (Larminie and Dicks, 2003), was injected into the electrochemical cell, while cyclic voltammograms of an MUA-based *CrHydA1* monolayer were recorded. The reductive peak current of the active *CrHydA1* monolayer had an amplitude of  $2.2 \mu\text{A}$  (Figure 20, light blue curve). Upon injection of carbon monoxide the reductive current decreases by  $1.2 \mu\text{A}$ . This observation confirms that the reductive current depends on the catalytic reaction of the hydrogenase and that its amplitude can be used as a quantitative indicator for the activity of the hydrogenase monolayer.



**Figure 20** *Cyclic voltammograms of CrHydA1 during CO inhibition* | *CrHydA1* is immobilized on an MUA-monolayer. The light blue curve shows the cyclic voltammogram in the presence of  $100 \mu\text{M}$  MV. The cyclic voltammograms after injection of 1 mL carbon monoxide are coloured in darker shades of blue.

An increase of the reductive current after addition of *CrHydA1* to a  $100 \mu\text{M}$  solution of MV on an MPA-modified electrode is observed (Figure 21). Current in the red curve is comparable to the cyclic voltammogram of MV as displayed in Figure 19(B) and solely depends on the electrode area and the MV concentration. The reductive current at a potential of  $-450 \text{ mV}$  reaches a value of  $-47 \mu\text{A}$ , while it is only  $-2 \mu\text{A}$  on an MUA-modified electrode (Figure 19(A)).

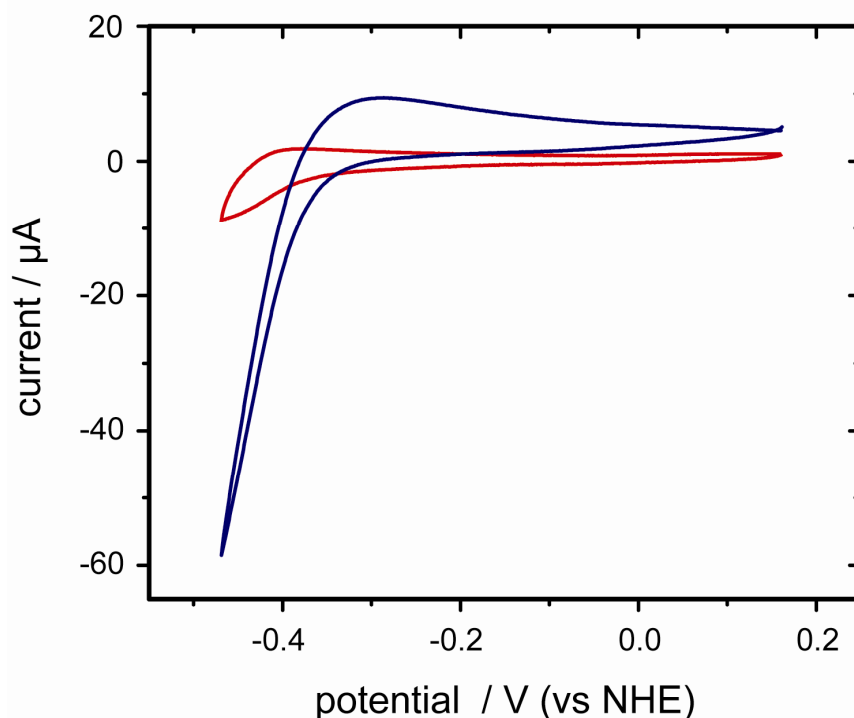


**Figure 21** Cyclic voltammograms of CrHydA1 on a MPA-SAM | The cyclic voltammogram of a 100  $\mu\text{M}$  MV solution on an MPA-modified gold electrode (red curve) is compared to the cyclic voltammogram 10 min after addition of 3.5  $\mu\text{M}$  CrHydA1 (blue curve).

An emerging question is, which electron transfer step is limiting to the rate of hydrogen evolution. Possible candidates are the reduction of  $\text{MV}^{2+}$  and the electron transfer from  $\text{MV}^0$  to CrHydA1. The electron transfer inside the hydrogenase is not considered because the hydrogen evolution rate in solution is about hundred times higher than for the immobilized enzyme (Chapter 4.1.3).

Electron transfer from the electrode surface to  $\text{MV}^{2+}$  is measured as reductive current.. If reduced  $\text{MV}^0$  is re-oxidized by the hydrogenase, the concentration of oxidized  $\text{MV}^{2+}$  increases again and more electrons are able to leave the electrode resulting in a higher (more negative) reductive current.

The reduction rates of  $\text{MV}^{2+}$  are compared by cyclic voltammetry for three different surfaces. Figure 22 shows the redox signals of a 100  $\mu\text{M}$  MV solution in 10 mM potassium phosphate buffer (pH 6.8) on different electrode surfaces at a scan rate of 10  $\text{mV s}^{-1}$ . The peak areas are proportional to the amount of electrons that are transferred during reduction (negative peaks) or during oxidation (positive peaks). The peak areas are the same for the bare gold surface (red curve) and the surface, which is modified by MPA (blue curve) or MUA (black curve), respectively.

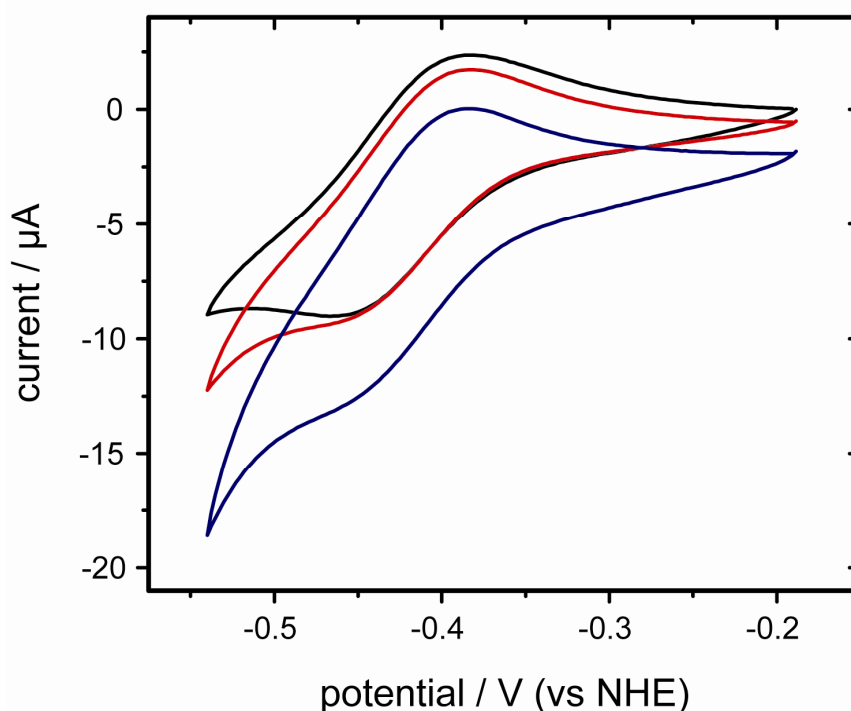


**Figure 22** *Cyclic voltammograms of 100  $\mu\text{M}$  MV on different surfaces* | The cyclic voltammograms are recorded on a bare gold electrode (red), and on the gold electrode modified by MPA (blue) or MUA (black).

If  $\text{MV}^{2+}$  is reduced on top of the self-assembled monolayer (SAM), the reaction rate should be affected by the distance from the surface and thus should result in a smaller peak area in the cyclic voltammetry experiments on MUA. As the peak areas are identical, it can be concluded that  $\text{MV}^{2+}$  is able to penetrate the SAMs and reduction takes place close to the surface at a rate that is faster than electron transfer from  $\text{MV}^0$  to the hydrogenase. Therefore, diffusion of reduced MV to the electron acceptor site of the hydrogenase is the rate-limiting step.

Two major differences between both SAMs may explain the difference in the reductive current: (1) The MUA layer is thicker and the hydrogenase (*CrHydA1*) is immobilized at a longer distance from the electrode surface. Reduced  $\text{MV}^0$  has to diffuse a longer distance and its concentration in the vicinity of the electron acceptor site is lower compared to the hydrogenase on MPA. (2) The MUA layer is more flexible, due to the longer chain length. This allows the SAM to form surface structures different to that of the MPA layer. The orientation of the hydrogenase is probably influenced and sterical hindrance might restrict the access to the electron acceptor site.

### 4.1.3 Specific activity of immobilized [FeFe]-hydrogenase

Cyclic voltammetry shows that electrons are transferred to the hydrogenase (Chapter 4.1.2). However, it is not clear if the transferred electrons are consumed to reduce protons and produce hydrogen. This is demonstrated by the direct detection of molecular hydrogen by gas chromatography. *CrHydA1* is immobilized on an MPA-modified gold film electrode and covered with the MV-containing potassium phosphate buffer (pH 6.8). After a constant potential of -450 mV has been applied to this system for 20 minutes, 1 mL of the gas phase is injected into the gas chromatograph. The area of the hydrogen peak is calculated by integration to be an average area of 140, which equates 20 nmol H<sub>2</sub> ( $n(\text{H}_2)$ ) in the total volume.

While the potential is applied, the current is monitored by amperometry. The transferred charge is calculated to be 25 mC by integration over 20 minutes, which equals a maximum theoretical H<sub>2</sub> production of  $n_{\text{max}}(\text{H}_2) = 130$  nmol, if all electrons are transferred to the hydrogenase. The catalytic efficiency  $\eta_{\text{cat}} = n(\text{H}_2) / n_{\text{max}}(\text{H}_2)$  is found to be 15% at the applied potential of -450 mV.

Two factors contribute to the difference between calculated and measured hydrogen: (1) Electrons can be conducted from the gold electrode to the counter electrode without being used by the hydrogenase. (2) A fraction of the surface might be covered with protein which does not produce molecular hydrogen - either denatured during purification/dialysis or bound in an orientation which blocks the electron acceptor site – and transfers the electrons to other acceptors in the solution.

Just recently, Hambourger et al. reported immobilization of the [FeFe]-hydrogenase *CaHydA* from *Clostridium acetobutylicum* on glassy carbon and carbon felt (Hambourger et al., 2008). Proteins can bind directly on the surface and receive electrons via direct electron transfer on certain forms of graphite. However, quantification of the bound enzymes is not possible on those electrodes, but on a gold electrode as presented here.

The specific hydrogen evolving activity of recombinant *CrHydA1* in solution is measured by established *in vitro* tests to be 760  $\mu\text{mol H}_2 \text{ min}^{-1} \text{ mg}^{-1}$  (Girbal et al., 2005). After dialysis, the average specific activity of the *CrHydA1* samples used in our experiments drops to 130  $\mu\text{mol H}_2 \text{ min}^{-1} \text{ mg}^{-1}$  corresponding to 8500  $\text{mol H}_2 \text{ min}^{-1} \text{ mol}^{-1}$ . This value defines the upper limit of the specific hydrogen evolving activity of the immobilized *CrHydA1*.

Surface plasmon resonance (SPR) is used to quantify the amount of immobilized *CrHydA1*. Binding of the protein to the MPA-modified surface and the exchange of the

buffer with the protein solution change the refractive index and lead to an increase of the SPR response, respectively (Figure 23). Before and after the injection, the surface is rinsed with buffer and the difference in the SPR response is solely attributed to the bound protein. These values are noted in Figure 23 as  $\Delta R_n$  for each protein injection (with  $n$  = number of injection). During the first injection the entire surface of the MPA-SAM is available, while in the following injections only the uncovered parts can bind proteins. Consequently,  $\Delta R_2$  and  $\Delta R_3$  are much smaller than  $\Delta R_1$ . Washing after each injection step removes unspecifically bound proteins. The sum of all three binding steps  $\Delta R_n = 2250$  R.U. reflects the total amount of specifically bound hydrogenase and is calculated to be  $2.25 \text{ ng } CrHydA1 \text{ mm}^{-2}$  (or  $3.42 \times 10^{-12} \text{ mol cm}^{-2}$ ) with the conversion of 1000 R.U. into  $1 \text{ ng protein mm}^{-2}$  (Armstrong et al., 1947; Stenberg et al., 1991).

One molecule of *CrHydA1* covers a surface area between  $23 \text{ nm}^2$  and  $47 \text{ nm}^2$ , depending on its orientation. These values are estimated from a homology modelling structure of *CrHydA1* using the catalytic subunit of *CpI* hydrogenase from *Clostridium pasteurianum* (PDB-ID: 1FEH). From these values the amount of specifically bound *CrHydA1* in a monolayer is calculated to be in the range of  $2.3 - 4.6 \text{ ng } CrHydA1 \text{ mm}^{-2}$  or  $3.5 - 6.9 \times 10^{-12} \text{ mol cm}^{-2}$ . The measured value indicates that a protein monolayer is adsorbed to the surface and the contribution of unspecific multilayer is negligible.



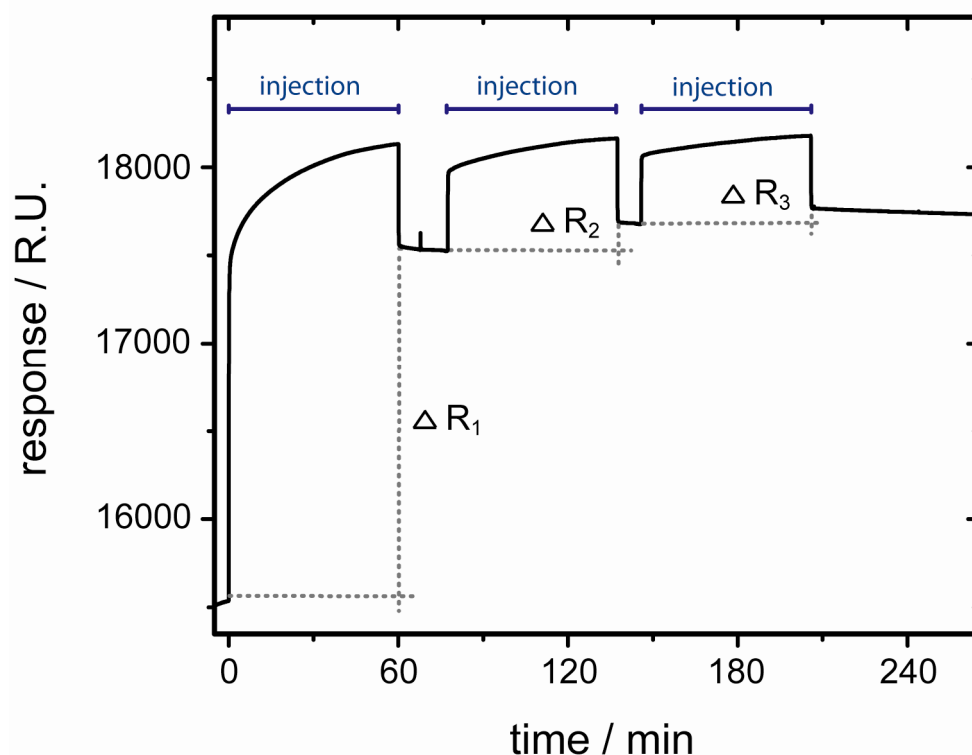


**Figure 23** Surface plasmon resonance signal during the binding of CrHydA1 on an MPA-SAM / The surface is continuously rinsed with buffer at a flow rate of  $5 \mu\text{L min}^{-1}$ . At  $t = 0, 77, \text{ and } 146 \text{ min}$  CrHydA1 is injected for one hour, respectively. The increase in the SPR response is indicated as  $\Delta R_n$  for each injection. ( $\Delta R_1 = 2014 \text{ R.U.}$ ,  $\Delta R_2 = 162 \text{ R.U.}$ ,  $\Delta R_3 = 78 \text{ R.U.}$ )

In the amperometric experiment  $20 \text{ nmol H}_2$  have been produced in 20 minutes. The amount of hydrogen is quantified by gas chromatography (Figure 24). The electrode, which I use, has a geometrical surface area of  $1.45 \text{ cm}^2$  and a surface roughness of 2.5 (Miyake et al., 2002). From these values, the specific hydrogen evolving activity of surface-bound CrHydA1 can be calculated to be  $1.3 \mu\text{mol H}_2 \text{ min}^{-1} \text{ mg}^{-1}$  or  $85 \text{ mol H}_2 \text{ min}^{-1} \text{ mol}^{-1}$ , which is 1% of the activity in the *in vitro* test.

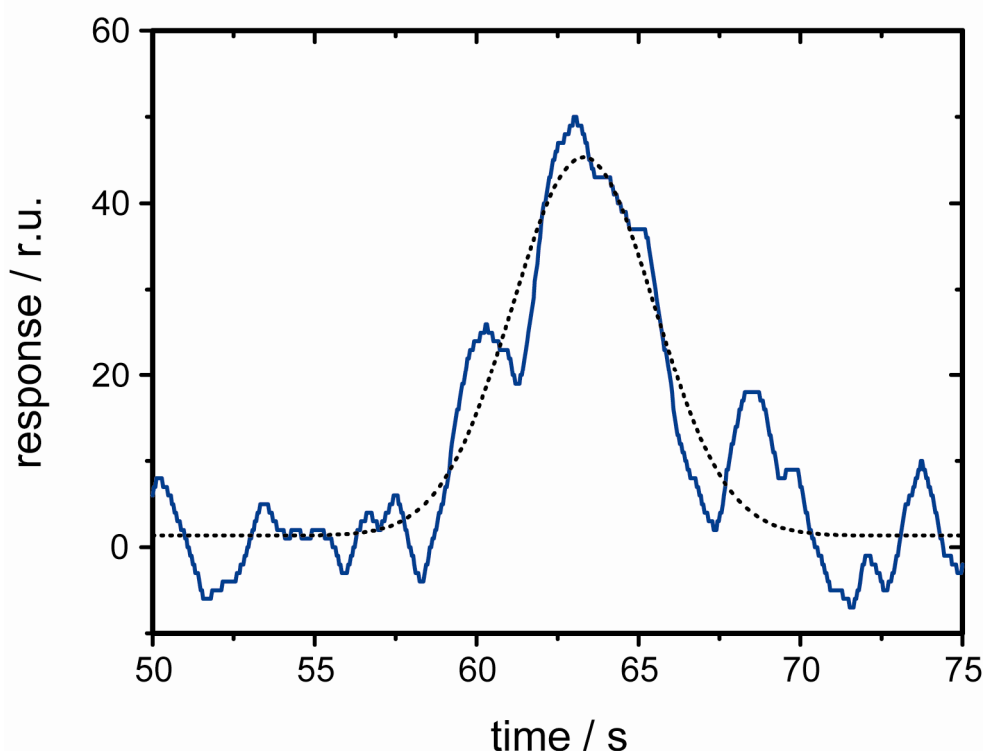


**Figure 24** *Hydrogen production from CrHydA1 on a MPA-SAM* | The hydrogen, which is produced by a CrHydA1-monolayer, is quantified by gas chromatography. A Gaussian curve (black, dotted) is fitted to the measured data (blue).

For the *in vitro* essay, an excess of the strong reductant sodium dithionite is added to immediately re-reduce  $MV^{2+}$  in the vicinity of the electron acceptor site of CrHydA1 and maintain a constant high concentration of reduced  $MV^0$ . Using a protein monolayer, re-reduction of  $MV^{2+}$  takes place close to the electrode surface (tunnelling distance) and  $MV^0$  diffuses a longer distance to the hydrogenase, which limits the reaction rate. Another explanation for the comparatively low activity of the immobilized CrHydA1 is that the access to the electron acceptor site of CrHydA1 might be hindered by the MPA-SAM, compared to the protein in solution (see above). In addition the temperature is 20 °C for the monolayer experiments and 37 °C for the *in vitro* tests, which also contributes to the higher reaction rate in the latter case.

In summary, the design of a catalyst-coated electrode has been shown, which is able to produce hydrogen at a rate of  $1.3 \mu\text{mol H}_2 \text{ min}^{-1} \text{ mg}^{-1}$  (or  $85 \text{ mol H}_2 \text{ min}^{-1} \text{ mol}^{-1}$ ). MV is utilized as a soluble electron mediator between electrode surface and surface-tethered hydrogenase.

#### 4.1.4 Monolayer-mediated electron transfer

Methylviologen (MV) has proven itself to be a suitable electron donor for the [FeFe]-hydrogenase *CrHydA1* (Chapter 4.1.3). Here, a MV derivative was bound to a gold electrode via a thiol group and *CrHydA1* was immobilized on this surface. Electrons were transferred from the gold electrode via the MV monolayer to *CrHydA1*, where they reduced protons to molecular hydrogen (Figure 25).

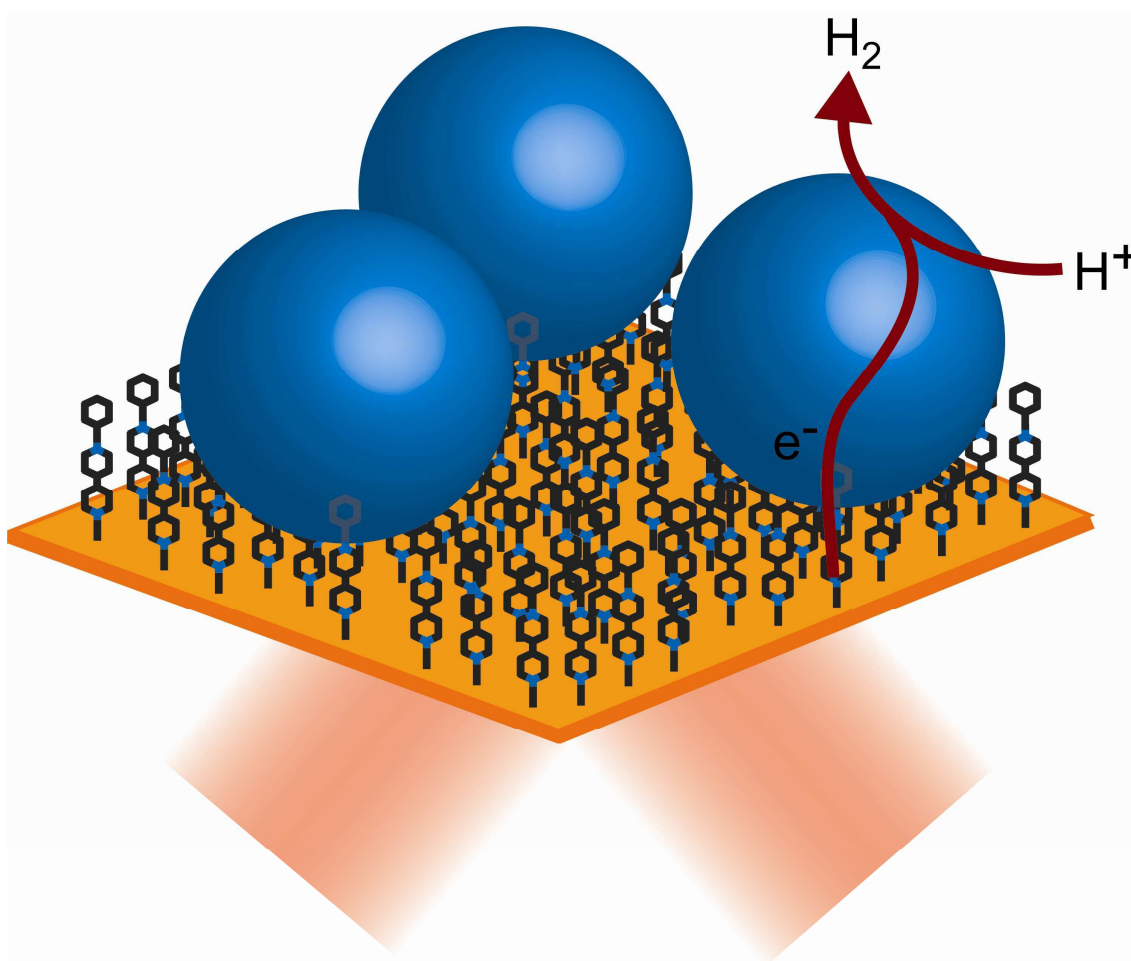


**Figure 25** *CrHydA1* on a redox-active monolayer | The [FeFe]-hydrogenase *CrHydA1* (blue) is immobilized on a redox-active monolayer. Electrons are transferred from the gold electrode, through the monolayer towards the hydrogenase. The surface-tethered molecules are probed by IR spectroscopy. For sake of visual clarity, the size of *CrHydA1* is reduced by a factor of about 2 with respect to the 1-(10-mercaptodecyl)-1'-benzyl-4,4'-bipyridinium molecules.

#### Characterization of the surface-tethered redox mediator

The bipyridinium group is the redox active center of methylviologen. In its oxidized state ( $MV^{2+}$ ) both nitrogen atoms carry positive charges. In the reduction process an electron is transferred to both of the nitrogen atoms and a biradical ( $MV^0$ ) is formed. In

order to immobilize the bipyridinium function on the gold electrode a 10-mercaptodecyl function was synthesized to one of the nitrogen atoms. A benzyl group was bound to the other nitrogen to stabilize the compound during the synthesis. The structure of 1-(10-mercaptodecyl)-1'-benzyl-4,4'-bipyridinium (BBP) is shown in Figure 26. Although both groups are larger than the methyl groups of MV, BBP is able to access the electron acceptor site of CrHydA1. If MV was replaced by BBP for the *in vitro* assay in solution (Chapter 3.2), a hydrogenase activity of 25% was measured.

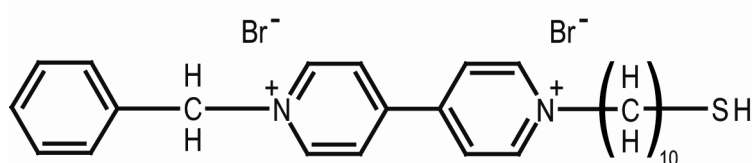


**Figure 26** Chemical structure of BBP | The oxidized form of 1-(10-mercaptodecyl)-1'-benzyl-4,4'-bipyridinium-dibromid is shown as chemical structure.

The binding of BBP to a bare gold surface was monitored *in situ* by SEIRAS (Figure 27). The rising bands were assigned to vibrational modes of BBP (Table 3) and showed the adsorption of BBP molecules to the surface. After approximately 60 minutes the band intensities did not increase any further and a complete monolayer of BBP was formed. The broad, negative band at  $1650\text{ cm}^{-1}$  was assigned to the water bending mode and indicated that water was displaced from the surface, what is consistent with BBP binding.

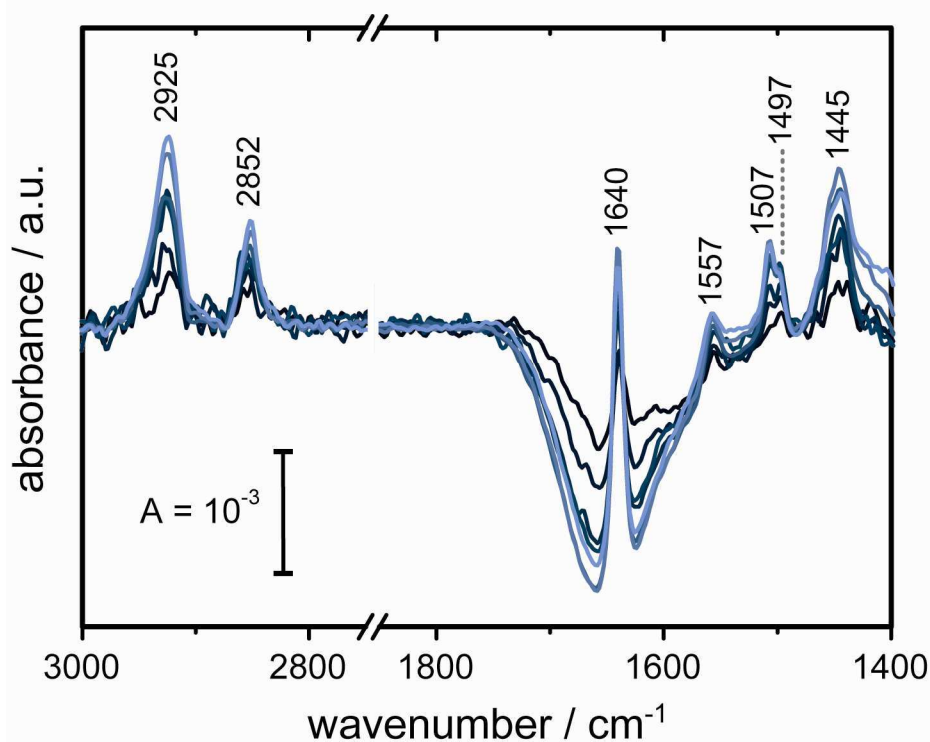


**Figure 27** *BBP binding to a bare gold surface* | The SEIRA spectra are recorded during the binding process of 1 mg/mL BBP to bare gold at 6 s (black), 12 s, 30 s, 1 min, 5 min, 30 min, and 60 min (light blue). The bands are discussed in the text.

Table 3 IR frequencies of BBP

Band position / $\text{cm}^{-1}$	Assigned vibration
2925(+)	Asymmetrical C-H stretching (in $\text{CH}_2$ )
2852(+)	Symmetrical C-H stretching (in $\text{CH}_2$ )
1650(-)	$\text{H}_2\text{O}$ bending
1640(+)	(Hetero-)aromatic ring quadrant stretching
1557(+)	(Hetero-)aromatic ring quadrant stretching
1507(+)	(Hetero-)aromatic ring semicircle stretching
1497(+)	(Hetero-)aromatic ring semicircle stretching
1445(+)	(Hetero-)aromatic ring semicircle stretching

Surface-tethered BBP has a first redox potential of approximately -153 mV (Figure 28, red curve). This redox potential is significantly higher than the redox potential for the two electron reduction of MV in solution (-423 mV, Stombaugh et al., 1976) and thus the reaction of BBP at the surface probably was a different one (see below).

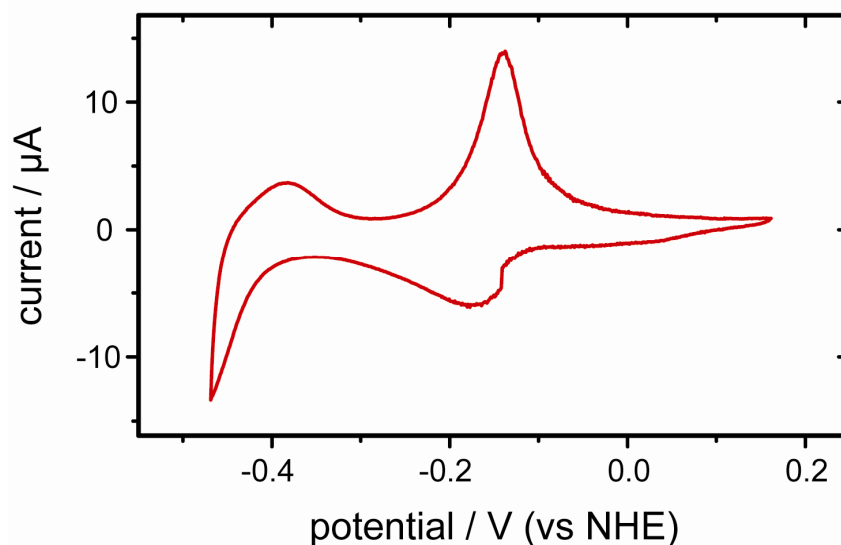


**Figure 28** *Cyclic voltammogram of a BBP monolayer* | A cyclic voltammogram of a BBP monolayer is recorded at a scan rate of  $10 \text{ mV s}^{-1}$  in  $10 \text{ mM}$  potassium phosphate buffer (pH 6.8).

A potential-induced difference spectrum of the BBP monolayer was recorded to monitor the changes during this redox reaction. The background was recorded at  $160 \text{ mV}$  (oxidized state) and the sample spectrum was recorded at  $-240 \text{ mV}$  (first reduced state). Positive bands (Figure 29, black curve) corresponded to vibrations which solely appeared in the first reduced state. The bands at  $1634 \text{ cm}^{-1}$ ,  $1594 \text{ cm}^{-1}$ , and  $1505 \text{ cm}^{-1}$  were assigned to stretching vibrations of the pyridine rings (Table 4) and showed that the redox-induced changes were localized in the bipyridinium ring system. MV and BBP differ in the two groups which are bound to the pyridine rings. The exchange of a methyl group with a mercaptodecyl function is a conservative modification and does not drastically affect the redox potential. The second exchange is a methyl group for a benzyl group. Benzyl substituents have a stronger influence on the ring system and may be able to stabilize a radical on the nitrogen. Thus, it can be presumed that the first redox potential can be assigned to the one electron redox reaction between the benzylic cation ( $\text{BBP}^{2+}$ ) and benzylic radical ( $\text{BBP}^{\cdot+}$ ). The band intensities for the oxidation (red curve) were almost equal to the reduction (black curve) indicating that this redox process was reversible.

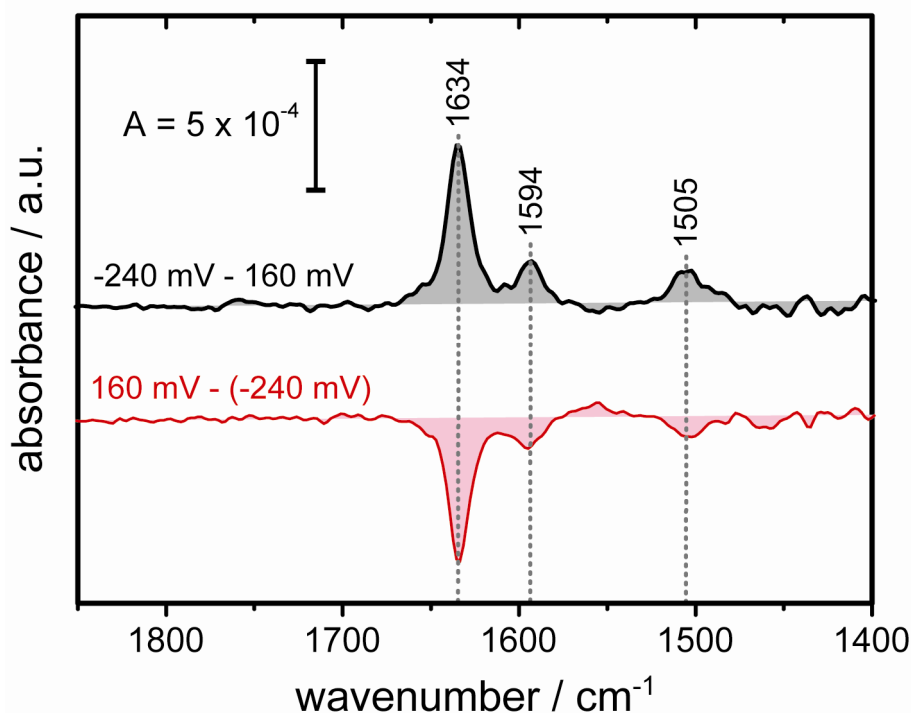


**Figure 29** Potential-induced difference spectra of a BBP monolayer | For the black spectrum, a BBP monolayer is equilibrated at a potential of 160 mV and the reference spectrum is recorded. Then, the potential is changed to -240 mV and the sample spectrum is recorded. The positive bands are assigned to vibrations, which occur only at -240 mV and are discussed in the text. The red spectrum is measured for the back reaction.

Table 4 Redox-induced IR frequencies of BBP

Band position / cm <sup>-1</sup>	Assigned vibration
1634	Heteroaromatic ring quadrant stretching
1594	Heteroaromatic ring quadrant stretching
1505	Heteroaromatic ring semicircle stretching

Below a potential of -385 mV an increase of the reductive current was observed on a BBP monolayer (Figure 28). This can be explained by a second reduction step of BBP (maybe: BBP<sup>+</sup> to BBP<sup>0</sup>) and/or the formation of hydrogen. A potential-induced difference spectrum of this transition was measured (Figure 30).

During the reduction process a positive band was detected at 1661 cm<sup>-1</sup> which was assigned to changes in the ring stretching vibrations, probably due to the reduction of the second bipyridinium nitrogen. In addition, negative bands occurred at 1637 cm<sup>-1</sup>, 1594 cm<sup>-1</sup>, and 1507 cm<sup>-1</sup> (Table 5). These bands had almost the same position and

amplitude (with reversed algebraic sign) as the bands of the first redox process. This indicated that the first reduced form  $\text{BBP}^+$  was consumed. Probably  $\text{BBP}^+$  was further reduced to  $\text{BBP}^{2+}$ .

Another explanation is that the electrons were used to reduce protons to molecular hydrogen. If the electron transfer from  $\text{BBP}^+$  to  $\text{H}^+$  is faster than the re-reduction of  $\text{BBP}^{2+}$ , basically the oxidized form ( $\text{BBP}^{2+}$ ) was monitored by SEIRAS and the negative bands are explained. A third explanation is a re-orientation of the BBP molecules in the electric field. In SEIRAS, only vibrations which change the dipole moment perpendicular to the surface are detected. The part of the perpendicular changes of the dipole moment can be decreased by the re-orientation and cause the negative bands.

The absence of bands in the region between  $3000$  and  $2800\text{ cm}^{-1}$  (C-H stretching of decyl side chain) showed that no desorption process contributed to the spectrum.

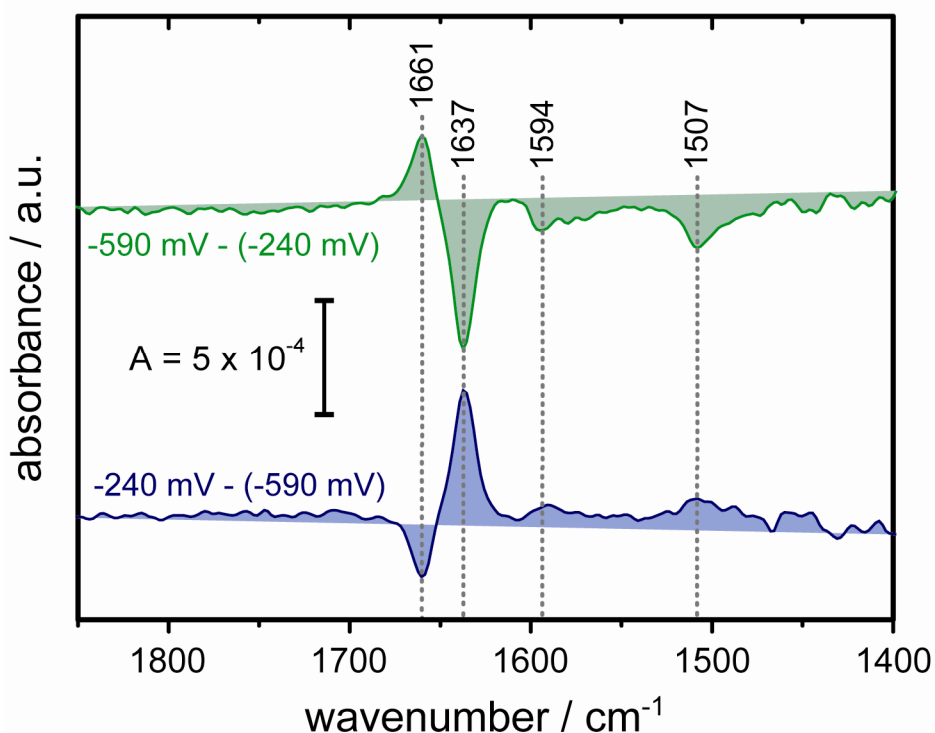


**Figure 30** Potential-induced difference spectra of a BBP monolayer | For the green spectrum, the reference is recorded at a potential of  $-240\text{ mV}$  and the sample at  $-590\text{ mV}$ . The bands are discussed in the text. The blue spectrum is measured for the back reaction.



Table 5 Redox-induced IR frequencies of BBP at low potentials

Band position / $\text{cm}^{-1}$	Assigned vibration
1661	Heteroaromatic ring stretching
1637	Heteroaromatic ring quadrant stretching
1594	Heteroaromatic ring quadrant stretching
1507	Heteroaromatic ring semicircle stretching

#### *Immobilization of the [FeFe]-hydrogenase*

The binding of *CrHydA1* to a BBP-modified surface was monitored *in situ* by SEIRAS (Figure 31). The rising amide I and amide II band indicated accumulation of the hydrogenase in the vicinity of the surface. During the binding process an additional negative band arose at  $1638 \text{ cm}^{-1}$ . This band was assigned to the quadrant stretching vibration of the pyridine ring(s). A band at almost the same position was observed during the first oxidation (Figure 29, red curve). But *CrHydA1* was bound under oxygen-containing atmosphere and the hydrogenase was inhibited by oxygen and unable to oxidize BBP. In addition, the open circuit potential was +80 mV (vs NHE) and the BBP molecules were initially in their oxidized form. Therefore, the band was not assigned to an oxidation of BBP upon *CrHydA1* binding. This was confirmed by the absence of bands at  $1594 \text{ cm}^{-1}$  and  $1505 \text{ cm}^{-1}$ , which were detected in the same oxidation process.

The negative band at  $1638 \text{ cm}^{-1}$  can be explained by the surface selection rules of SEIRAS. The orientation of the BBP molecule was changed with respect to the surface upon *CrHydA1* binding. The perpendicular part of the dipole moment change of the  $1638 \text{ cm}^{-1}$  vibration decreased during the re-orientation and the negative band occurred. During the BBP binding, a positive band was detected at approximately the same position ( $1640 \text{ cm}^{-1}$ , Figure 27) with an intensity of 2.6 mOD. The negative band during the *CrHydA1* binding had a significantly lower intensity of about 0.4 mOD and was likely to result from a reorientation process.

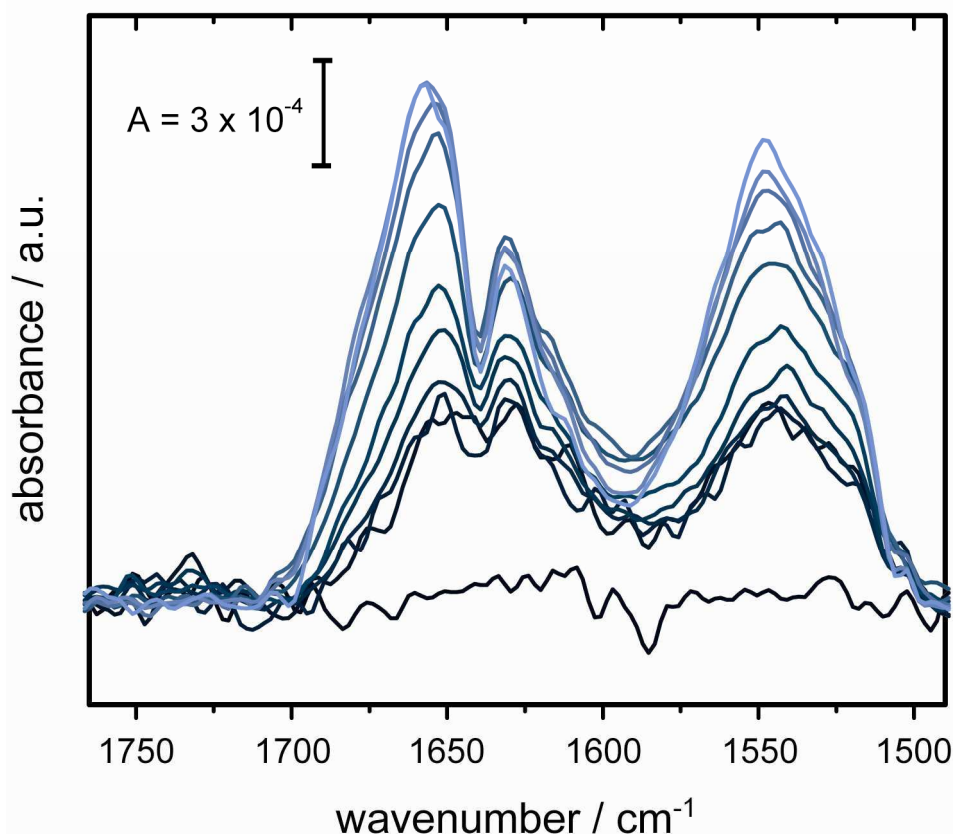


**Figure 31** *CrHydA1 binding to a BBP monolayer* | The displayed SEIRA spectra are recorded at 0 (black) 0.5, 1, 2, 5, 10, 30, 60, 120, 180, and 240 min (light blue) after addition of the protein to a BBP monolayer. The rising bands indicate the binding process and are discussed in the text.

To compare the binding kinetics of *CrHydA1* to different chemically-modified surfaces (Figure 32) the peak height of the amide II bands were normalized to maximum coverage and plotted versus the adsorption time. The fastest binding was observed on an MUA-SAM, 90% of the maximum coverage with *CrHydA1* was reached after 5 minutes. On the shorter carboxy-terminated linker MPA 50 minutes were necessary. The binding to BBP-modified surfaces was significantly slower and took 80 minutes. If a constant potential of -190 mV was applied, and the BBP monolayer was kept in the first reduced state, 90% of the maximum coverage was reached after 70 minutes.

In addition, a mixed monolayer of 1:100 BBP:MPA was used with the aim to provide isolated, well accessible BBP residues, but 90% binding needed about 200 minutes on this layer.

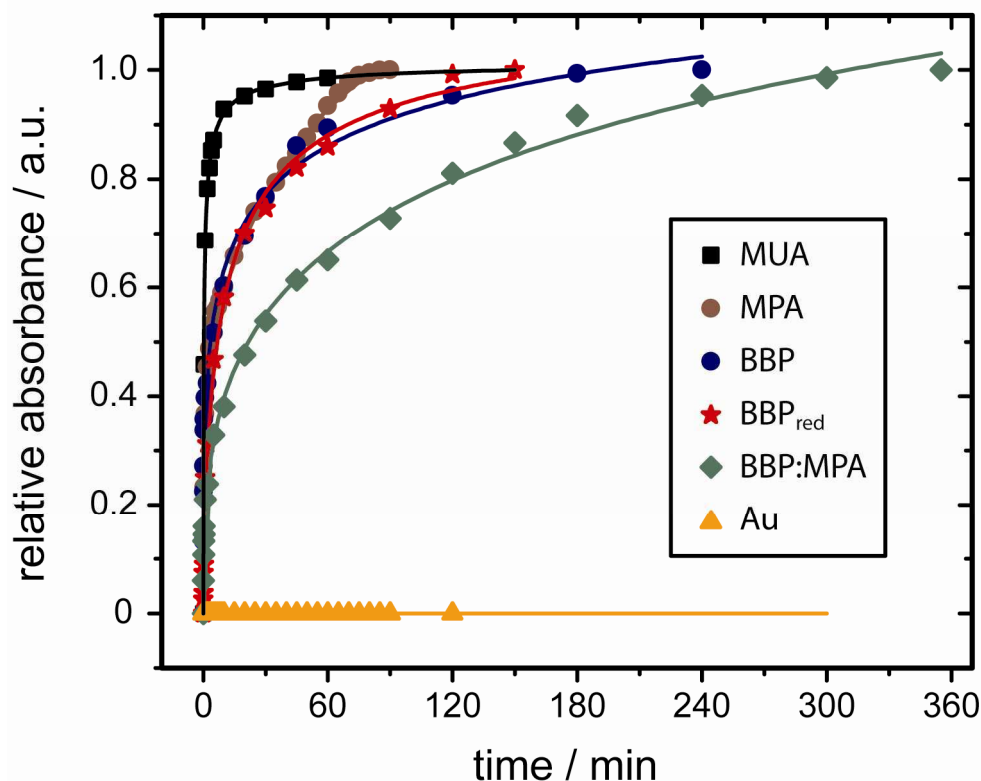


**Figure 32** *Binding kinetics of CrHydA1 on different surfaces* | The binding kinetics of  $3.5 \mu\text{M}$  CrHydA1 to monolayers of MUA (black square), MPA (grey circle), BBP (blue circle), reduced BBP at  $-200 \text{ mV}$  (red star) and to a 1:100 mixture of BBP:MPA (grey/green diamond) are calculated from the respective amide II intensities. The data are normalized to the level of the maximum coverage. Fitted curves are presented as solid lines in the respective colour. All binding experiments are performed at room temperature ( $20 \text{ }^\circ\text{C}$ ).

#### *Activity of a BBP-based CrHYdA1 monolayer*

A cyclic voltammogram of a BBP monolayer was recorded (Figure 33, red curve). The reductive current increased by  $6.2 \mu\text{A}$  upon binding of CrHydA1 (Figure 33, blue curve). This increase clearly showed electron transfer from BBP to the hydrogenase. Compared to the results on carboxy-terminated SAMs (Chapter 4.1.2), the reductive current is three times higher than on an MUA-modified electrode, but reaches only 13% of the amplitude on an MPA-modified electrode.

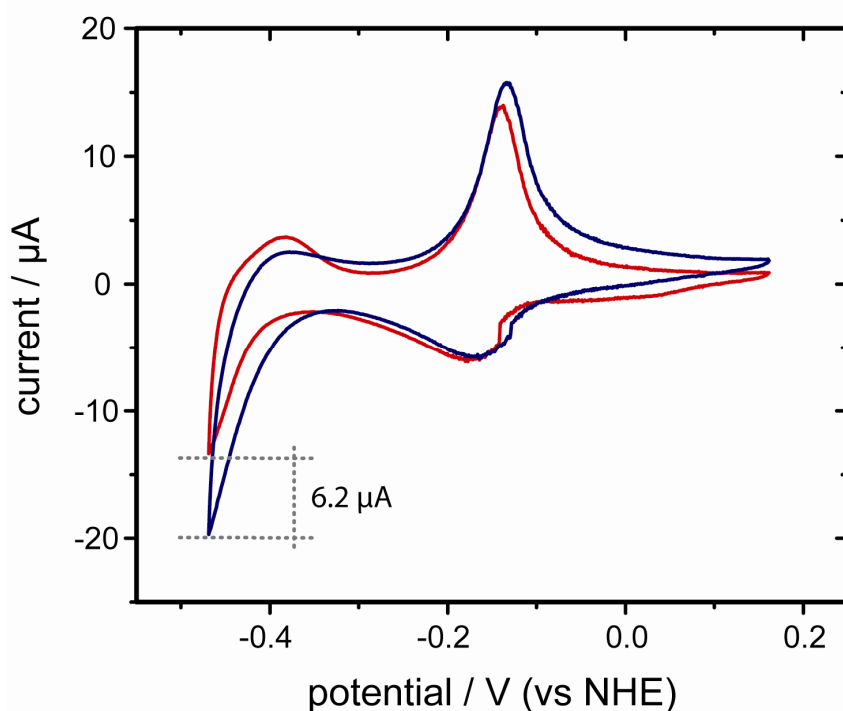


**Figure 33** *Cyclic voltammograms of CrHydA1 on a BBP monolayer* | A cyclic voltammogram of a BBP monolayer is recorded before (red line) and after binding of CrHydA1 (blue line). The difference in the reductive peak currents is due to hydrogen production by the hydrogenase.

To prove that the reductive current depends on CrHydA1 the inhibitory effect of carbon monoxide was monitored by amperometry (Figure 34). A constant potential of -450 mV was applied to the BBP-based CrHydA1 monolayer, CO was injected after 85.3 minutes, and the solution was stirred for 30 seconds to expose the hydrogenase to CO without long delay. The peaks which occurred during injection and stirring were due to mechanical disturbance of the system. CO inhibited the hydrogenase and the amplitude of the reductive current decreased by 125 nA. As additional proof, no hydrogen production was detected after CO was injected.

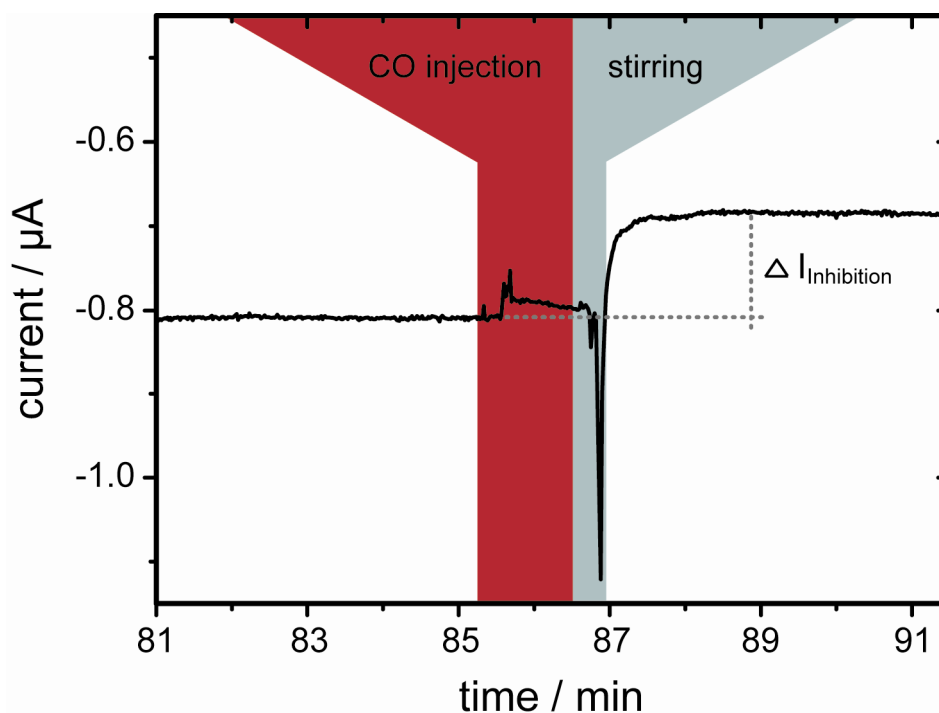


**Figure 34** Amperometry of CrHydA1 on BBP during CO inhibition | A constant potential of -450 mV is applied to a CrHydA1 monolayer, which is bound to a BBP-modified electrode and the current is recorded versus time. After approximately 4 minutes (of stable current), 1 mL carbon monoxide is injected into the system and the solution is stirred for 30 seconds. The decrease of the reductive (negative) current ( $\Delta I_{\text{Inhibition}} = 125 \text{ nA}$ ) is due to the inhibition of the hydrogenase.

Gas chromatography was used, to show that the transferred electrons were consumed to reduce protons and produce molecular hydrogen. After the constant potential of -450 mV was applied for 85 minutes, 1 mL of the gas phase was injected into the gas chromatograph, and the produced hydrogen was calculated from the area of the hydrogen peak (Figure 35) to be 208 nmol. This equates a hydrogen production rate of  $2.4 \pm 0.2 \text{ nmol H}_2 \text{ min}^{-1}$ .

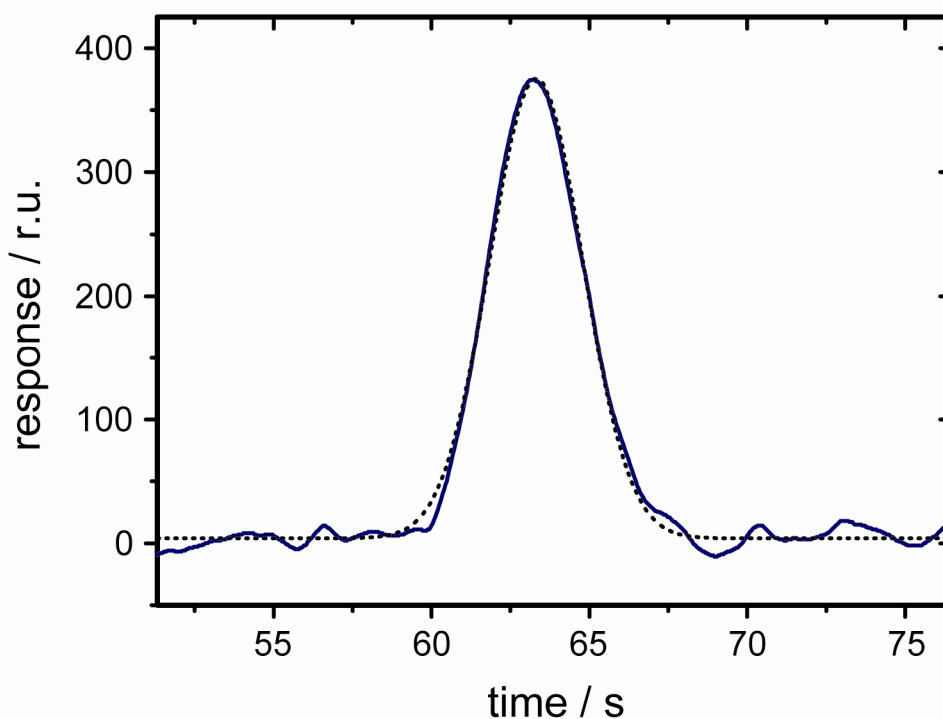


**Figure 35** *Hydrogen production from CrHydA1 on a BBP-SAM* | The hydrogen, which is produced by a CrHydA1-monolayer, is quantified by gas chromatography. A Gaussian curve (black, dotted) is fitted to the measured data (blue). The area of 1423 is equal to 208 nmol of produced hydrogen or 2.4 nmol H<sub>2</sub> min<sup>-1</sup>.

The calculated hydrogen production rate is 2.4 times higher than the rate of the MPA-based system (1 nmol H<sub>2</sub> min<sup>-1</sup>, Chapter 4.1.3), but these values must be corrected for the *in vitro* activity of the hydrogenase. The hydrogenase, which was used for the MPA experiments, had an *in vitro* activity of 130 μmol H<sub>2</sub> min<sup>-1</sup> mg<sup>-1</sup>. For the BBP experiments the preparation of the enzyme had been improved and the *in vitro* activity was increased by a factor of 5 (up to 680 μmol H<sub>2</sub> min<sup>-1</sup> mg<sup>-1</sup>). If these activities are taken into account the MPA-based CrHydA1 monolayer seems to be the more efficient electrocatalyst.

But the BBP-based system has an important advantage for future spectroscopic studies. The electron transfer is mediated by an immobilized monolayer and not limited by the diffusion of a soluble electron carrier. Thus, the system responds faster to a potential change and will allow highly time-resolved SEIRA measurements in the future. Time-resolved IR measurements of the bare BBP-monolayer are currently performed by Kenichi Ataka.

#### 4.1.5 Hydrogen evolution potential

Another important parameter (besides the amount of produced hydrogen) is the most positive potential which allows hydrogen production at the given surface. A more positive hydrogen evolution potential means hydrogen production at lower energy.

In Figure 36 four cyclic voltammograms (pH 6.8, 20 °C) are compared on different electrodes. Each surface exhibited a non-proportional increase of the reductive current at potentials below its hydrogen evolution potential. On a bare gold electrode with methylviologen as electron mediator, hydrogen evolution took place below -460 mV (red curve). By modifying the gold surface with CrHydA1, the hydrogen evolution potential was improved to -335 mV on BBP (green curve) or -290 mV on MPA (blue curve). These characteristic values are close to the potential of -270 mV on platinum surfaces (black curve), which are used in the industry for electrochemical hydrogen production.

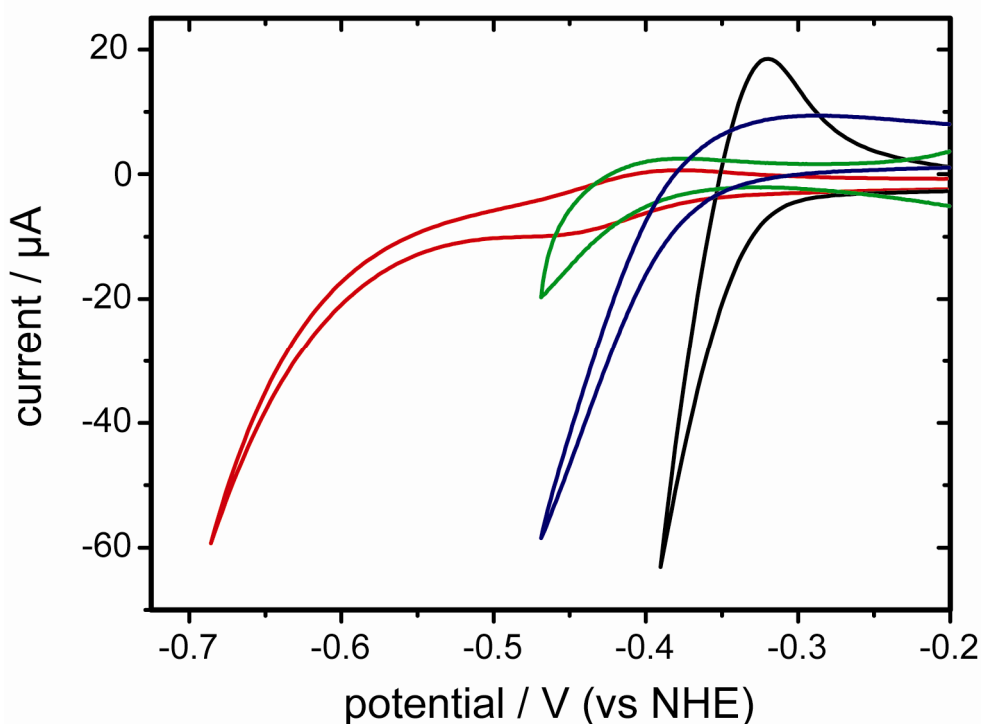


**Figure 36 Hydrogen evolution potential on different surfaces** | Cyclic voltammograms are compared for different surfaces with respect to their hydrogen evolution potentials. If the potential is decreased a non-proportional increase of the reductive current is observed at the respective hydrogen evolution potential. The hydrogen evolution starts at the highest potential on a platinum electrode (black), CrHydA1 on MPA (blue) and BBP (green) need a slightly more negative potential, and the lowest potential is needed on a bare gold electrode (red). The peaks in the red curve between -0.4 and -0.5 V are due to the redox reaction of soluble MV.

#### 4.1.6 Conclusions

The [FeFe]-hydrogenase *CrHydA1* from *Chlamydomonas reinhardtii* was immobilized on various monolayers. When methylviologen was used as a soluble electron carrier, the *CrHydA1*-modified surface was able to catalyze the reduction of protons to molecular hydrogen at a similar potential as platinum electrodes. At a potential of -450 mV 15-17% of the provided electrons were used for hydrogen production.

The catalytic efficiency of the modified gold electrode is rather low in comparison to a graphite-based approach (Hambourger et al., 2008). However, the possibility to investigate the bound protein by surface-enhanced infrared spectroscopy (SEIRAS) and to quantify the amount of bound protein via SPR makes the system a promising approach for in-depth analysis of the specific activity per molecule. This will make it possible to distinguish between different surface populations of the hydrogenase and optimize the electrode to highest activity. The system can be used to probe the specific redox activity and efficiency of variable hydrogenase and protein films in general – as a platform technology for further investigations.

A BBP monolayer has a high affinity for *CrHydA1* and is able to mediate the electron transfer between electrode and hydrogenase. In this setup, the response of the hydrogenase to an external potential is not delayed by a diffusion process, because the redox-active monolayer replaces the soluble electron carrier. This is the first step towards time-resolved, potential-induced surface-enhanced infrared difference absorption spectroscopy (SEIDAS).



## 4.2 Coupling of hydrogen production and photosynthesis

The strategy of this study is to bind photosystem I (PS1) and the hydrogenase (MBH) to each other – in a way that allows direct electron transfer between both proteins. The PsaE subunit of PS1 from *Synechocystis sp. PCC 6803* is deleted from PS1 (PS1 $_{\Delta\text{PsaE}}$ ) and genetically fused to the oxygen-tolerant (Ludwig et al., 2009) hydrogenase (MBH $_{\text{PsaE}}$ ) from *Ralstonia eutropha*. PS1 $_{\Delta\text{PsaE}}$  and MBH $_{\text{PsaE}}$  spontaneously assemble and yield PS1 with a hydrogenase bound close to the electron donor site of PS1 (F $_{\text{A/B}}$ ) (Figure 37).

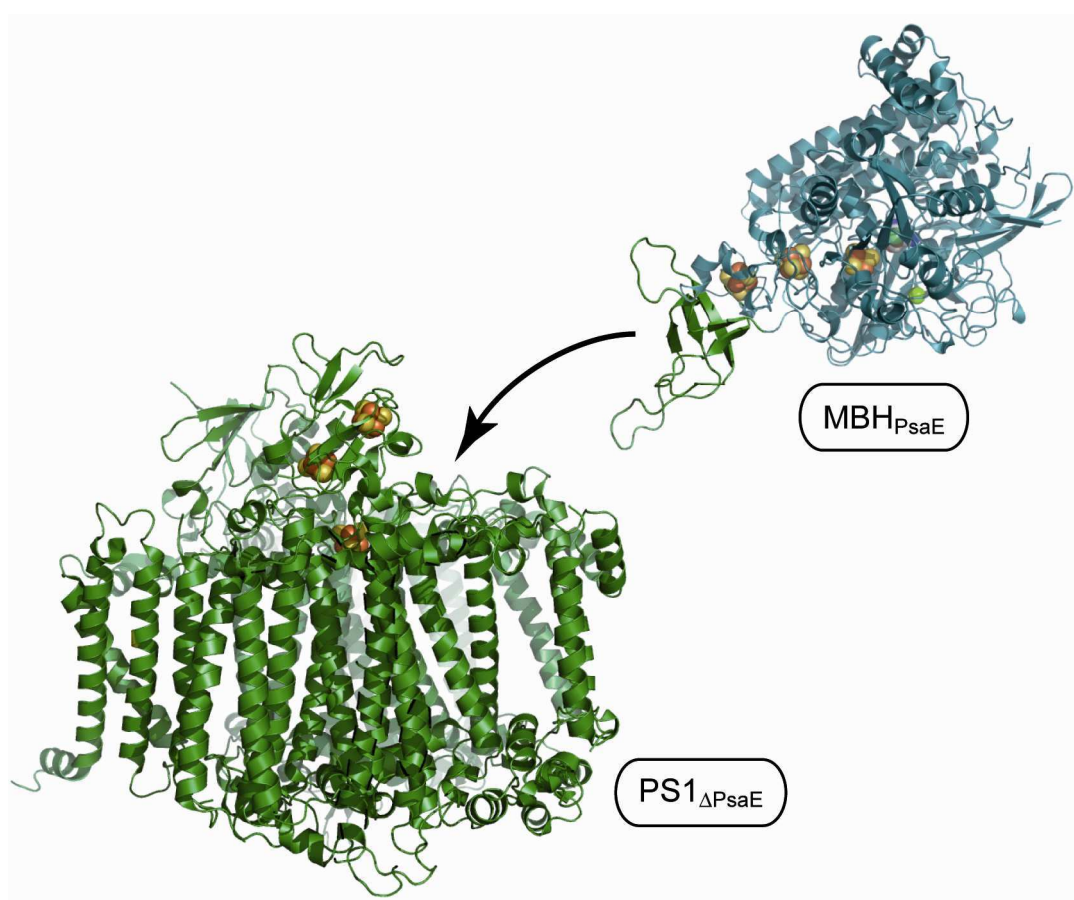


**Figure 37** Coupling concept of hydrogenase and photosystem I | The subunit PsaE of PS1 is deleted from PS1 (PDB-ID: 1JB0) and genetically fused to the MBH (based on PDB-ID: 2FRV). The affinity between PsaE and its native position in PS1 allows a spontaneous assembly to a functional hybrid complex.

It has been demonstrated that PsaE is crucial for electron transfer between F $_{\text{A/B}}$  and the native electron acceptor ferredoxin (Sonoike et al., 1993). Thus, PsaE represents the optimal position for binding of MBH.

A similar protein complex was investigated in solution (Ihara et al., 2006) but hydrogen production could not be quantified on a molecular level with respect to the functional complex. In my measurements, the hybrid complex was bound to the solid support of a gold electrode and the quantification became possible by a combination of various surface sensitive techniques. It was shown by surface-enhanced infrared absorption spectroscopy and electrochemistry that both proteins specifically assembled on the surface and electrons were transferred between both proteins, respectively. Surface plasmon resonance and gas chromatography were applied to quantify the specific hydrogen evolution activity per molecule (and per surface area)

In the surface-tethered system, electrons were provided by a gold electrode, transferred to the photosystem I by a soluble electron carrier (PMS), and conducted to the hydrogenase where the electrons reduced protons to molecular hydrogen (Figure 38).

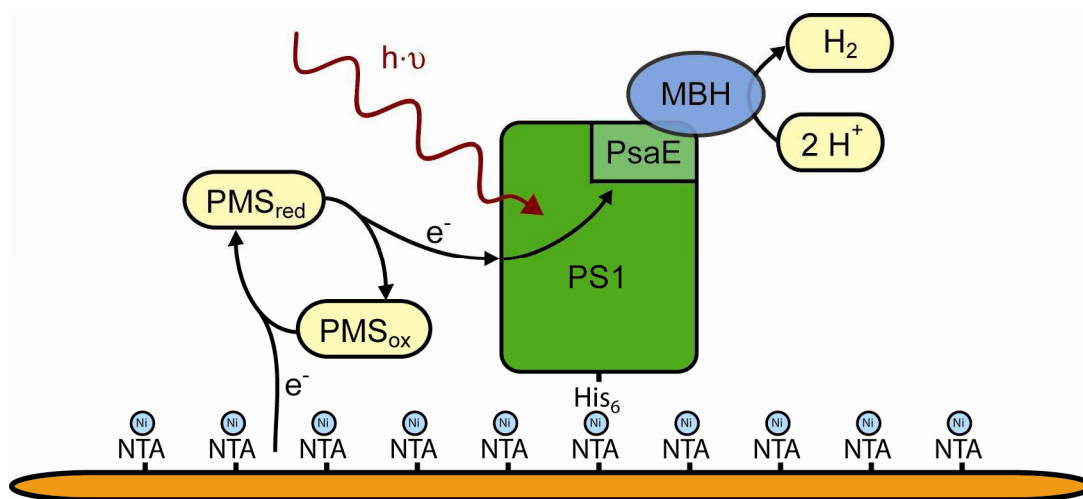


**Figure 38** *Electron flow for light-induced hydrogen production* | Electrons reduce the oxidized form of PMS at the gold surface. PMS transfers electrons to the chlorophyll a dimer (P700) in photosystem I, where it is promoted to a higher energy level upon illumination. After passing the electron transfer chain inside PS1 the electron is transferred to the distal iron-sulfur cluster of the hydrogenase (MBH) and further to the active site where protons are reduced to molecular hydrogen.

#### 4.2.1 Assembly of photosystem I and [NiFe]-hydrogenase

In the first step of assembly of the photosynthetic hydrogen generation complex, PsaE-depleted PS1 (PS1<sub>ΔPsaE</sub>) was attached to the electrode surface via histidine-tag/Ni-NTA interaction. The chemical modification of the gold electrode to form a Ni-NTA terminated surface and the mechanism of protein binding was described before (Chapter 3.3.1). Concentrated PS1<sub>ΔPsaE</sub> solution was injected into the bulk electrolyte to yield a final concentration of 0.5 μM. Since the PsaF subunit of PS1<sub>ΔPsaE</sub> was equipped with an

N-terminal histidine10-tag, the protein was specifically adsorbed onto the surface. This strategy led to the attachment of PS1 $_{\Delta\text{PsaE}}$  with PsaF oriented towards the surface, and leaving the PsaE site exposed to the bulk solution. Two prominent bands were observed in the SEIRA spectrum of the immobilized deletion mutant PS1 $_{\Delta\text{PsaE}}$  (Figure 39). The amide I (predominantly C=O stretching vibration of the peptide bond) and amide II (C=N stretching coupled to N-H bending vibration) bands occurred at 1653  $\text{cm}^{-1}$  and 1545  $\text{cm}^{-1}$ , respectively (Lewis and McElhaney, 2002).

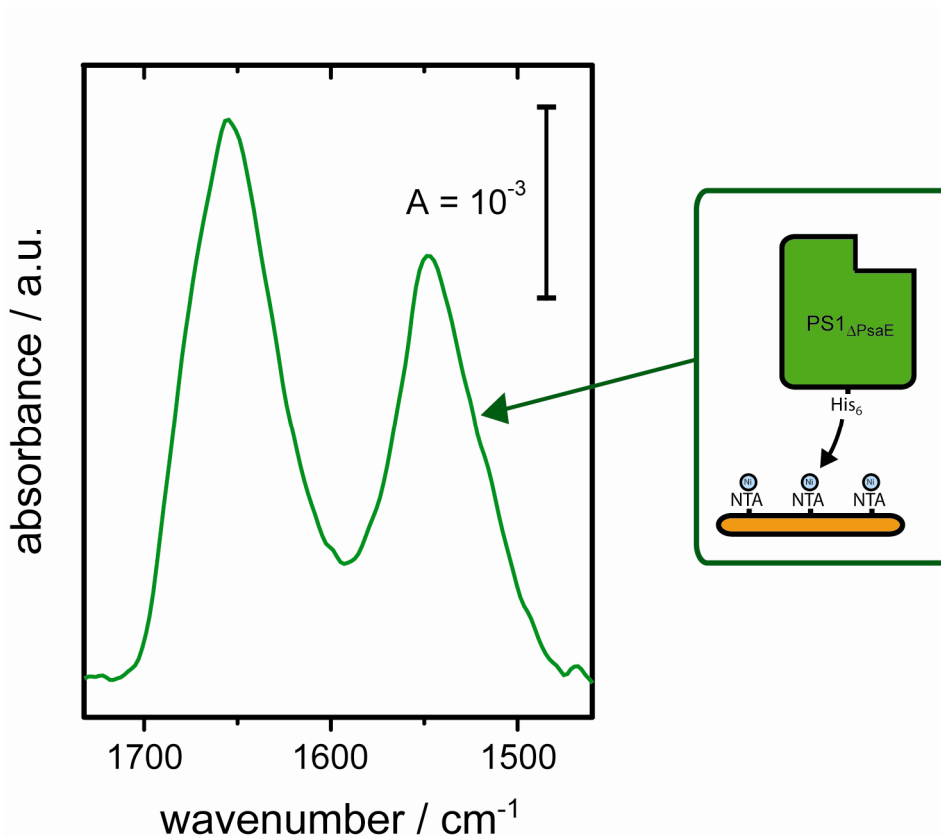


**Figure 39** *PS1 $_{\Delta\text{PsaE}}$  binding to a Ni-NTA monolayer* | A Ni-NTA-terminated gold surface is incubated with a 0.5  $\mu\text{M}$  solution of PS1 $_{\Delta\text{PsaE}}$  for 130 minutes. The SEIRA spectrum (left) is recorded after the binding process is finished. The appearance of amide I (1653  $\text{cm}^{-1}$ ) and amide II (1545  $\text{cm}^{-1}$ ) bands show that the deletion mutant is immobilized on the gold surface. The binding process is schematically depicted on the right.

It was demonstrated that isolated PsaE spontaneously binds to its native position in PsaE-depleted PS1 to re-establish the fully functional photosynthetic complex (Cohen et al., 1993; Lushy et al., 2002). This affinity was used to bind a fusion construct of PsaE and MBH to PsaE-free PS1. The binding process was monitored *in situ* by SEIRAS (Figure 40(A)). When the monolayer of PS1 $_{\Delta\text{PsaE}}$  was incubated with a 1.4  $\mu\text{M}$  solution of the fusion protein MBH $_{\text{PsaE}}$  or isolated PsaE, saturation was reached within 2 hours in

both cases. The similar kinetics suggests that both proteins are bound by the same interaction which is not significantly influenced by the fused hydrogenase (Figure 40(B)).

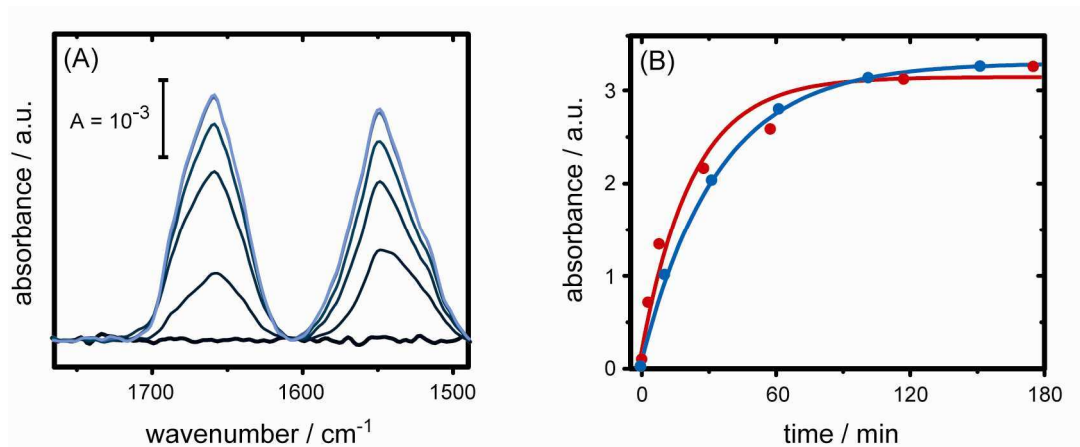


**Figure 40** Binding kinetics of PsaE to its native position in PS1 | (A) A monolayers of PS1 $_{\Delta\text{PsaE}}$  is incubated with 1.4  $\mu\text{M}$  MBH<sub>PsaE</sub>. The spectra are recorded at  $t = 0$  (black), 9, 30, 60, 100, and 150 minutes (light blue). 910 scans are averaged for each spectrum. (B) The intensities of the amide II bands are plotted versus the time for 1.4  $\mu\text{M}$  MBH<sub>PsaE</sub> (blue) and 1.4  $\mu\text{M}$  PsaE (red).

However, the kind of interaction between MBH<sub>PsaE</sub> and PS1 $_{\Delta\text{PsaE}}$  has to be checked, because unspecific interactions are possible, which form non-functional complexes. The fusion protein might interact with the surface of PS1 or with the unoccupied parts of the Ni-NTA monolayer by electrostatic interaction.

To quantify the fraction of specifically bound MBH<sub>PsaE</sub>, the affinity of MBH<sub>PsaE</sub> to monolayers of PS1 $_{\Delta\text{PsaE}}$ , PS1, and Ni-NTA were compared. The absorption changes were followed *in situ* by surface-enhanced infrared absorption (SEIRA) spectroscopy (Figure 41). After incubation with MBH<sub>PsaE</sub>, the surface was intensely washed with buffer to remove weakly bound protein. The SEIRA spectra of the immobilized fusion protein MBH<sub>PsaE</sub> showed two prominent bands at 1660  $\text{cm}^{-1}$  and 1549  $\text{cm}^{-1}$ , which were assigned to the amide I and amide II vibrations, respectively. The maximum intensity of the amide I band at 1660  $\text{cm}^{-1}$  reflects the predominant  $\alpha$ -helical structure of MBH. The amide bands are solely attributed to the adhered fusion protein because the absorption of the modified gold surface was used as the reference spectrum.

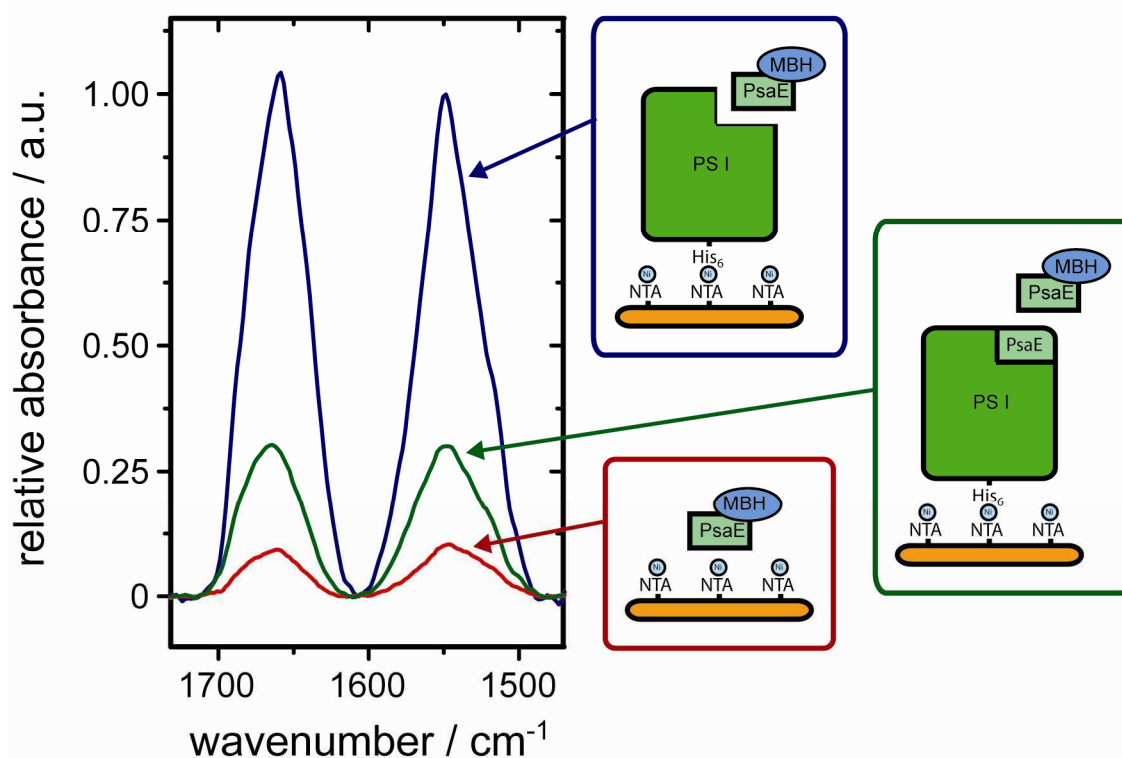


**Figure 41** Binding of the fusion protein  $MBH_{PsaE}$  to different modified surfaces | Monolayer of the  $PsaE$ -free photosystem I ( $PSI_{\Delta PsaE}$ ) (blue), “full” photosystem I ( $PSI$ ) (green) and Ni-NTA (red) are incubated with a  $1.4 \mu M$  solution of  $MBH_{PsaE}$ , respectively. The intensities of amide I ( $1660 \text{ cm}^{-1}$ ) and amide II band ( $1549 \text{ cm}^{-1}$ ) are proportional to the amount of immobilized fusion protein. (The spectra are normalized to the surface enhancement factor of the respective gold surface and to 1 for the amide II intensity of the blue curve). The three experiments are schematically depicted on the right.

In order to compare the relative amount of adsorbed  $MBH_{PsaE}$ , the integrated areas of the amide II bands were compared. For the immobilization on the  $PSI_{\Delta PsaE}$ -modified surface (Figure 41, blue curve) the integral area was the largest and set to 100% (maximum binding). Specific assembly (binding of the  $PsaE$  subunit of the fusion protein to its native place in  $PSI$ ) and all possible unspecific interactions contributed to this value. For binding of the fusion protein to a  $PSI$  layer (Figure 41, green curve), the area was only 37% of the maximum binding. The  $PSI$  layer allowed almost the same unspecific interactions as a layer of the  $PsaE$  free mutant, but the specific interaction between  $MBH_{PsaE}$  and the deletion site of  $PsaE$  were blocked, because the protein did not lack  $PsaE$ . This suggests that the difference between both measurements (approximately 2/3 of the maximum binding) was due to specifically bound fusion protein, which formed a functional hybrid complex.

For the binding to a bare Ni-NTA layer (Figure 41, red curve) the area was only 11% of the maximum binding. This indicates that most unspecific interactions occurred between the fusion protein and the surface of PS1.

#### 4.2.2 Quantification of the hybrid complex

Immobilization of  $\text{MBH}_{\text{PsaE}}$  on a  $\text{PS1}_{\Delta\text{PsaE}}$  monolayer was also monitored by surface plasmon resonance (SPR). The fusion protein was injected into the flow system for 325 min. The binding of the protein and the exchange of buffer with protein solution changed the refractive index in the vicinity of the surface and lead to an increase of the SPR response, respectively. Because both effects occurred on the same time scale (at the used flow rate of  $1 \mu\text{L min}^{-1}$ ) the dissociation constant  $K_d$  could not be determined. But the total difference of the SPR response before and after the protein injection was solely attributed to the bound fusion protein. At those time points the surface was rinsed with buffer until the SPR response became stable and no solution mixing contributed to the SPR response.

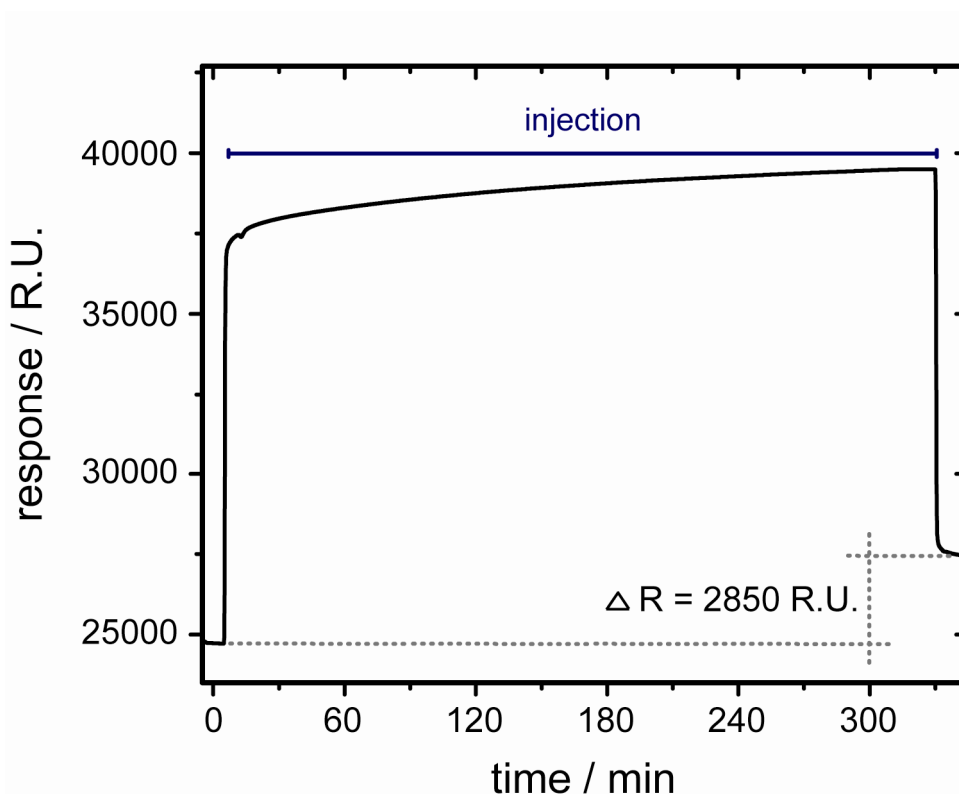


**Figure 42** Surface plasmon resonance signal during the assembly of  $\text{MBH}_{\text{PsaE}}$  / A  $\text{PS1}_{\Delta\text{PsaE}}$  monolayer is continuously rinsed with buffer at a flow rate of  $5 \mu\text{L min}^{-1}$ . At  $t = 5 \text{ min}$   $1.4 \mu\text{M}$   $\text{MBH}_{\text{PsaE}}$  is injected for 325 minutes. The difference in the SPR response before and after the injection is indicated as  $\Delta R$ .

The SPR response increased by 2850 R.U. Taking this value, the protein coverage was calculated to be 2.85 ng MBH<sub>PsaE</sub> mm<sup>-2</sup> (or 2.5 x 10<sup>-12</sup> mol MBH<sub>PsaE</sub> cm<sup>-2</sup>). To determine the conversion factor, the binding of several radioactive-labelled, soluble proteins was monitored by SPR. The correlation of radioactivity and SPR response yielded a conversion factor of 1 ng protein mm<sup>-2</sup> per 1,000 R.U. (Armstrong et al., 1947; Stenberg et al., 1991). As the SEIRA spectroscopy showed that about 2/3 of the fusion protein were bound specifically to PS1<sub>ΔPsaE</sub>, the amount of hydrogenase specifically immobilized on PS1<sub>ΔPsaE</sub> was 1.9 ng MBH<sub>PsaE</sub> mm<sup>-2</sup> (or 1.6 x 10<sup>-12</sup> mol cm<sup>-2</sup>).

#### 4.2.3 Functional testing - Photocurrent

The genetic fusion of PsaE and MBH was made to bring the electron acceptor site of MBH and the electron donor site of PS1 close to each other and thus allow direct electron transfer.

Amperometry was used to experimentally verify the light-induced electron transfer (photocurrent) from PS1 to the MBH. The electron flow is depicted in Figure 38. The redox properties of the soluble electron carrier N-methylphenazonium methyl sulphate (PMS) were investigated by cyclic voltammetry. The midpoint potential of PMS was determined as mean value of oxidative and reductive peak potential to be +85 mV (Figure 43).

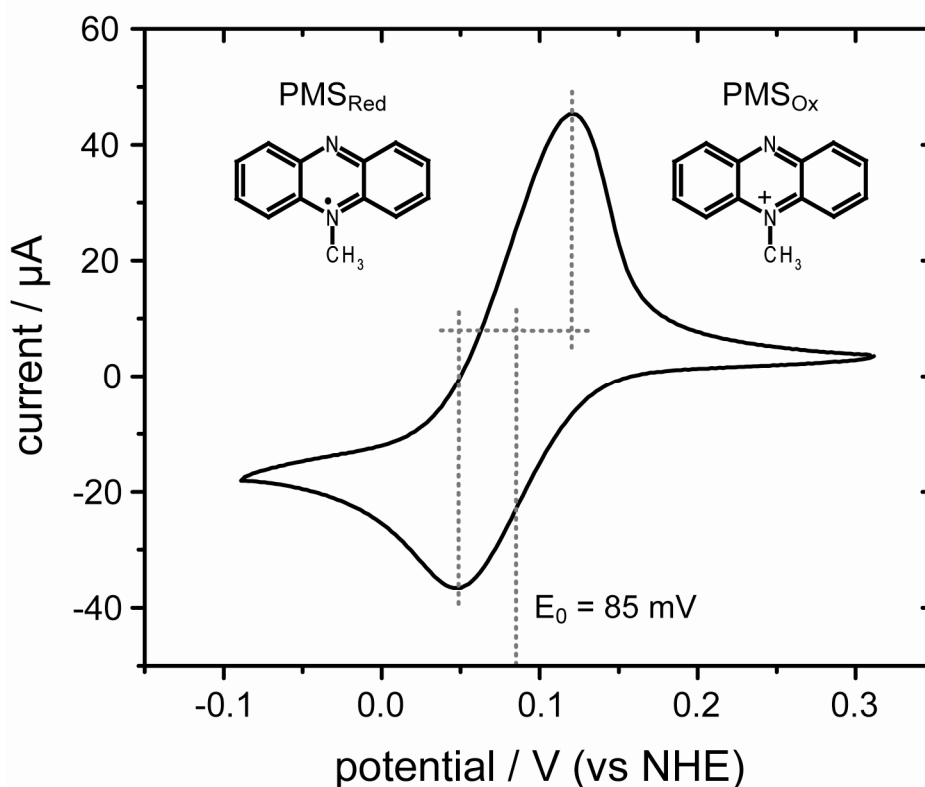


**Figure 43** *Cyclic voltammogram of PMS* / Cyclic voltammetry is used to measure the mid-point potential of a 75  $\mu\text{M}$  PMS solution. The mid-point potential is graphically determined as the average potential of oxidative and reductive peak potentials. At low potentials PMS is mostly in the reduced state (top left) and high potentials PMS is dominated by the oxidized state (top right).

At an external potential of -90 mV (vs NHE), PMS was reduced to the semiquinone (Zaugg et al., 1964) by the electrode. Reduced PMS diffused towards the electron acceptor site of PS1. There, an electron was transferred to the reaction center P700 whose potential was lifted upon red light illumination and electron transfer to the active site of MBH ensued. Here, the electrons were used to reduce protons from the bulk to molecular hydrogen. Oxidized PMS separated from PS1 and diffused to the electrode where it was re-reduced. This reduction was measured as a light-induced current which is proportional to the activity of PS1.

The PS1 <sub>$\Delta$ PsaE</sub> monolayer exhibited a photocurrent of 200 nA (Figure 44, green curve). After binding of the fusion protein, the hydrogenase acted as the acceptor for the electrons which were provided by PS1. Upon the formation of the functional hybrid complex PS1-MBH, the photocurrent increased to an average amplitude of 300 nA (Figure 44, blue curve). However, it is not possible to distinguish by electrochemical methods whether the electrons were consumed by hydrogen production or directly transferred to the counter electrode (e.g. by oxygen species in the solution). In both



cases, PS1 donated electrons and was able to accept further electrons from PMS. This electron transfer was measured as a photocurrent. The increase of the photocurrent by 50% upon assembly of the hybrid complex indicates that the binding of MBH brought a suitable electron acceptor close to the electron donor site of PS1 and increased the electron transfer rate. For comparison, a bare gold surface was illuminated under the same conditions (Figure 44, red curve) and exhibited only capacitive currents (the peaks when the light is switched on and off).

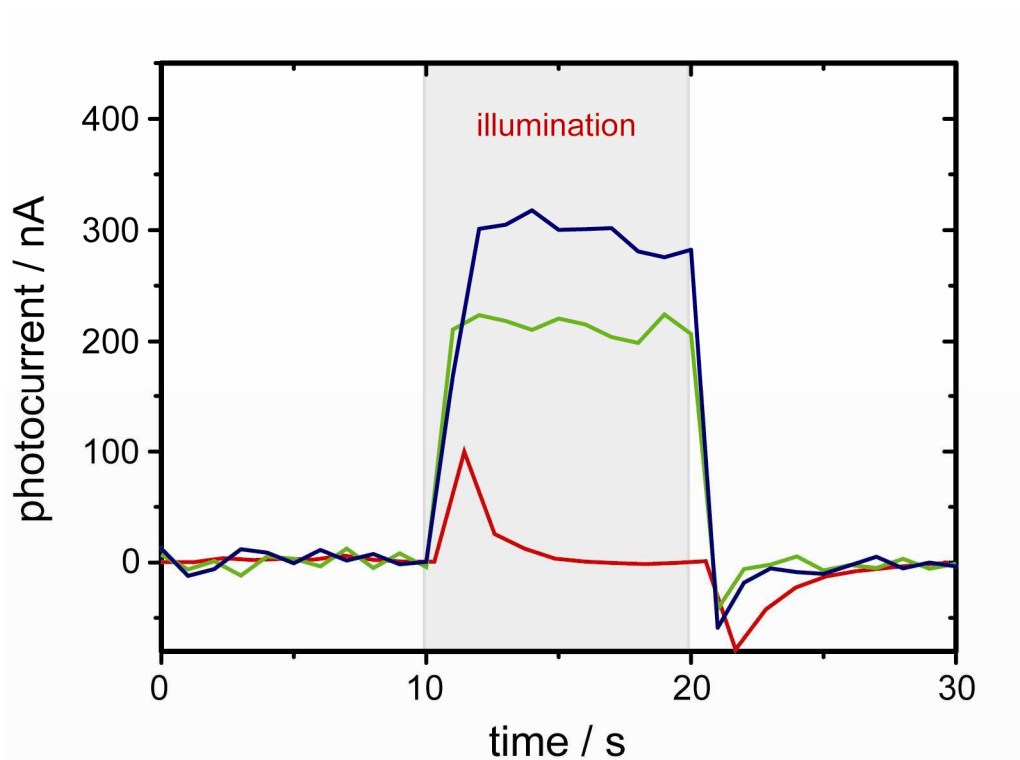


**Figure 44** Photocurrent measurement of the hybrid complex PS1-MBH | A bare gold surface (red) and monolayers of PS1 $\Delta$ PsaE (green) and PS1-MBH (blue) are equilibrated at a constant potential and illuminated for 10 seconds. Upon illumination an additional current of 206 nA is detected for PS1 $\Delta$ PsaE and 297 nA for the hybrid complex. The additional current is named photocurrent and is consistent with electron transport from the working electrode to PS1. Only capacitive current is detected for the bare gold surface. (PMS is used as soluble electron carrier.)

In order to confirm that the photocurrent is dependent on PS1, we measured action spectra of the hybrid complex (Figure 5, open circles) and the PsaE deletion mutant (black stars). The data points reproduce the absorption spectrum of PS1 $\Delta$ PsaE very well (Figure 5, red curve), which strongly suggests that PS1 was involved in the reaction which caused the photocurrent. The broadening and slight red shift of the action spectrum was due to the half-width of the interference filters (~15 nm) and an

interaction between PS1 and gold substrate might contribute as well (Salomon et al., 2007).

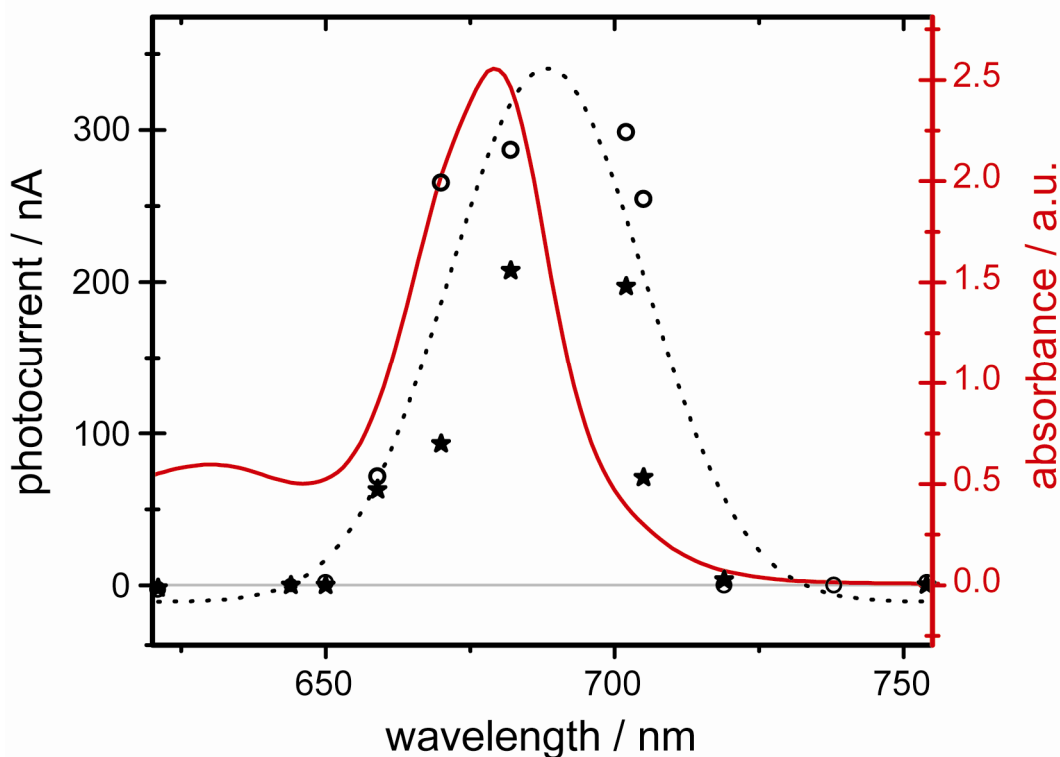


**Figure 45** Action spectrum of PSI monolayers | PsaE-free PSI  $PSI_{\Delta PsaE}$  (stars) and the hybrid complex PSI-MBH (open circle) are immobilized on the surface and illuminated with different wavelengths. The photocurrents are normalized to the PSI coverage which is calculated from the intensity of the amide II band and the surface enhancement factor. The red curve shows the absorption spectrum of  $PSI_{\Delta PsaE}$  in solution for comparison.

The photocurrent also depends on the pH of the solution (Figure 46). The highest photocurrents were measured for pH 7.5 (190 nA) and pH 4.5 (225 nA). The pH does not significantly influence the redox properties of the soluble electron carrier PMS, but affects the proteins. The catalytic reaction of the hydrogenase consumes protons and thus is faster at lower pH. This can explain the high photocurrent at pH 4.5. If the pH was decreased further the system became less stable and the photocurrent decreased with time. The value of 190 nA was measured 5 min after changing the pH to a value of 3.5. The high photocurrent at pH 7.5 can not be explained in terms of hydrogenase activity. I propose that this pH mostly increased the reaction rate of PS1.

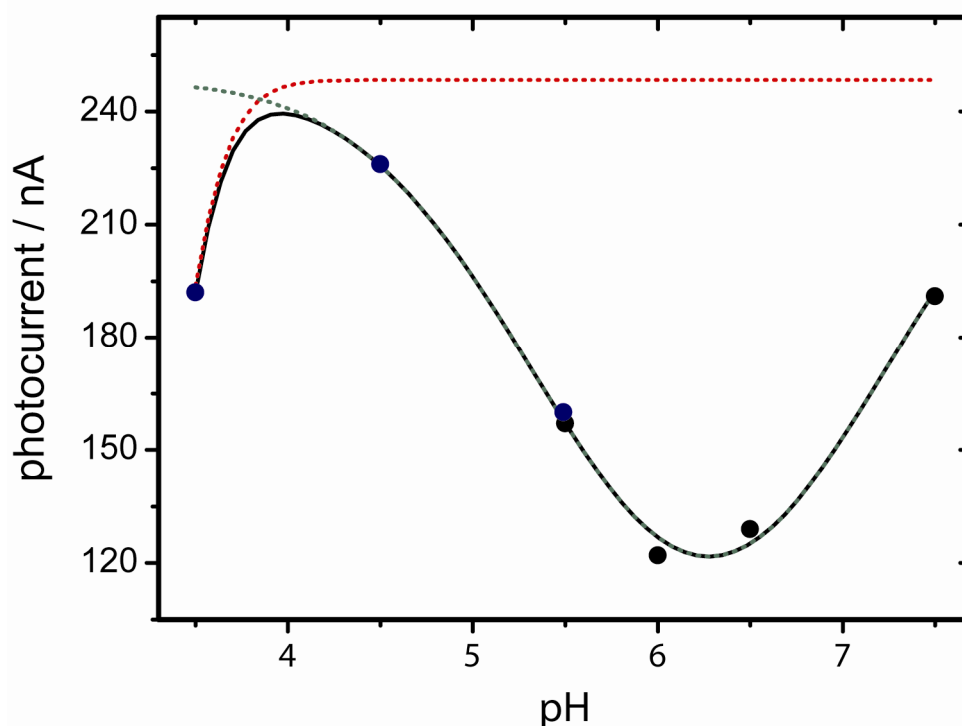


**Figure 46** *pH dependence of the photocurrent of PS1-MBH* | The photocurrent of a PS1-MBH monolayer is measured at different pH values under red light illumination. The pH region between 7.5 and 5.5 (black) is measured in the standard protein buffer (20 mM HEPES); for more acidic pH values (5.5 to 3.5) (blue) 20 mM acetate buffer is used. Dotted curves are fitted to the experimental values and present the predicted, continuous pH dependence.

#### 4.2.4 Light-induced hydrogen evolution

The electrons, which are provided by PS1, are not necessarily consumed by hydrogen production. They can also be directly transferred to the counter electrode. Thus, the hydrogen, which is produced by a PS1-MBH monolayer, must be determined by gas chromatography. Molecular hydrogen was accumulated during a time interval of 30 minutes and the rate of  $H_2$  production per time and electrode area was calculated.

Upon illumination, the immobilized hybrid complex PS1-MBH generated molecular hydrogen at a rate of  $120 \pm 30 \text{ pmol } H_2 \text{ s}^{-1} \text{ cm}^{-2}$  at an electrode potential of -90 mV (to re-reduce PMS). After 30 min of illumination the activity of the monolayer was reduced to ~50% due to photo damage (Figure 49). Surprisingly, residual hydrogen production could be detected even in the absence of MBH (~25% rate of  $H_2$  production for a monolayer of  $PS1_{\Delta PsaE}$ ). This observation suggests that electrons provided at the donor site of PS1 ( $F_A/F_B$ ) can be directly used to reduce protons to molecular hydrogen. The electrons at  $F_A/F_B$  have a potential of -0.54 V and -0.59 V, respectively (Evans and

Heathcote, 1980). These potentials are insufficient to produce H<sub>2</sub> at a bare gold electrode at the used pH of 7.5 (Krassen et al., 2009). It is known, however, that the overpotential for hydrogen production (on metal electrodes) is reduced by the addition of small organic molecules, like 4,4'-bipyridine (Uchida et al., 2008), methyl viologen (Tamamushi and Tanaka, 1987), or pyridine (Hamelin et al., 1990, 1991). Thus, it seems likely that H<sub>2</sub> production occurs in the protein environment of a high-energetic iron-sulfur cluster but at a low rate.

Three control experiments were performed: (1) In the dark, the hybrid complex did not produce a significant amount of hydrogen (< 20 pmol H<sub>2</sub> s<sup>-1</sup> cm<sup>-2</sup>, Table 1) when the same conditions were applied, i.e. at an electrode potential of -90 mV and in the presence of PMS as soluble electron carrier. (2) His-tagged MBH was immobilized on a Ni-NTA-terminated surface in the absence of PS1. The hydrogenase did not show hydrogen evolution under otherwise identical conditions (-90 mV, 75 μM PMS, PS1 buffer) and illumination. (3) The bare gold surface, covered with buffer and PMS, did not produce hydrogen upon illumination and a potential of -90 mV. These experiments (summarized in Table 6) provide unequivocal evidence that the presence of PS1 is critical for the detected activity.

Table 6 Hydrogen evolution rates

Surface structure	Illumination	H <sub>2</sub> production rate / (pmol H <sub>2</sub> s <sup>-1</sup> cm <sup>-2</sup> )
PS1-MBH	Yes	120 ± 30
PS1-MBH	No	< 20
PS1 <sub>ΔPsaE</sub>	Yes	31 ± 12
MBH	Yes	< 20
Bare gold	Yes	< 20

From the hydrogen production rate of the hybrid complex ( $120 \times 10^{-12}$  mol H<sub>2</sub> s<sup>-1</sup> cm<sup>-2</sup>) and the amount of specifically immobilized MBH<sub>PsaE</sub> ( $1.6 \times 10^{-12}$  mol MBH<sub>PsaE</sub> cm<sup>-2</sup>) the surface activity was calculated to be  $4,500 \pm 1,125$  mol H<sub>2</sub> min<sup>-1</sup> mol<sup>-1</sup> hybrid complex (pH 7.5, 20 °C, -90 mV).

#### 4.2.5 Hydrogen evolution potential

The presented experiments were performed at a constant potential of -90 mV to assure fast re-reduction of PMS at the surface. But the system is able to produce molecular hydrogen at a potential of up to 85 mV which is the redox potential of PMS (Figure 43). A photocurrent above noise level was measured up to a potential of 10 mV – with 3% of the amplitude detected at -90 mV (Figure 47).

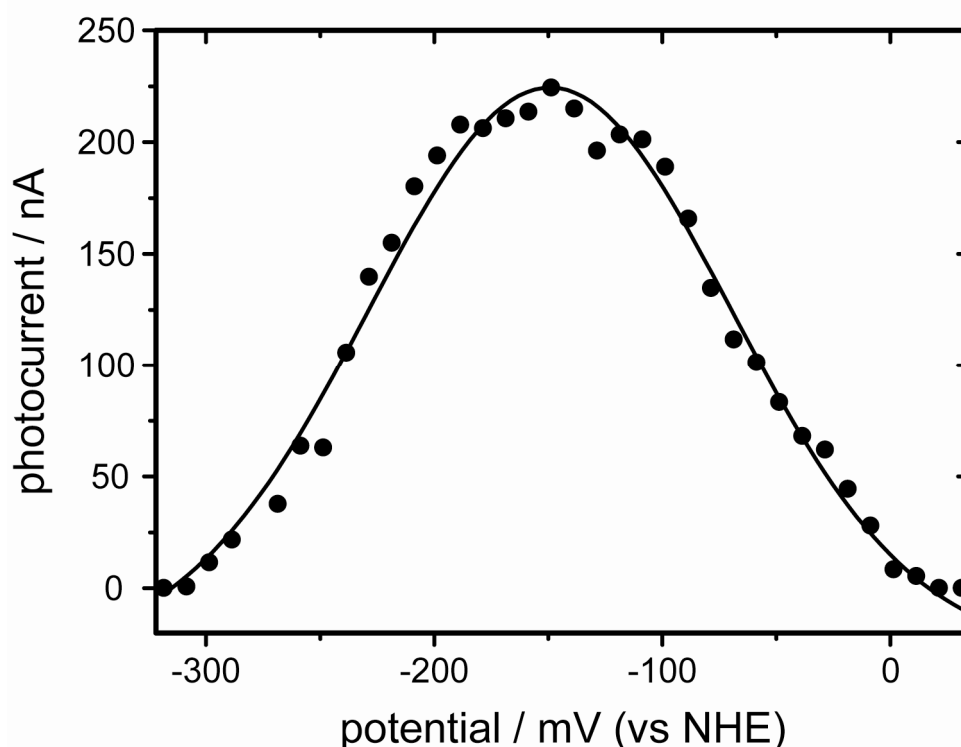


**Figure 47** Potential dependence of the photocurrent of PS1-MBH | A monolayer of PS1-MBH is equilibrated at the respective potential. The photocurrent is measured under red light illumination.

Surprisingly, at potentials below -150 mV a decrease of the photocurrent was observed. Possible explanations are (1) reductive damage of the monolayer. (2) re-orientation of PS1 in the electric field, which blocked the binding site of PMS.

The concentration of reduced PMS is higher at more negative potentials and can not explain the decrease of the photocurrent. In addition, the monolayer was constantly monitored by SEIRAS during the measurement and no potential-induced protein desorption was observed and can be excluded as explanation.

#### 4.2.6 Mimic the native environment

A major difference between the native, cellular system and the *in vitro* device is that in the latter the photosystem I is solubilized by detergent molecules and not embedded in a lipid bilayer. In order to come closer to the native environment, the photosystem I is reconstituted in lipids.

The surface-tethered PS1<sub>ΔPsaE</sub> monolayer was incubated in a solution of dimyristoyl-phosphatidylcholine (DMPC) vesicles, while the concentration of detergent molecules was continuously decreased by the addition of bio-beads. The immobilization of DMPC molecules on the surface was monitored by SEIRAS (Figure 48).

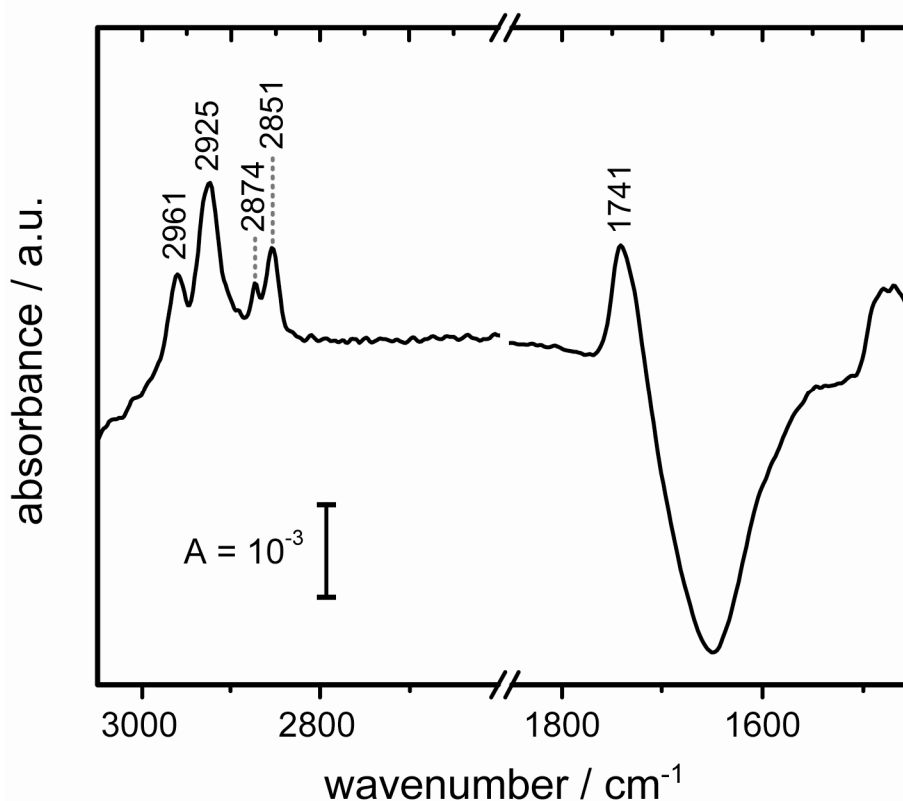


**Figure 48** SEIRA spectrum of the reconstitution process / Di-myristoyl-phosphatidyl-cholin (DMPC) reconstitutes a monolayer of  $PSI_{\Delta Ps a E}$ . The positive bands indicate the presence of DMPC along the surface.

The bands at 2961  $\text{cm}^{-1}$  and 2925  $\text{cm}^{-1}$  are assigned to the symmetrical C-H stretching vibrations of the two alkyl chains of DMPC. The corresponding asymmetrical stretching vibrations result in the bands at 2874  $\text{cm}^{-1}$  and 2851  $\text{cm}^{-1}$ . The band at 1741  $\text{cm}^{-1}$  is due to the C=O stretching mode of the ester head group. These bands indicate the presence of DMPC along the surface. Water was displaced from the surface and a broad negative band at 1650  $\text{cm}^{-1}$  was detected from the water bending mode. No additional spectral features were observed in the amide region (1700-1500  $\text{cm}^{-1}$ ) and, thus, the protein was neither removed from the surface nor its structure or orientation drastically changed. The surface structure is described in detail in chapter 4.3.

After the reconstitution process the fusion protein  $MBH_{PsaE}$  was bound to the surface. The stability of the photocurrent under continuous illumination was compared for the detergent-stabilized and the DMPC-reconstituted monolayer of  $PSI$ -MBH. After 1 hour of continuous illumination a photocurrent of 115 nA was measured for the reconstituted monolayer, while only 55 nA were measured for the detergent-stabilized photosystem I. It took 7 hours of illumination until the photocurrent of the reconstituted monolayer

decreased to the same value (Figure 49). The stability increased by a factor of 7 upon reconstitution.

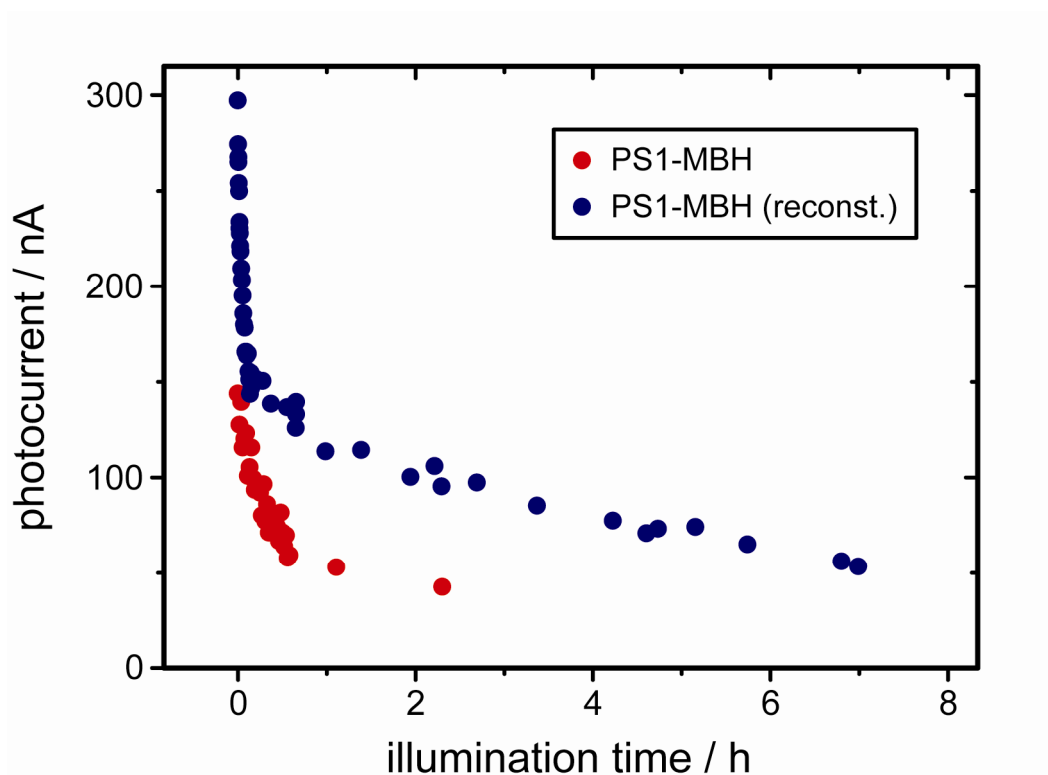


**Figure 49** *Stability of the surface-tethered hybrid complex* | Monolayers of detergent-stabilized PS1-MBH (red) and reconstituted PS1-MBH (blue) are continuously illuminated. The photocurrent is plotted versus the total illumination time. To measure the photocurrent, the light is switched off for 10 seconds and the photocurrent is determined from the respective current drop.

#### 4.2.7 Conclusions

Photosystem I (PS1) was immobilized on a gold surface and specifically assembled with the membrane-bound hydrogenase (MBH). Upon light-illumination the hybrid complex produced molecular hydrogen at a rate of  $4,500 \pm 1,125 \text{ mol H}_2 \text{ min}^{-1} \text{ mol}^{-1}$  (pH 7.5, 20 °C, -90 mV).

For MBH, which was directly immobilized on a pyrolytic graphite edge electrode (without PS1), a turnover rate of  $4,200 \text{ mol H}_2 \text{ min}^{-1} \text{ mol}^{-1}$  was estimated (Goldet et al., 2008). This activity was measured at a potential of -450 mV, pH of 5.5, 40 °C, and under continuous removal of the produced hydrogen by a rotating ring disk electrode. This value is in the same range as that measured for the hybrid complex. In our experiments, the use of light by PS1 made it possible to increase the potential to -90 mV

(to lower energy), increase the pH to 7.5, do it without continuous removal of H<sub>2</sub>, and decrease the temperature to room temperature (20 °C) without decreasing the hydrogen evolution rate. Thus, PS1 increases the electron transfer rate towards MBH significantly. On this basis, our derived value for hydrogen production by the hybrid complex is considered to be high. The results demonstrate highly efficient coupling of photosynthesis and biological hydrogen production.



### **4.3 Spatially-resolved analysis of a protein monolayer**

The study of surface-tethered proteins commonly includes assumptions about the surface structure. Open questions are: How are proteins oriented? Do the proteins aggregate on the surface? How do lipids spread over the surface? Schematic pictures often show idealized, well-ordered, homogenous monolayer structures.

In this chapter, the first steps towards a spatially-resolved infrared analysis of a protein monolayer is shown. In scanning near-field infrared microscopy (SNIM) the sample is probed by an atomic force microscopy (AFM) tip. The tip is illuminated by intense infrared radiation and allows measuring of spatially-resolved spectral information. The investigation of a reconstituted, surface-tethered membrane protein is schematically depicted in Figure 50.

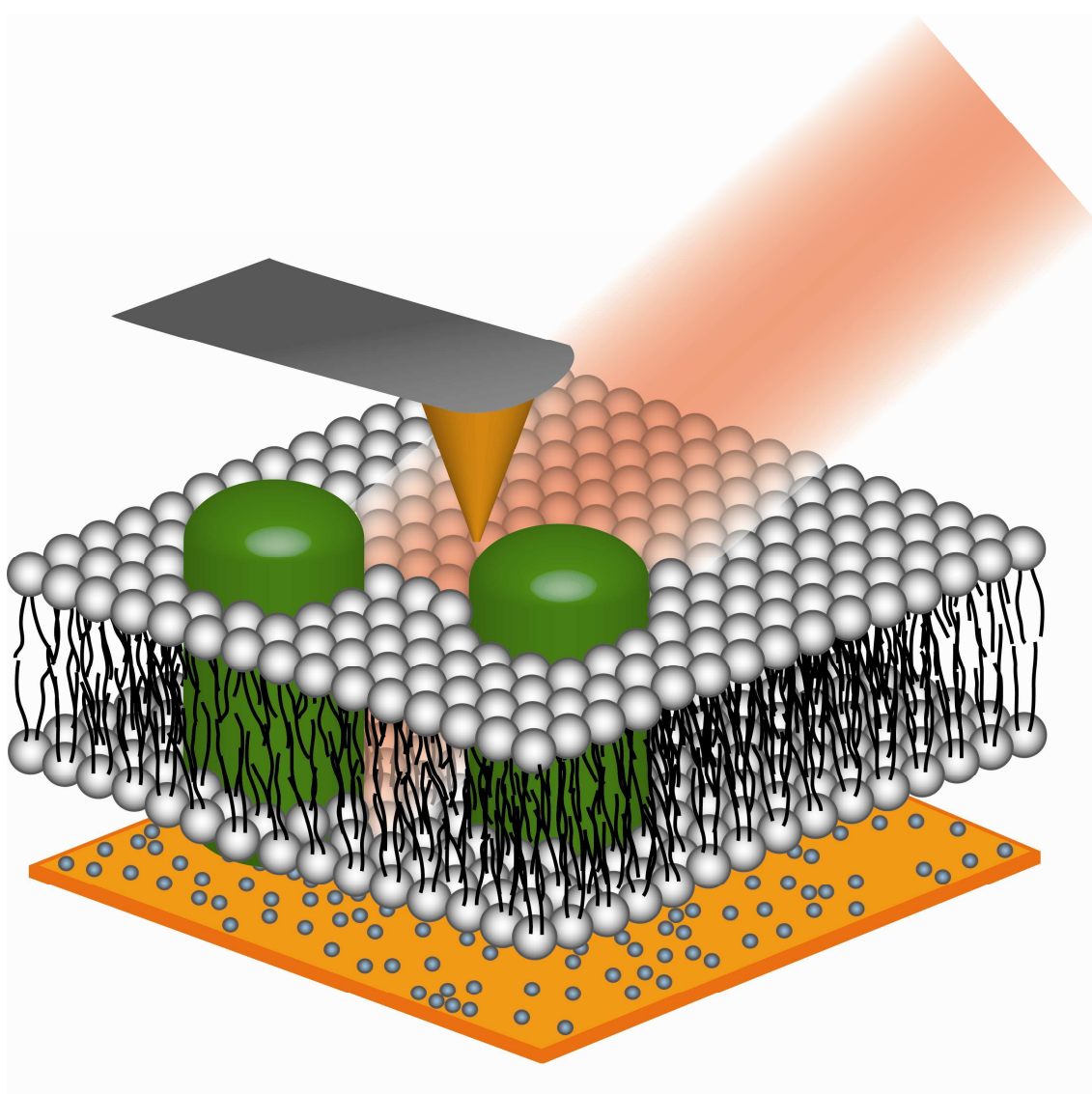


**Figure 50** *Reconstituted membrane protein – investigated by SNIM* | Cytochrome *c* oxidase is immobilized and reconstituted in a lipid bilayer. The topography is measured by AFM and the scanning near-field infrared microscopy setup is used to record vibrational information at each position of the tip.

In the future this technique will be used to investigate the surface-bound hybrid complex of photosystem I and membrane-bound hydrogenase. The recorded data will show how the topographical structure of the photosystem I monolayer is affected by the assembly with the hydrogenase.

#### 4.3.1 Model system “Cytochrome *c* oxidase”

Cytochrome *c* oxidase (CcO) is a well-investigated system in our laboratory. Expression, purification, surface immobilization and reconstitution in a lipid bilayer of di-myristoyl-phosphatidyl-cholin (DMPC) are established.

Template-stripped gold (Chapter 3.9) was modified with a Ni-NTA-terminated monolayer and incubated with a solution of detergent-stabilized CcO. CcO bound to this layer via its His-tag. As long as each CcO molecule was isolated (i.e. without neighbouring molecules) several orientations were possible. It might orient between upstanding position, with the membrane plane parallel to the surface, and sideways position, with the membrane plane perpendicular to the surface. During the binding process, more and more CcO molecules bound to the surface and the upstanding orientation was stabilized by adjacent CcO molecules. Afterwards, the surface-tethered protein monolayer was reconstituted in a lipid bilayer (Chapter 0), and gold nano particles were dried on top of the sample as a contrast standard for the SNIM measurement. The predicted surface structure is depicted in Figure 51.

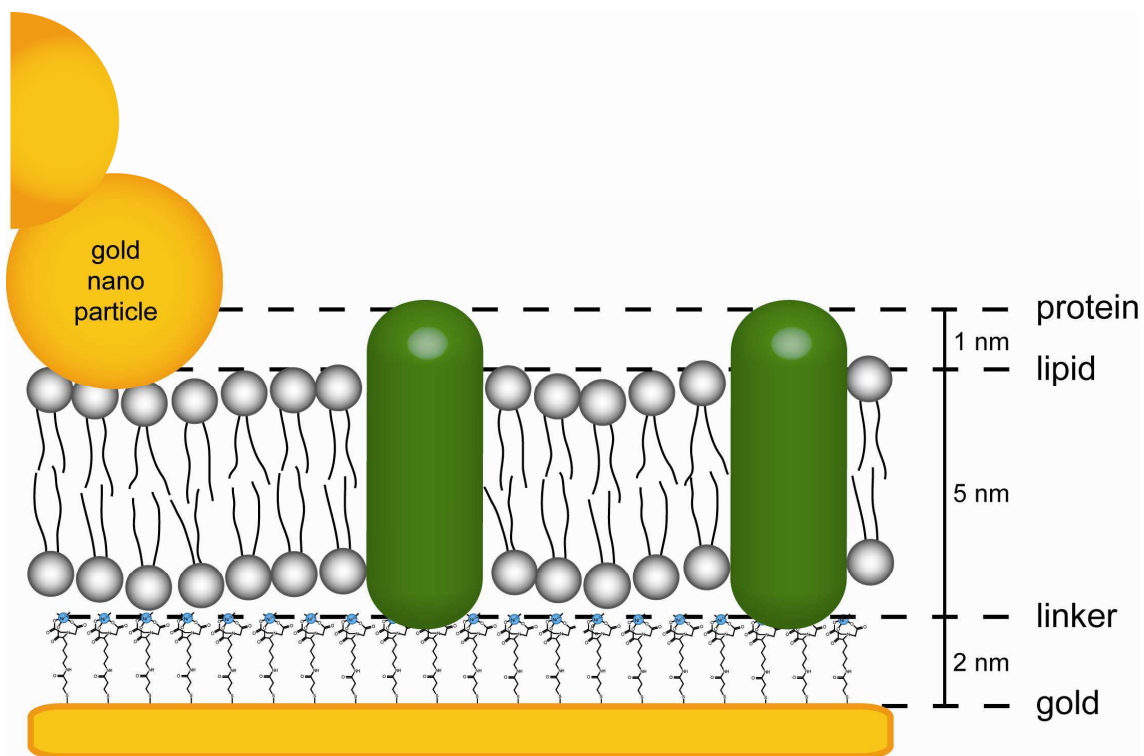


**Figure 51** *Structural model of the CcO layer* | The gold surface is covered with a 2 nm-thick monolayer of Ni-NTA linkers. CcO molecules (green) are bound to this linker. The DMPC bilayer forms at the hydrophobic parts of the CcO. Gold nano particles with a diameter of 4 nm are dried on top of the sample.

### 4.3.2 Topography

AFM was used to record the topography of the sample. An overview scan of 25x25  $\mu\text{m}$  is shown in Figure 52(A). Island like structures, which were 20-200 nm higher than the background, were distributed over the sample. These islands were also observed when gold nano particles were dried on a bare gold surface (data not shown). The gold nano particles aggregated on top of the surface.

A small section was enlarged and the tilt of this section was corrected by subtraction of a fitted plane (Figure 52(B)). The topography was dominated by structures with a height between 5 nm and 10 nm, what is consistent with a protein monolayer or a lipid membrane layer. The island-like structures (green/red), with a height above 20 nm, were gold nano particle aggregates. They were necessary as a contrast reference for the SNIM analysis

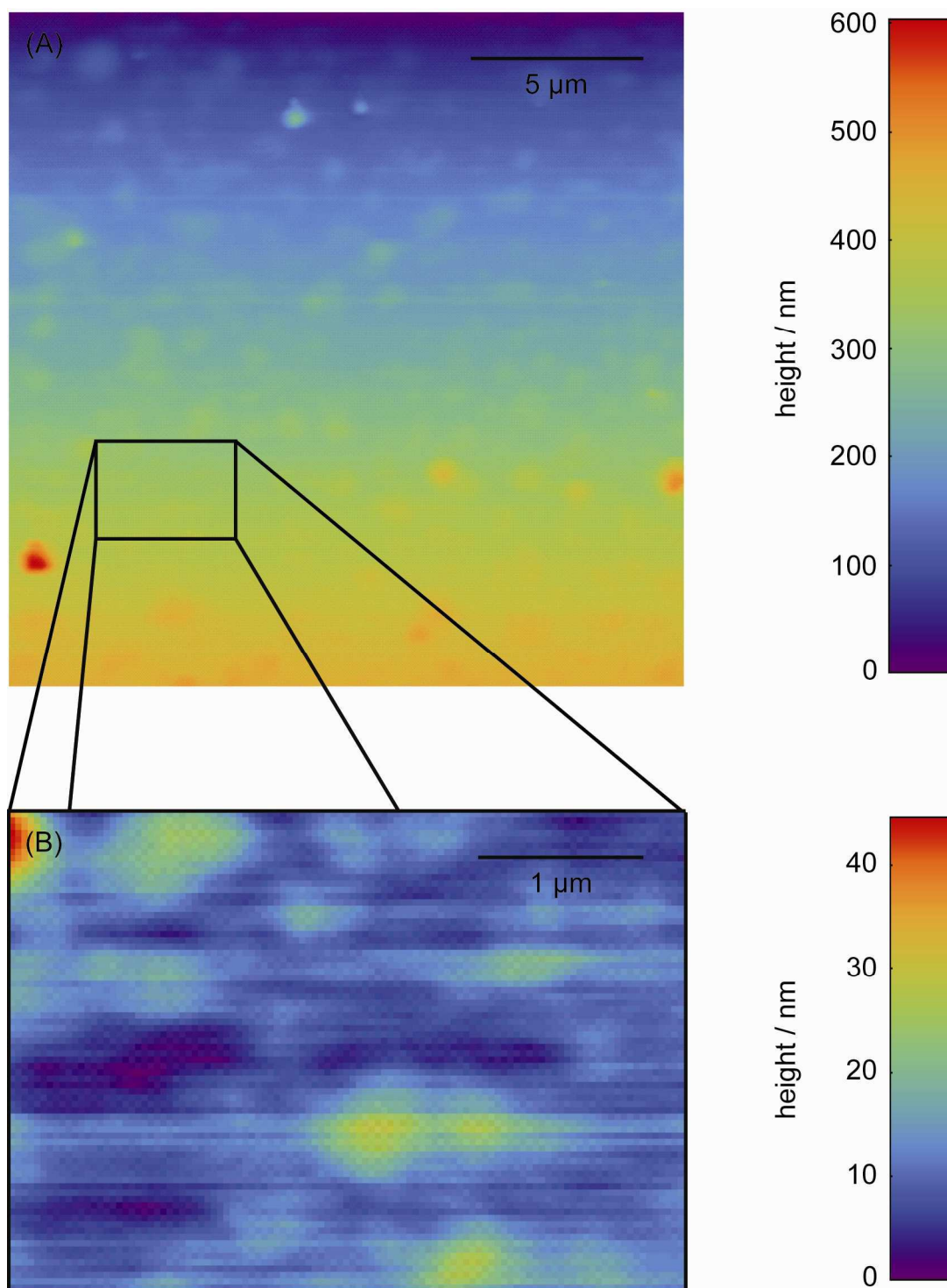


**Figure 52** *AFM image of reconstituted cytochrome c oxidase* | (A) CcO is immobilized on a Ni-NTA-modified gold surface and reconstituted in a lipid bilayer. 5 nm gold particles are dried on the surface as reference for the SNIM measurement. The AFM image (512x512 pixels) shows an area of 20x20 μm. The raw data without any processing are presented here. (B) The indicated area (107x76 pixels) of the AFM image is enlarged. The tilt of the sample is corrected by subtraction of a fitted plane.

### 4.3.3 Near-field imaging

The surface modification steps were monitored by SEIRA spectroscopy (Figure 53). During CcO binding (red curve) the amide I band rose at  $1657\text{ cm}^{-1}$ . For the reconstitution in DMPC (black curve) a characteristic band was observed at  $1740\text{ cm}^{-1}$  which is assigned to the carbonyl stretching mode of the ester head group (Ataka et al., 2004).

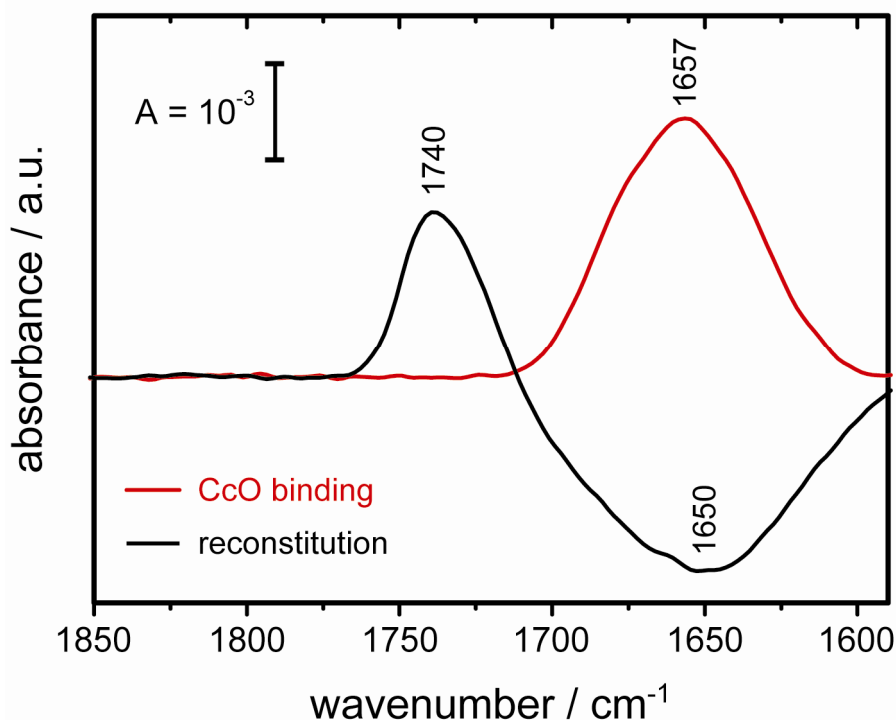


**Figure 53 SEIRA spectra of CcO binding and DMPC reconstitution** | Detergent-solubilized CcO is immobilized on a Ni-NTA-modified template-stripped gold surface. The spectrum (red) is recorded at maximum binding after washing with buffer. The surface-tethered protein layer is incubated with a solution of detergent-destabilized lipid vesicles (liposomes) of DMPC. The spectrum (black) is measured after the reconstitution is completed. The spectral region is cut to the used range for the SNIM measurement. The bands are discussed in the text.

In SEIRAS, the signals are averaged over the entire surface. Strictly speaking, these spectra only prove that CcO and DMPC accumulate in the vicinity of the surface. But the spectra provide the information at which wavenumbers the different compounds absorb. The broad, negative band at  $1650\text{ cm}^{-1}$  is not a spectral feature of the lipid, but results from the displacement of water from the surface. The lipid does not absorb in this region.

For the SNIM measurement, intense laser lines close to the peak maxima were used to measure at wavenumbers where the compounds absorb –  $1647\text{ cm}^{-1}$  for the protein and  $1744\text{ cm}^{-1}$  for the lipid. SNIM images at these wavenumbers were recorded in the same region as the AFM overview scan. The wavenumber  $1801\text{ cm}^{-1}$  was used as a reference, where neither protein nor lipid absorbs (Figure 54).

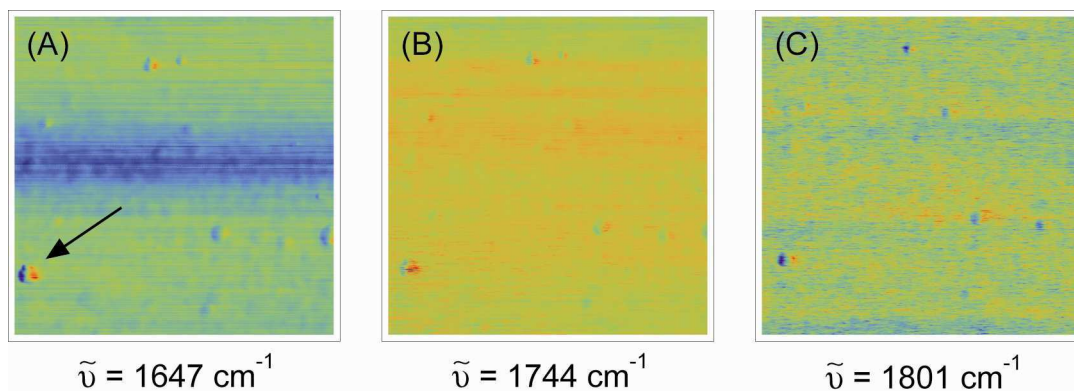


**Figure 54** SNIM images of reconstituted cytochrome c oxidase | The reconstituted CcO-layer is investigated by SNIM at three wavenumbers: (A)  $1647\text{ cm}^{-1}$ , (B)  $1744\text{ cm}^{-1}$ , and (C)  $1801\text{ cm}^{-1}$ . The unprocessed data are presented here. The marked position in (A) is discussed in the text.

Round areas of strong near-field contrast were observed at several positions at each wavelength. One such spot is marked with an arrow in Figure 54(A). These areas were correlated with the position of gold nano particle aggregate on the AFM scan, which was simultaneously recorded. The large height difference resulted in a topography artifact at the edges of the gold nano particle aggregates. The near-field contrast was high for the right edge of these positions and low for the left edge. This distribution was due to the moving direction of the sample from the left to the right with respect to the AFM tip. The height adaptation was fast on the right edge, when the gold nano particle aggregate approached the tip. This resulted in a high near-field contrast. On the other edge the height adaptation was comparably slow and a low near-field contrast was observed. The rest of the area was quite noisy. The spatially-resolved spectral information was not directly accessible as an image.

The intensity of the near-field signal and the signal-to-noise ratio varied with the intensity of the respective laser line and with the focusing of the laser beam on the AFM tip. In order to correct the fluctuation between the measurements at different wavenumbers, the near-field intensity  $I_{\text{Sample}}$  at each point was correlated to the near-field intensity of gold  $I_{\text{Gold}}$  in the same measurement.  $I_{\text{Gold}}$  was averaged over all points which were assigned to gold nano particle aggregates from the topography. The normalized near-field contrast  $c$  was calculated according to the equation (5).

$$C = \frac{I_{Sample} - I_{Gold}}{I_{Gold}} \quad (5)$$

For each position of the scan the near-field contrast was plotted versus the corresponding height and a scatter plot for the three wavenumbers was obtained (Figure 55). The data points in the protein (A) and lipid (B) measurement were more concentrated. This indicates that protein and lipid can be detected in the near-field. A measurement at  $1801 \text{ cm}^{-1}$ , where neither protein nor lipid absorbs, showed a broader, less specific distribution.

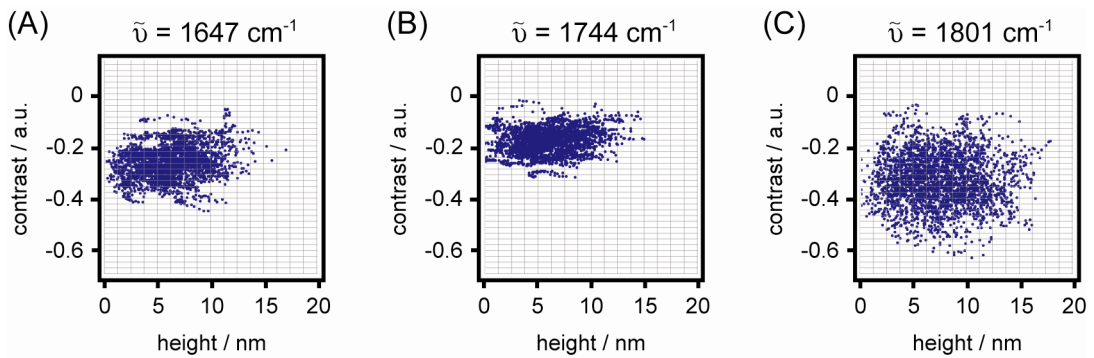


**Figure 55** *Near-field scatter plots* | The near-field contrast is plotted versus the height. Each point in the scatter plot corresponds to one pixel of the scan. (The scatter plots were designed by Fouad Ballout (RU Bochum, group of Prof. Havenith))

For better analysis, a grid was placed on top of the scatter plot, and the data points in each cell were counted. The probability distribution of the near-field contrast at the respective height was plotted as a contour plot for each wavenumber (Figure 56).



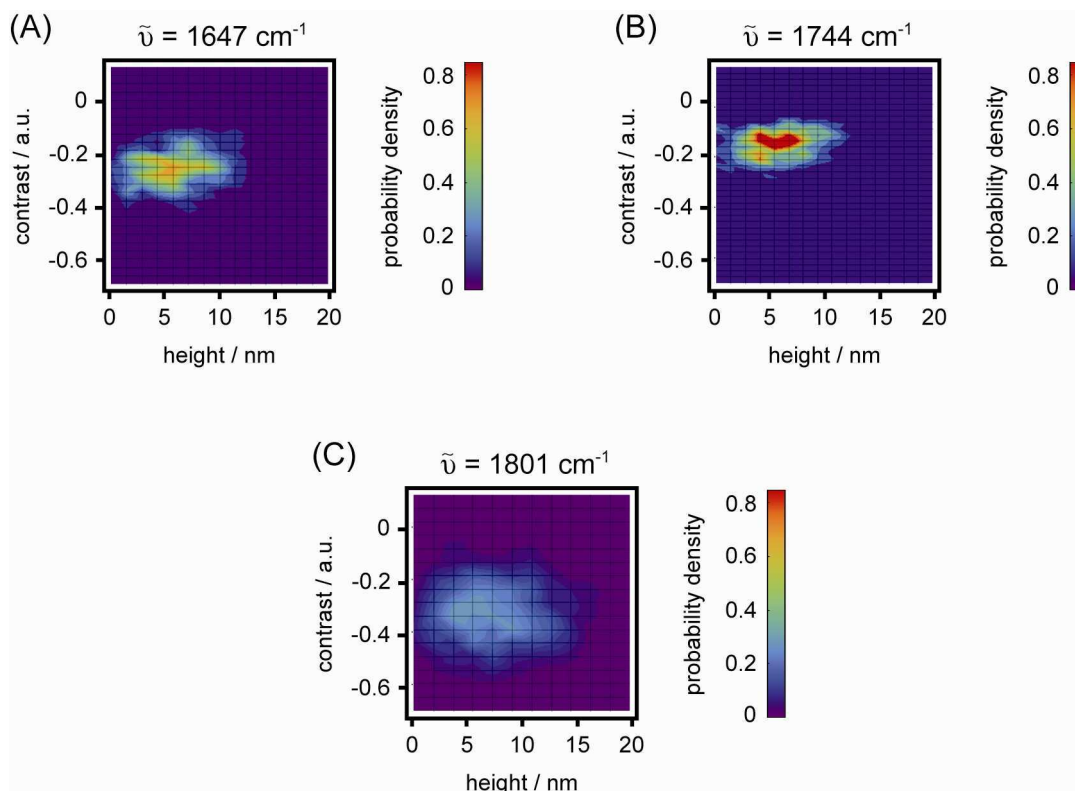


**Figure 56** *Near-field contour plots* | The probability distribution of near-field contrast at respective heights is plotted as a 3-dimensional probability density. The third dimension is colour-coded. (A) at  $1647 \text{ cm}^{-1}$ , (B) at  $1744 \text{ cm}^{-1}$ , and (C) at  $1801 \text{ cm}^{-1}$ . (The contour plots were calculated by Fouad Ballout (RU Bochum, group of Prof. Havenith))

The lowest point of the scan is set to 0 nm and all other height values refer to this point. If the gold surface was completely covered with the Ni-NTA terminated monolayer the top of this layer was set to 0 nm. According to the suggested model (Figure 51) a lipid membrane was expected at a height of 5 nm (or 7 nm, if gold is the zero level) and a CcO monolayer was expected at a height of 6 nm or 8 nm, respectively. In addition, the surface had differences in height of at most 1.5 nm (Figure 14(B)) due to the used template-stripped gold substrate. The lowest position was the height reference, but the various surface structures could also be immobilized at the higher positions. Thus, the surface structures can be detected at the predicted height and at positions which were up to 1.5 nm higher.

The contour plot at  $1801 \text{ cm}^{-1}$  showed a broad, diffuse distribution without significant spectral information. For the protein measurement (A) the highest probability density was detected at a contrast of -0.25 and a height of 5-6 nm. This was consistent with the height of the CcO with respect to the Ni-NTA monolayer. The data were concentrated in a contrast interval of 0.1. The tip of the AFM had a curvature radius of 40 nm. Due to

the shape of the electric field between tip and gold surface a spot with a radius of approximately 80 nm was probed at a time. The concentration of the protein varied from spot to spot and resulted in a broadened contrast interval.

The same was true for the lipid measurement (B), where the highest probability density was detected in an interval between -0.10 and -0.16. The highest probability density was found for topographies with a height between 3.5 and 8 nm. 5-6.5 nm was consistent with the predicted lipid bilayer. Lower structures might consist of a lipid monolayer or “randomly” accumulated lipids. Higher structures might be formed by lipids which were unspecifically bound to proteins or the lipid membrane. These results are schematically summarized in Figure 57.

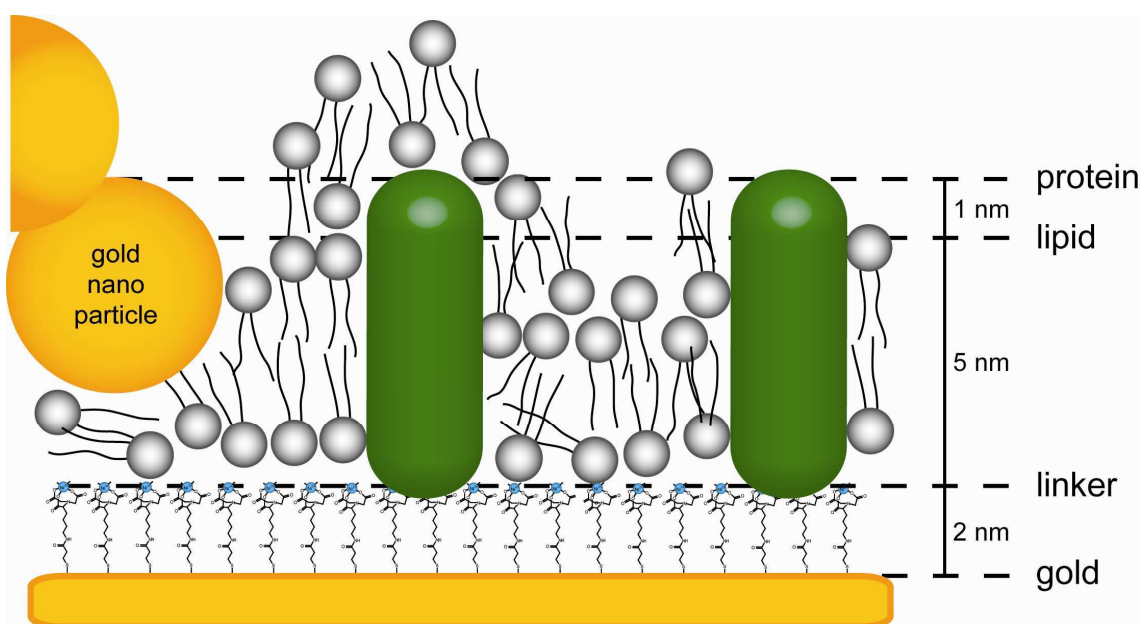


**Figure 57 Improved model of the CcO layer** | The gold surface is covered with a 2 nm thick Ni-NTA-terminated monolayer. CcO is adsorbed on this layer via its His-tag. Lipids are spread over the surface and cover the transmembrane region of the CcO. Gold nano particles are dried on top.

#### 4.3.4 Conclusions

It was possible to correlate near-field information with topographic heights. An improved model of a reconstituted monolayer of cytochrome c oxidase could be derived from these data (Figure 57): The gold surface is covered by a continuous, Ni-NTA-terminated monolayer. CcO is immobilized on this layer in an upstanding position, with the membrane plane parallel to the surface. The surface-tethered proteins are reconstituted in a non-perfect lipid membrane.

The aim for the future is to assign every single pixel of the AFM image to one of the predicted surface structures. This information will yield a chemical image of the surface.

#### 4.4 Structural investigation of the H-cluster

The structure of the H-cluster is known from X-ray crystallography of the [FeFe]-hydrogenases from *Clostridium pasteurianum* (Peters et al., 1998) and *Desulfovibrio desulfuricans* (Nicolet et al., 1999). Detailed information about the inorganic ligands was provided by infrared spectroscopy (Pierik et al., 1998; Nicolet et al., 2001), as well as by ENDOR spectroscopy (Thomann et al., 1991). The structure of the H-cluster is summarized in the introduction (Chapter 2.2.2).

In this study, the [FeFe]-hydrogenase *CrHydA1* from *Chlamydomonas reinhardtii* was investigated by IR spectroscopy. The aim is to monitor changes in the ligand arrangement during hydrogen production (Chapter 4.4.2).

##### 4.4.1 Marker bands of the H-cluster

It has not been shown that the structure of the metal center of *CrHydA1* is identical to the H-cluster which has been found in the crystal structure of other hydrogenases. Initial EPR studies detected an axial signal of the CO-inhibited form which is characteristic for [FeFe]-hydrogenases (Kamp et al., 2008).

Here, the IR spectra of H<sub>2</sub>-reduced and CO-inhibited *CrHydA1* are compared with literature values of other [FeFe]-hydrogenases to confirm the structural similarity.

##### *Transmission measurements*

Several bands are observed in the spectral region between 2150 cm<sup>-1</sup> and 1750 cm<sup>-1</sup> (Figure 58). These bands are assigned to stretching vibrations of inorganic CO and CN<sup>-</sup> ligands which are bound to the central irons of the metal center. The bands are assigned, according to earlier infrared spectroscopic studies of hydrogenases (Pierik et al., 1998; Nicolet et al., 2001). Bands at wavenumbers between 2100 cm<sup>-1</sup> and 2040 cm<sup>-1</sup> correspond to the stretching vibration of terminal CN<sup>-</sup> ligands. Bands at lower wavenumbers are due to the stretching vibration of CO ligands.

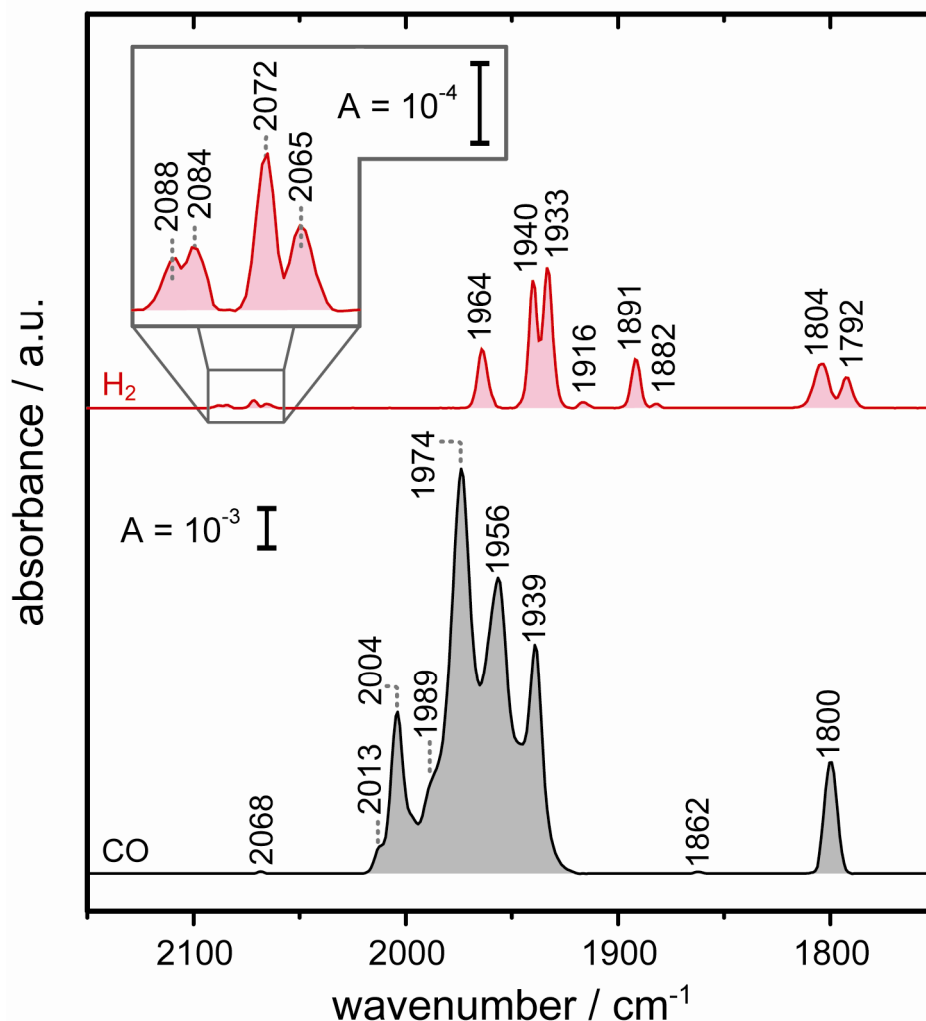


**Figure 58** Infrared absorption spectra of different *CrHydA1* states | 1 mM *CrHydA1* is incubated with hydrogen (red), or carbon monoxide (black) and measured in a transmission setup by IR spectroscopy. The bands are discussed in detail in the text.  $8 \times 1024$  scans are averaged for each spectrum.

Defined states of the [FeFe]-hydrogenase from *Desulfovibrio vulgaris* were investigated in the past (Pierik et al., 1998). For the  $H_2$ -reduced state CN stretching vibrations were observed at  $2079\text{ cm}^{-1}$  and  $2041\text{ cm}^{-1}$ . CO stretching vibrations were measured at  $1965\text{ cm}^{-1}$ ,  $1941\text{ cm}^{-1}$ ,  $1916\text{ cm}^{-1}$ , and  $1894\text{ cm}^{-1}$ . The  $2041\text{ cm}^{-1}$  band was found to disappear under argon atmosphere, while a second band in the CN region appeared at  $2095\text{ cm}^{-1}$ . Similar bands were found for *CrHydA1* with a shift of up to  $7\text{ cm}^{-1}$  (Figure 58, red curve) indicating that the  $H_2$ -reduced state of a very similar H-cluster contributed to the spectrum. The presence of four bands in the CN region (compared to two in the literature) showed that at least one additional state was detected.

No bands were observed below  $1894\text{ cm}^{-1}$  for the  $\text{H}_2$ -reduced state in the literature. Here, the bands at  $1804\text{ cm}^{-1}$  and  $1792\text{ cm}^{-1}$  were assigned to a bridging CO molecule between both iron ions. The band at  $1882\text{ cm}^{-1}$  was assigned to an intermediate state between bridging and terminal CO. The existence of a bridging CO and the observation of an additional band at  $1933\text{ cm}^{-1}$  in my measurements affirmed that different states of *CrHydA1* contributed to the spectrum. Probably a partially reduced state was observed in addition to the fully reduced state.

After incubation in CO two prominent bands were observed at  $2016\text{ cm}^{-1}$  and  $1971\text{ cm}^{-1}$  for the *Desulfovibrio vulgaris* enzyme (Pierik et al., 1998). The binding of CO to a  $\text{Fe}(\text{CO})(\text{CN}^-)$  center resulted in a iron ion with two bound CO molecules. The CO molecules showed a strong vibrational coupling and were assigned to these bands. For *CrHydA1* these bands were found at  $2004\text{ cm}^{-1}$  and  $1974\text{ cm}^{-1}$  in my measurements. The band at  $1862\text{ cm}^{-1}$  was assigned to an intermediate state between bridging and terminal CO. Intermediate states at similar low wavenumbers are known from literature ( $1848\text{ cm}^{-1}$ , Cotton and Wilkinson, 1988). Additional bands were observed in the spectrum of the CO-inhibited *CrHydA1* (Figure 58, black curve). These bands indicated that other states contributed to the spectrum. A very similar spectrum was observed earlier for *Desulfovibrio vulgaris* (van der Spek et al., 1996).

The spectral information is summarized in Table 7. The detected bands and the spectral changes between  $\text{H}_2$ -reduced and CO-inhibited state strongly indicate that the H-cluster of *CrHydA1* is identical to the one of other [FeFe]-hydrogenases.

Table 7 IR frequencies of *CrHydA1* in the CO/CN region

<i>CrHydA1</i> state	Band position / $\text{cm}^{-1}$	Assigned vibration
$\text{H}_2$ / Ar	2088, 2084, 2072, 2065	CN stretching of $\text{Fe}(\text{CO})(\text{CN}^-)$
	1964, 1940, 1933, 1916, 1891	CO stretching of $\text{Fe}(\text{CO})(\text{CN}^-)$
	1882	Stretching of terminal/bridging CO
	1804, 1792	Stretching of bridging CO
CO / Ar	2068	CN stretching of $\text{Fe}(\text{CO})(\text{CN}^-)$
	2013, 2004, 1989, 1974	CO stretching of $\text{Fe}(\text{CO})_2(\text{CN}^-)$
	1956, 1939	CO stretching of $\text{Fe}(\text{CO})(\text{CN}^-)$
	1862	Stretching of terminal/bridging CO
	1800	Stretching of bridging CO

#### *Attenuated total reflection measurements*

The protein solution on top of the silicon prism was probed by the evanescent IR wave. As the penetration depth does not change, the signal intensity solely depended on the concentration of the protein. The advantage of the attenuated total reflection (ATR)

setup compared to the transmission setup was that the sample was accessible for manipulation during the whole measurement. The protein bands were monitored *in situ* during the drying process (Figure 59).

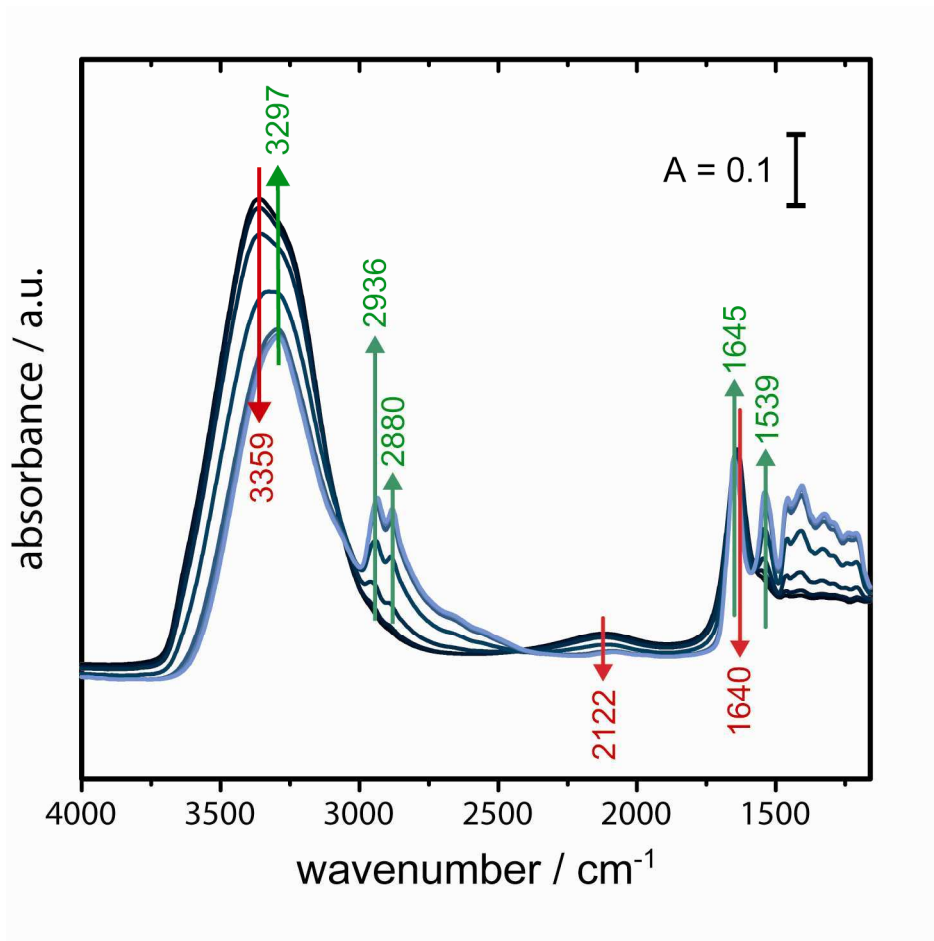


**Figure 59** Infrared ATR spectra of CrHydA1 during drying | 50  $\mu\text{L}$  of 1 mM CrHydA1 solution (in 10 mM potassium phosphate buffer) is placed on a silicon ATR crystal. The solution is slowly dried in an argon stream. The spectra are recorded during the drying process at  $t = 1$  (black), 6, 12, 15, 18, 21, and 24 (light blue) minutes. 1024 scans are averaged for each spectrum. Rising and decreasing bands are marked in the figure.

While the protein solution was dried in an argon stream, water was removed from the sample. Hence, the bands which were assigned to vibrational modes of water decreased (red arrows). The protein was concentrated and the bands which corresponded to vibrational modes of the protein increased (green arrow). Amide A ( $3297\text{ cm}^{-1}$ ), amide I ( $1645\text{ cm}^{-1}$ ), and amide II ( $1539\text{ cm}^{-1}$ ) bands were due to vibrations of the protein backbone. The bands at  $2936\text{ cm}^{-1}$  and  $2880\text{ cm}^{-1}$  were assigned to asymmetrical and symmetrical C-H stretching of various amino acid side chains. Various amino acid side

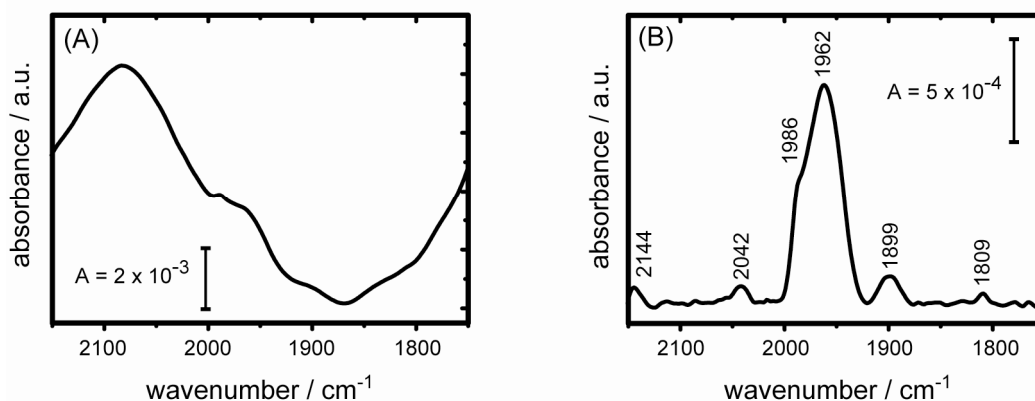
chain vibrations arose at wavenumbers below  $1460\text{ cm}^{-1}$ . The spectral information and assigned vibrational modes are listed in Table 8.

Table 8 IR frequencies of a CrHydA1 solution during drying

Band position / $\text{cm}^{-1}$	Assigned vibration
3359(-)	Asymmetrical and symmetrical $\text{H}_2\text{O}$ stretching
3297(+)	N-H stretching (amide A)
2936(+)	Asymmetrical C-H stretching (in $\text{CH}_2/\text{CH}_3$ )
2880(+)	Symmetrical C-H stretching (in $\text{CH}_2/\text{CH}_3$ )
2122(-)	$\text{H}_2\text{O}$ libration
1645(+)	C=O stretching (amide I)
1640(-)	$\text{H}_2\text{O}$ bending
1539(+)	C=N stretching / N-H bending (amide II)
<1460(+)	Various amino acid side chain vibrations

Two major bands were observed within the CO/CN region (Figure 60). These bands were detected at  $1986\text{ cm}^{-1}$  and  $1962\text{ cm}^{-1}$  and assigned to the CO stretching of terminal CO ligands. The CrHydA1 sample had been incubated in hydrogen prior to the measurement and was kept under argon atmosphere during the whole measurement. Thus, the iron centers should both carry one terminal  $\text{CN}^-$ , one terminal CO and one bridging CO. The band at  $1986\text{ cm}^{-1}$  was found at a too high wavenumber for such an iron center and indicated that two terminal CO ligands were found on at least one of the iron centers (Pierik et al., 1998).

The band at  $2042\text{ cm}^{-1}$  was assigned to the stretching vibration of a terminal  $\text{CN}^-$  ligand. But the band appeared at a lower wavenumber compared to the measurements in the transmission setup. This shift might originate from an altered metal center induced by the drying process. Two factors might contribute to this change: (1) The concentration of the protein was drastically increased and the close contact between protein molecules affected their secondary structure and the environment of the H-cluster. (2) The buffer concentration increased as well and might affect the protein. In both cases the ligand arrangement could be changed. Therefore, the spectra from the transmission setup are used as reference for CrHydA1.



**Figure 60** Infrared ATR spectra of the CO/CN region of CrHydA1 | 1 mM CrHydA1 is further concentrated on a silicon ATR crystal. The spectrum of the CO/CN region between  $2150\text{ cm}^{-1}$  and  $1750\text{ cm}^{-1}$  is recorded after 107 minutes. The unprocessed spectrum (A) and the spectrum after baseline correction (B) are presented.  $8 \times 1024$  scans are averaged for the spectrum.

#### 4.4.2 Structural changes during hydrogen production

A gold surface was modified with a monolayer of 3-mercaptopropionic acid. The immobilization of CrHydA1 on this surface was monitored *in situ* by SEIRAS (Figure 61(A)). The bands which were observed at  $1657\text{ cm}^{-1}$  and  $1553\text{ cm}^{-1}$  were assigned to the amide I and amide II modes, respectively. The negative peak at  $1716\text{ cm}^{-1}$  was assigned to the H-O-H bending mode of water which was displaced from the surface. The negative peak seems to be shifted to higher wavenumber due to the overlap with the amide I band.

The position of amide I and amide II band were shifted compared to the ATR measurement. Due to the surface selection rules, the contributions of the various secondary structure elements to the amide bands depend on their respective orientation to the surface. For example the C=O stretching vibration of the peptide bond is oriented parallel to  $\alpha$ -helices. If an  $\alpha$ -helix is oriented perpendicular to the surface the contribution of the respective C=O stretching mode becomes stronger and the amide I band is shifted to higher wavenumber (Krimm and Bandekar, 1986; Byler and Susi, 1986). Another explanation is that the ATR spectrum is probably disturbed by high concentrations of protein and buffer.

In the SEIRAS measurements, bands in the CO/CN region could not be clearly assigned due to the limiting signal-to-noise ratio (Figure 61(B)). At  $1830\text{ cm}^{-1}$  a positive band might exist, but it can not be clearly distinguished from a shift of the baseline.



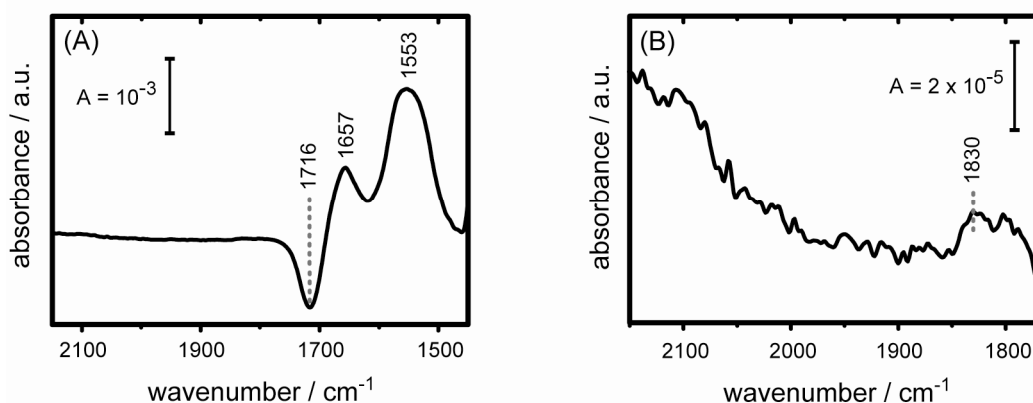


**Figure 61** SEIRA spectra of immobilized CrHydA1 | CrHydA1 is immobilized on an MPA monolayer. The spectrum is recorded during binding of the CrHydA1 monolayer. The overview spectrum (A) and the cut-out of the CO/CN region (B) are presented. 6x 1570 scans are averaged for the spectrum.

One factor reducing the signal intensity was that no pure state of CrHydA1 was immobilized on the surface. During the IR measurements in transmission setup (Chapter 4.4.1) different states contributed to the spectrum under comparable sample treatment (Figure 58, red curve). Potential-induced surface-enhanced infrared difference absorption spectroscopy (SEIDAS) was applied in order to monitor structural changes of the ligand arrangement between two defined states. The monolayer was equilibrated at an external potential of 160 mV, CrHydA1 was forced in its oxidized state, and a reference spectrum was recorded. Then, the potential was changed to -450 mV and the sample spectrum was recorded (Figure 62, red curve). The SEIRA spectrum of the CO/CN region during the binding process was baseline corrected and plotted for comparison (Figure 62, black curve)

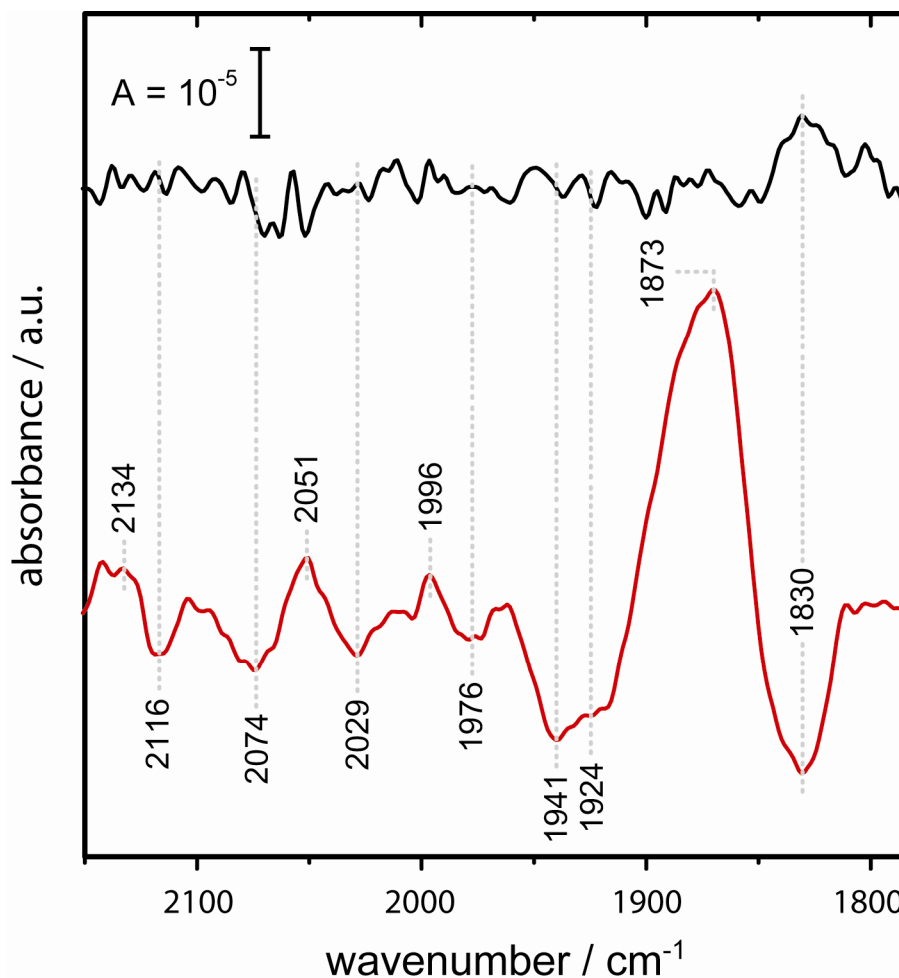


**Figure 62** *Potential-induced SEIDA spectrum of immobilized CrHydA1* | CrHydA1 is immobilized on an MPA monolayer. The reference spectrum is recorded at a potential of 160 mV. The sample spectrum is recorded at -450 mV (red curve). Negative bands are assigned to the oxidized state, positive bands to the reduced state. 27x 1570 scans are averaged for the spectrum. For comparison the absorption spectrum during binding of CrHydA1 is baseline corrected and plotted (black curve).

Methylviologen (MV) was used in this experiment as soluble electron carrier. At a potential of 160 mV MV and CrHydA1 were in their oxidized states. When the potential was changed to -450 mV MV was reduced and transferred electrons to the hydrogenase (Chapter 4.1). The redox reaction of MV did not contribute to spectral changes in the CO/CN region. Negative bands could correspond to vibrational modes of the oxidized form of CrHydA1 and the positive bands could be contributions from the catalytic active form. The band at 1830  $\text{cm}^{-1}$  could be assigned to the stretching vibration of the bridging CO, which disappeared upon reduction. The CO changed to a transition state between bridging CO and terminal CO and gave rise to a band at 1873  $\text{cm}^{-1}$ . A similar difference was also observed for the hydrogenases from

*Desulfovibrio desulfuricans* (Nicolet et al., 2001) and *Desulfovibrio vulgaris* (Pierik et al., 1998) as a difference between oxidized and H<sub>2</sub>-reduced state.

But the observed band intensities are inconsistent if both spectra are compared. A positive band at 1830 cm<sup>-1</sup> was observed in the absorption spectrum during binding (Figure 62, black curve) with about half the intensity of the negative band in the potential-induced difference spectrum (Figure 62, red curve). The other bands of the oxidized form should have a counter part with a similar intensity ratio, but no bands were observed. It is possible that the change of the applied electric field resulted in a reorientation of the hydrogenase molecules and the intensity of the bands were changed due to the surface selection rules (vibrations which change the dipole moment perpendicular to the surface are enhanced stronger). But it is not possible to explain the absence of the six bands (2116, 2074, 2029, 1976, 1941, and 1924 cm<sup>-1</sup>) by surface selection rules. It seems likely that artifacts are found in the SEIDA spectrum. More experiments are necessary to distinguish “true” bands from these artifacts.

#### 4.4.3 Conclusions

The active site of *CrHydA1* contains a metal cluster which has a very similar structure compared to other [FeFe]-hydrogenases. The bands of the CO-inhibited and H<sub>2</sub>-reduced state of the *Desulfovibrio vulgaris* hydrogenases could be assigned to the respective spectra of the *Chlamyomonas reinhardtii* enzyme *CrHydA1*. The band position only varied up to 15 cm<sup>-1</sup> due to differences in the protein cage.

*CrHydA1* was immobilized on a gold surface and the changes between oxidized and catalytic active state were recorded by SEIDA spectroscopy. The spectral data are not contradictory to the transition of the bridging CO to the proximal iron, but further experiments are necessary to confirm this process. The H<sub>2</sub> formation could take place at the vacant coordination site of the distal iron as predicted in literature (Nicolet et al., 2001).

## 5 Concluding discussion

### 5.1 Hydrogenase as electrocatalyst

In the context of the climate problem it has become evident that we have to reduce the carbon dioxide emission. Renewable energy sources, like wind, water, or solar energy, are able to provide energy without any CO<sub>2</sub> emission. At the moment the contribution of renewables to Germany's energy production is about 10% (BMW<sub>i</sub>, 2008). But with further shortage of fossil fuels their fraction will increase. Renewables will have to provide electrical energy as well as fuels, because the world's need for energy is basically a need for fuels.

Hydrogen is a very promising fuel. It can be burned without any CO<sub>2</sub> emission and with water as the only product. One way to convert electrical energy to hydrogen is the electrolysis of (acidified) water. Platinum is broadly used as catalyst for this reaction. The low overpotential of platinum allows hydrogen production at low energy compared to other metallic electrocatalysts. Because the available amount of platinum is limited, it is mandatory to find alternatives.

Nature has developed hydrogenases which are highly efficient catalysts for the reduction of protons to molecular hydrogen. For the [FeFe]-hydrogenase *CrHydA1*, hydrogen production rates of up to 85 mol H<sub>2</sub> min<sup>-1</sup> mol<sup>-1</sup> were measured in this work (Chapter 4.1). With this device, hydrogen is produced at potentials below -290 mV (vs NHE). This value is close to the hydrogen evolution potential of platinum electrodes of -270 mV. Higher hydrogen production rates and a higher hydrogen evolution potential (i.e. hydrogen production at lower energy) have been reported in the literature for pyrolytic graphite edge electrodes (Goldet et al., 2008) and carbon felt electrodes (Hambourger et al., 2008).

However, the application of these systems to large-scale hydrogen production is uneconomic. The expression and purification of the enzyme are too expensive compared to the produced amount of hydrogen. Moreover, these enzymes are highly sensitive to oxygen and only stable for a couple of hours. Both, activity of the enzyme and stability, have to be drastically improved to allow an application in the future. Only a profound understanding of the catalytic mechanism on the atomic scale will lead to the improvement of the efficiency of these biological nanomachines.

In this respect, the catalytically active hydrogenase, that I have studied, is accessible to IR spectroscopy. A time-resolved measurement of the catalytic cycle will help to reveal the reaction mechanism. In this work, the basis for time-resolved measurements was established. Catalytically active *CrHydA1* was immobilized on a gold electrode and the electrons were transferred to the hydrogenase in the absence of a soluble electron carrier (Chapter 4.1.4), which would limit the time resolution due to diffusion. Once we understand the reaction mechanism in detail, we will be able to understand the oxygen tolerance of [NiFe]-hydrogenases and the high activity of [FeFe]-hydrogenases. These are the key information to design an oxygen-tolerant, highly active hydrogenase.

## 5.2 Coupling of photosynthesis and hydrogen production

Our sun is the largest energy source and will be available virtually forever. Solar energy is most efficiently used by photosynthesis to convert abundant, energy-poor molecules into energy-rich molecules. In this way, photosynthesis lays the foundation for life on our planet. The utilization of this energy conversion process has the potential to ensure the world's energy supply forever.

The world's need for energy is basically a need for fuels rather than electrical energy. Thus it is important, to use solar energy for the production of a fuel (e.g. hydrogen), which can be burned without creating severe environmental problems. A coupling between hydrogen producing enzyme and the photosynthesis apparatus can do this job.

In this work, I presented the coupling between photosystem I (PS1) and a hydrogenase via the PS1-subunit *PsaE*. Immobilized on an electrode, this hybrid complex was able to produce molecular hydrogen at a rate of  $4,500 \text{ mol H}_2 \text{ min}^{-1} \text{ mol}^{-1}$  (Chapter 4.2). The turnover rate of this system is superior compared to other (bio-)nanoelectronic devices for hydrogen production, which only use a hydrogenase and do not include PS1. In addition, hydrogen production is possible at positive potentials up to +85 mV, which means that less electrical energy has to be used than is stored in the produced hydrogen. The improvement compared to the hydrogen evolution potential of commercially applied platinum electrodes of -270 mV is considered to be large.

However, the device shares the disadvantages of all enzyme-modified electrodes, i.e. it is hardly possible to repair or specifically replace inactive proteins. Thus, the activity of the surface continuously decreases and all proteins must be desorbed and replaced by active proteins to regenerate the surface. In addition, the isolation of proteins is costly and the application of the device for hydrogen production is uneconomic at the moment.

I propose this nanoelectronic device as a platform technology that allows comparison of different catalytic building blocks and coupling methods. Proteins from various organisms may be coupled via different subunits of photosystem I (e.g. PsaC or PsaD) or via artificial, redox-active linker molecules. The efficiency of the electron transfer and the influence of competitive electron acceptors can be quantified for the resulting hybrid complexes. An efficient electron transfer from PS1 to hydrogenase will allow an increase of the hydrogen production because less electrons are “lost” to other metabolic pathways like NADP<sup>+</sup> reduction by ferredoxin:NADP<sup>+</sup>-reductase.

Such knowledge provides the molecular basis for enhancing the yield of hydrogen evolution in living microorganisms. In the future, the most promising complexes will be introduced into cellular systems like cyanobacteria or green algae. If the hydrogen is produced by cells, the costly protein isolation is not necessary any more, inactive proteins are automatically replaced, and a continuous hydrogen production is possible. The remaining challenge will be to create a system which uses as much energy as possible for hydrogen production, but still provides enough energy for the metabolic pathways which are necessary for cell growth.

Hydrogen will be produced by bioreactors which only need sufficient illumination. No fertile ground is required, which remains available for food production.

### **5.3 Structural investigation of protein monolayers**

Protein monolayers are not perfectly homogenous. With SEIRAS we are able to distinguish several surface structures, which contribute to the measured spectrum. The respective surface structure might have an effect on the local activity of the bound proteins.

In an attempt to reveal the lateral distribution of the chemical composition of the solid-supported membrane, we applied scanning near-field infrared microscopy (SNIM), a combination of IR spectroscopy and atomic force microscopy, with the aim to resolve the spectral information in 2D. We were able to correlate IR spectroscopic data with topographic heights. The membrane protein cytochrome c oxidase was immobilized on a Ni-NTA monolayer in an upstanding position, with the membrane plane parallel to the surface. The surface-tethered proteins were reconstituted in a non-perfect lipid membrane.

In the future, the combination with electrochemistry might allow localized activity measurements. This method might also answer the question to what extent the activity of membrane proteins is affected by the protein:lipid ratio in a lipid membrane.

## 6 References

Adams, M.W.W., Mortenson, L.E., Chen, J.S., 1980. Hydrogenase. *Biochim. Biophys. Acta* 594, 105-176.

Adams, M.W.W., 1990. The structure and mechanism of iron-hydrogenases. *Biochim. Biophys. Acta* 1020(2), 115-145.

Alivisatos, P., Cummings, P., Yoreo, J.D., Fichthorn, K., Gates, B., Hwang, R., Lowndes, D., Majumdar, A., Makowski, L., Michalske, T., 2004. Nanoscience research for energy needs: Report of the National Nanotechnology Initiative. Grand Challenge Workshop; The National Nanotechnology Coordination Office: Arlington.

Anderson, M. S., 2003. Enhanced infrared absorption with dielectric nanoparticles. *Appl. Phys. Lett.* 83, 2964-2966.

Armstrong, F.A., Fontecilla-Camps, J.C., 2008. *Biochemistry*. A natural choice for activating hydrogen. *Science* 321, 498-499.

Armstrong, S.H., Budka, M.J.E., Morrison, K.C., Hasson, M., 1947. Preparation and properties of serum and plasma proteins. XII. The refractive properties of the proteins of human plasma and certain purified fractions. *J. Am. Chem. Soc.* 69, 1747-1753.

Aroca, R.F, Ross, D.J., 2004. Surface-enhanced infrared spectroscopy. *Appl. Spectrosc.* 58, 324A-338A.

Ataka, K., Yotsuyanagi, T, Osawa, M., 1996. Potential-dependent reorientation of water molecules at an electrode/electrolyte interface studied by surface-enhanced infrared absorption spectroscopy. *J. Phys. Chem.* 100, 10664-10672.

Ataka, K., Osawa, M., 1998. In situ infrared study of water-sulfate coadsorption on gold(111) in sulfuric acid solutions. *Langmuir* 14(4), 951-959.

Ataka, K., Osawa, M., 1999. In situ infrared study of cytosine adsorption on gold electrodes. *J. Electroanal. Chem.* 460, 188-196.

Ataka, K., Heberle, J., 2003. Electrochemically induced surface-enhanced infrared difference absorption (SEIDA) spectroscopy of a protein monolayer. *J. Am. Chem. Soc.* 125, 4986-4987.

Ataka, K., Giess, F., Knoll, W., Naumann, R., Haber-Pohlmeier, S., Richter, B., Heberle, J., 2004. Oriented attachment and membrane reconstitution of His-tagged cytochrome c oxidase to a gold electrode: In situ monitoring by surface-enhanced infrared absorption spectroscopy. *J. Am. Chem. Soc.* 126, 16199-16206.

Ataka, K., Heberle, J., 2007. Biochemical applications of surface-enhanced infrared absorption spectroscopy. *Anal. Bioanal. Chem.* 388(1), 47-54.

Badura, A., Esper, B., Ataka, K., Grunwald, C., Wöll, C., Kuhlmann, J., Heberle, J., Rögner, M., 2006. Light-driven water splitting for (bio-)hydrogen production: Photosystem 2 as the central part of a bioelectrochemical device. *Photochem. Photobiol.* 82, 1385-1390.

Baffert, C., Demuez, M., Cournac, L., Burlat, B., Guigliarelli, B., Bertrand, P., Girbal, L., Léger, C., 2008. Hydrogen-activating enzymes: Activity does not correlate with oxygen sensitivity. *Angew. Chem.* 120(11), 2082-2084.

Berg, J.M., Tymoczko, J.L., Stryer, L., 2003. *Biochemie*. Spektrum Akademischer Verlag: Berlin, Germany, 5<sup>th</sup> Ed.

BMWi (Bundesministerium für Wirtschaft und Technologie), 2008. *Energiestatistik: Erneuerbare Energien*. [www.bmwi.de](http://www.bmwi.de)



Byler, D.M., Susi, H., 1986. Examination of secondary structure of proteins by deconvolved FTIR spectra. *Biopolymers* 25, 469-487.

Cammack, R., Frey, M., Robson, R., 2001. Producing hydrogen as a fuel. In: Cammack, R., Frey, M., Robson, R., *Hydrogen as a fuel: Learning from nature*. Routledge, UK, pp. 201-230.

Carmeli, I., Frolov, L., Carmeli, C., Richter, S., 2007. Photovoltaic activity of photosystem I-based self-assembled monolayer. *J. Am. Chem. Soc.* 129, 12352–12353.

Chance, B., 1957. Techniques for the assay of the respiratory enzymes, *Meth. Enzymol.* 4, 273-329.

Chen, X., Ferrigno, R., Yang, J., Whitesides, G.A., 2002. Redox properties of cytochrome c adsorbed on self-assembled monolayers: A probe for protein conformation and orientation. *Langmuir* 18(18), 7009-7015.

Ciesielski, P.N., Scott, A.M., Faulkner, C.J., Berron, B.J., Cliffel, D.E., Jennings, G.K., 2008. Functionalized nanoporous gold leaf electrode films for the immobilization of photosystem I. *ACS Nano.* 2, 2465-2472.

Cohen, Y., Chitnis, V.P., Nechushtai, R., Chitnis, P.R., 1993. Stable assembly of Psae into cyanobacterial photosynthetic membranes is dependent on the presence of other accessory subunits of photosystem I. *Plant. Mol. Biol.* 23, 895-900.

Cotton, T.M., Schultz, S.G., van Duyne, R.P., 1980. Surface-enhanced resonance raman scattering from cytochrome c and myoglobin adsorbed on a silver electrode. *J. Am. Chem. Soc.* 102, 7960-7962.

Cotton, F.A., Wilkinson G., 1988. *Advanced inorganic chemistry*. Wiley: New York, USA.

Das, R., Kiley, P.J., Segal, M., Norville, J., Yu, A.A., Wang, L.Y., Trammell, S.A., Reddick, L.E., Kumar, R., Stellacci, F., 2004. Integration of photosynthetic protein molecular complexes in solid-state electronic devices. *Nano Lett.* 4, 1079–1083.

Doenecke, D., Koolman, J., Fuchs, G., Gerok, W., 2005. *Karlsons Biochemie und Pathobiochemie*. Georg Thieme Verlag: Stuttgart, Germany, 15<sup>th</sup> Ed.

Eddowes, M.J., Hill, H.A.O., 1977. Novel method for the investigation of the electrochemistry of metalloproteins: cytochrome c. *J. Chem. Soc. Chem. Commun.* 21, 771b-772.

EIA (Energy Information Agency), 2008. *World energy projections plus*. Official energy statistics from the U.S. government. Report #:DOE/EIA-0484.

Evans, M.C.W., Heathcote, P., 1980. Effects of glycerol on the redox properties of the electron acceptor complex in spinach photosystem I particles. *Biochim. Biophys. Acta* 590, 89-96.

Fontecilla-Camps, J.C., Volbeda, A., Cavazza, C., Nicolet, Y., 2007. Structure/function relationships of [NiFe]- and [FeFe]-hydrogenases. *Chem. Rev.* 107, 4273-4303.

Forestier, M., King, P., Zhang, L., Posewitz, M., Schwarzer, S., Happe, T., Ghirardi, M.L., Seibert, M., 2003. Expression of two [Fe]-hydrogenases in *Chlamydomonas reinhardtii* under anaerobic conditions. *Eur. J. Biochem.* 270(13), 2750-2758.

Gennis, R.B., Casey, R.P., Azzi, A., Ludwig, B., 1982. Purification and characterization of the cytochrome c oxidase from *Rhodospseudomonas sphaeroides*. *Eur. J. Biochem.* 125, 189-195.

Giess, F., Friedrich, M., Heberle, J., Naumann, R., Knoll, W., 2004. The protein-tethered lipid bilayer: a novel mimic of the biological membrane. *Biophys. J.* 87, 3213-3220.

Girbal, L., von Abendroth, G., Winkler, M., Benton, P.M.C., Meynial-Salles, I., Croux, C., Peters, J.W., Happe, T., Soucaille, P., 2005. Homologous and heterologous overexpression in *Clostridium acetobutylicum* and characterization of purified clostridial and algal Fe-only hydrogenases with high specific activities. *Appl. Environ. Microbiol.* 71(5), 2777-2781.

Goldet, G., Wait, A.F., Cracknell, J.A., Vincent, K.A., Ludwig, M., Lenz, O., Friedrich, B., Armstrong, F.A., 2008. Hydrogen production under aerobic conditions by membrane-bound hydrogenases from *Ralstonia* species. *J. Am. Chem. Soc.* 130, 11106-11113.

Gray, H.B., Malmstrom, B.G., Williams, R.J.P., 2000. Copper coordination in blue proteins. *J. Biol. Inorg. Chem.* 5, 551-559.

Gray, H.B., 2009. Powering the planet with solar fuel. *Nature Chemistry* 1, 7.

Grimme, R.A., Lubner, C.E., Bryant, D.A., Golbeck, J.H., 2008. Photosystem I/molecular wire/metal nanoparticle bioconjugates for the photocatalytic production of H<sub>2</sub>. *J. Am. Chem. Soc.* 130, 6308-6309.

Hambourger, M., Gervaldo, M., Svedruzic, D., King, P.W., Gust, D., Ghirardi, M., Moore, A.L., Moore, T.A., 2008. [FeFe]-hydrogenase-catalyzed H<sub>2</sub> production in a photoelectrochemical biofuel cell. *J. Am. Chem. Soc.* 130(6), 2015-2022.

Hamelin, A., Morin, S., Richer, J., Lipkowski, J., 1990. Adsorption of pyridine on the (311) face of silver. *J. Electroanal. Chem.* 285, 249-262.

Hamelin, A., Morin, S., Richer, J., Lipkowski, J., 1991. Adsorption of pyridine on the (210) face of silver. *J. Electroanal. Chem.* 304, 195-209.

Happe, T., Kaminski, A., 2002. Differential regulation of the Fe-hydrogenase during anaerobic adaptation in the green alga *Chlamydomonas reinhardtii*. 269(3), 1022-1032.

Happe, T., Naber, J.D., 1993. Isolation, characterization and N-terminal amino acid sequence of hydrogenase from the green alga *Chlamydomonas reinhardtii*. *Eur. J. Biochem.* 214(2), 475-481.

Heineman, W.R., Norris, B.J., Goelz, J.F., 1975. Measurement of enzyme E'values by optically transparent thin layer electrochemical cells. *Anal. Chem.* 47, 79-84.

Hellwig, C., Barthels, N., Salfner, K., Siepchen, B., Weber, C., Krassen, H., 2009. Ist unser Klima noch zu retten? *Bunsenmagazin* 11, 14-19.

Herres, W., Gronholz, J., 1985. Understanding FT-IR data processing. Dr. Alfred Hüthig Publishers.

Hexter, R.M., Albrecht, M.G., 1979. Metal surface Raman spectroscopy: Theory. *Spectrochim. Acta: Part A.* 35, 233-251.

Higuchi, Y., Yagi, T., Yasuoka, N., 1997. Unusual ligand structure in Ni-Fe active center and an additional Mg site in hydrogenase revealed by high resolution X-ray structure analysis. *Structure* 5, 1671-1680.

Horcas, I., Fernandez, R., Gomez-Rodriguez, J.M., Colchero, J., Gomez-Herrero, J., Baro, A.M., 2007. WSXM: A software for scanning probe microscopy and a tool for nanotechnology. *Rev. Sci. Instrum.* **78**, 013705.

Horner, D., Heil, B., Happe, T., Embley, M., 2002. Iron hydrogenases, ancient enzymes in modern eukaryotes. *Trends Biochem. Sci.*, 27, 148-153.

Hosler, J.P., Fetter, J., Tecklenburg, M.M., Espe, M., Lerma, C., Ferguson-Miller, S., 1992. Cytochrome aa<sub>3</sub> of *Rhodobacter sphaeroides* as a model for mitochondrial cytochrome c oxidase. Purification kinetics, proton pumping, and spectral analysis. *J. Biol. Chem.* 267, 24264-24272.

Ihara, M., Nishihara, H., Yoon, K., Lenz, O., Friedrich, B., Nakamoto, H., Kojima, K., Honma, D., Kamachi, T., Okura, I., 2006. Light-driven hydrogen production by a hybrid complex of a [NiFe]-hydrogenase and the cyanobacterial photosystem I. *Photochem. Photobiol.* 82, 676-682.

Jensen, T.R., van Duyne, R.P., Johnson, S.A., Maroni, V.A., 2000. Surface-enhanced infrared spectroscopy: A comparison of metal island films with discrete and nondiscrete surface plasmons. *Appl. Spectrosc.* 54, 371-377.

Jiang, X., Ataka, K., Heberle, J., 2008. Influence of the molecular structure of carboxyl-terminated self-assembled monolayer on the electron transfer of cytochrome c adsorbed on an Au electrode: In situ observation by surface-enhanced infrared absorption spectroscopy. *J. Phys. Chem. C* 112(3), 813-819.

Jordan, P., Fromme, P., Witt, H.T., Klukas, O., Saenger, W., Krauss N., 2001. Three-dimensional structure of cyanobacterial photosystem I at 2.5 Å resolution. *Nature.* 411, 909-917.

Kamp, C., Silakov, A., Winkler, M., Reijerse, E.J., Lubitz, W., Happe, T., 2008. Isolation and first EPR characterization of the [FeFe]-hydrogenases from green algae. *Biochim. Biophys. Acta* 1777, 410-416.

Karyakin, A.A., Morozov, S.V., Karyakina, E.E., Zorin, N.A., Perelygin, V.V., Cosnier, S., 2005. Hydrogenase electrodes for fuel cells. *Biochem. Soc. Trans.* 33, 73-75

Knoll, B., Keilmann, F., 1999. Near-field probing of vibrational absorption for chemical microscopy. *Nature* 399, 134-137.

Kôno, T., Nakamura, S., 1958. Electrolytic reductions of diphosphopyridine nucleotide, triphosphopyridine nucleotide, and cytochrome c at controlled potentials. *Bull. Agric. Chem. Soc. Japan* 22, 399-403.

Kopf, I., Samson, J.-S., Wollny, G., Grunwald, C., Bründermann, E., Havenith, M., 2007. Chemical imaging of microstructured self-assembled monolayers with nanometer resolution. *J. Phys. Chem. C* 111, 8166-8171.

Krassen, H., Stripp, S., von Abendroth, G., Ataka, K., Happe, T., Heberle, J., 2009. Immobilization of [FeFe]-hydrogenase CrHydA1 on a gold electrode: Design of a catalytic surface for the production of molecular hydrogen. *J. Biotechnol.* Doi:10.1017/j.biotech.2009.01.18.

Krause, N., 2008. BA-thesis. Einfluss von pH-Wert und Potential auf einen Mercaptoundekansäure-Monolayer. Bielefeld University, Department of Chemistry, Workgroup Prof. Heberle.

Kretschmann, E., Raether, H., 1968. Radiative decay of non-radiative surface plasmons excited by light. *Z. Naturforschung*, 23, 2135-2136.

Krimm, S., Bandekar, J., 1986. Vibrational spectroscopy and conformation of peptides, polypeptides, and proteins. *Adv. Protein Chem.* 38, 181-364.

Kuznetsov, B.A., Mestechkina, N.M., Izotov, M.V., Karuzina, I.I., Karyakin, A.V., Archakov, A.I., 1979. Electrochemical analysis of microsomal cytochromes. *Biokhimiia* 44, 1234- 1239.

Larminie, J., Dicks, A., 2003. Fuel Cell Systems Explained. Wiley: Chichester, U.K., 2<sup>nd</sup> Ed.

Léger, C., Dementin, S., Bertrand, P., Rousset, M., Guigliarelli, B., 2004. Inhibition and aerobic inactivation kinetics of *Desulfovibrio fructosovorans* NiFe hydrogenase studied by protein film voltammetry. *J. Am. Chem. Soc.* 126, 12162-12172.

Lewis, R.N.A.H., McElhaney, R.N. 2002. Vibrational spectroscopy of lipids; in *Handbook of Vibrational Spectroscopy* Chalmers, J.M., Griffiths, P.R., Eds., Wiley: Chichester, U.K., 3465-3480.

Lewis, N.S., Wrighton, M.S., 1981. Electrochemical reduction of horse heart ferricytochrome c at chemically derivatized electrodes. *Science* 211, 944 - 947.

Ludwig, M., Cracknell, J.A., Vincent, K.A., Armstrong, F.A., Lenz, O., 2009. Oxygen-tolerant H<sub>2</sub> oxidation by membrane-bound [NiFe] hydrogenases of *Ralstonia* species. Coping with low level H<sub>2</sub> in air. *J. Biol. Chem.* 284, 465-477.

Lushy, A., Verchovsky, L., Nechushtai, R., 2002. The stable assembly of newly synthesized PsaE into the photosystem I complex occurring via the exchange mechanism is facilitated by electrostatic interactions. *Biochemistry* 41, 11192-11199.

Mitchell, D.M., Gennis, R.B., 1995. Rapid purification of wildtype and mutant cytochrome c oxidase from *Rhodobacter sphaeroides* by Ni(2+)-NTA affinity chromatography. *FEBS Lett.* 368, 148-150.

Miyake, H., Ye, S., Osawa, M., 2002. Electroless deposition of gold thin films on silicon for surface-enhanced infrared spectroelectrochemistry. *Electrochem. Commun.* 4, 973-977.

Moskovitz, M., 1985. Surface-enhanced spectroscopy. *Rev. Mod. Phys.* 57, 783-826.

Nakajima, N., Ikada, Y., 1995. Mechanism of amide formation by carbodiimide for bioconjugation in aqueous media. *Bioconjugate Chem.* 6, 123-130.

Nicolet, Y., Piras, C., Legrand, P., Hatchikian, C.E., Fontecilla-Camps, J.C., 1999. *Desulfovibrio desulfuricans* iron hydrogenase: the structure shows unusual coordination to an active site Fe binuclear center. *Structure* 7, 13-23.

Nicolet, Y., Lemon, B.J., Fontecilla-Camps, J.C., Peters, J.W., 2000. A novel FeS cluster in Fe-only hydrogenases. *Trends Biochem. Sci.* 25, 138-143.

Nicolet, Y., de Lacey, A.L., Vernède, X., Fernandez, V.M., Hatchikian, E.C., Fontecilla-Camps, J.C., 2001. Crystallographic and FTIR spectroscopic evidence of changes in Fe coordination upon reduction of the active site of the Fe-only hydrogenase from *Desulfovibrio desulfuricans*. *J. Am. Chem. Soc.* 123, 1596-1601.

Osawa, M., Ikeda, M., 1991. Surface-enhanced infrared absorption of p-nitrobenzoic acid deposited on silver island films: Contributions of electromagnetic and chemical mechanisms. *J. Phys. Chem.* 95, 9919-9924.

Osawa, M., Ataka, K., Yoshii, K., Yotsuyanagi, T.J., 1993. Surface-enhanced infrared ATR spectroscopy for in situ studies of electrode/electrolyte interfaces. *Electron Spectrosc. Relat. Phenom.* 64-65, 371-379.

Osawa, M., 1997. Dynamic Processes in Electrochemical Reactions Studied by Surface-Enhanced Infrared Absorption Spectroscopy (SEIRAS). *Bull. Chem. Soc. Jpn.* 70, 2861-2880.

Osawa, M., 2002. Surface-enhanced infrared absorption spectroscopy. In: Chalmers, J.M., Griffiths, P.R. (Eds.), *Handbook of vibrational spectroscopy*, Wiley, Chichester, U.K., 785-799.



Pearce, H.A., Sheppard, N., 1976. Possible importance of a “metal-surface selection rule” in the interpretation of the infrared spectra of molecules adsorbed on particulate metals; infrared spectra from ethylene chemisorbed on silica-supported metal catalysts. *Surf. Sci.* 59, 205-217.

Peters, J.W., Lanzilotta, W.N., Lemon, B.J., Seefeldt, L.C., 1998. X-ray crystal structure of the Fe-only hydrogenase (CpI) from *Clostridium pasteurianum* to 1.8 angstrom resolution. *Science* 282, 1853-1858.

Pierik, A.J., Hulstein, M., Hagen, W.R., Albracht, S.P.J., 1998. A low-spin iron with CN and CO as intrinsic ligands forms the core of the active site in [Fe]-hydrogenase. *Eur. J. Biochem.* 258, 572-578.

Salomon, A., Boecking, T., Seitz, O., Markus, T., Amy, F., Chan, C., Zhao, W., Cahen, D., Kahn, A., 2007. What is the barrier for tunneling through alkyl monolayers? Results from n- and p-Si-Alkyl/Hg junctions. *Adv. Mater.* 19, 445-450.

Scheller, F., Jänchen, M., Lampe, J., Priimke, H.-J., Blank, J., Palecek, E., 1975. Studies on electron transfer between mercury electrode and hemoprotein. *Biochim. Biophys. Acta* 412, 157-167.

Schwarze, A., (probably) 2009. PhD-thesis. Humboldt-University Berlin, Department of Microbiology, Workgroup Prof. Friedrich.

Song, S., Clark, R.A., Bowden E.F., Tarlov, M.J., 1993. Characterization of cytochrome *c*/alkanethiolate structures prepared by self-assembly on gold. *J. Phys. Chem.* 97(24), 6564-6572.

Sonoike, K., Hatanaka, H., Katoh, S., 1993. Small subunits of photosystem I reaction center complexes from *Synechococcus elongates*. II. The *psaE* gene product has a role to promote interaction between the terminal electron acceptor and ferredoxin. *Biochim. Biophys. Acta* 1141, 52-57.

Stenberg, E., Persson, B., Roos, H., Urbaniczky, C., 1991. Quantitative determination of surface concentration of protein with surface plasmon resonance using radiolabeled proteins. *J. Colloid and Interface Science* 143, 513-526.

Stombaugh, N.A., Sundquist, J.E., Burris, R.H., Orme-Johnson, W.H., 1976. Oxidation-reduction properties of several low potential iron-sulfur proteins and of methylviologen. *Biochemistry* 15(12), 2633-2641.

Sun, L., Crooks, R.M., Ricco, A.J., 1993. Molecular interactions between organized, surface-confined monolayers and vapor-phase probe molecules. 5. Acid-base interactions. *Langmuir* 9(7), 1775-1780.

Tamamushi, R., Tanaka, K., 1987. Effect of methylviologen on the hydrogen evolution at mercury electrodes in aqueous buffer solutions. *J. Electroanal. Chem.* 230, 177-188.

Terasaki, N., Yamamoto, N., Hiraga, T., Sato, I., Inoue, Y., Yamada, S., 2006. Fabrication of novel photosystem I gold nanoparticle hybrids and their photocurrent enhancement. *Thin Solid Films.* 499, 153–156.

Thomann, H., Bernardo, M., Adams, M.W.W., 1991. Pulsed ENDOR and ESEEM spectroscopic evidence for unusual nitrogen coordination to the novel hydrogen-activating iron-sulfur center in hydrogenase. *J. Am. Chem. Soc.* 113, 7044-7046.

Uchida, T., Mogami, H., Yamakata, A., Sasaki, Y., Osawa, M., 2008. Hydrogen evolution reaction catalyzed by proton-coupled redox cycle of 4,4'-bipyridine monolayer adsorbed on silver electrodes. *J. Am. Chem. Soc.* 130, 10862-10863.

van der Spek, T.M., Arendsen, A.F., Happe, R.P., Yun, S., Bagley, K.A., Stufkens, D.J., Hagen, W.R., Albracht, S.P.J., 1996. Similarities in the architecture of the active sites of Ni-hydrogenases and Fe-hydrogenases detected by means of infrared spectroscopy. *Eur. J. Biochem.* 237, 629-634.

Vignais, P.M., Billoud, B., 2007. Occurrence, classification, and biological function of hydrogenases: an overview. *Chem. Rev.* 107, 4206-4272.

Vincent, K.A., Parkin, A., Lenz, O., Albracht, S.P.J., Fontecilla-Camps, J.C., Cammack, R., Friedrich, B., Armstrong, F.A., 2005. Electrochemical definitions of O<sub>2</sub> sensitivity and oxidative inactivation in hydrogenases. *J. Am. Chem. Soc.* 127(51), 18179-18189.

Volbeda, A., Charon, M.H., Piras, C., Hatchikian, C.E., Frey, M., Fontecilla-Camps, J.C., 1995. Crystal structure of the nickel-iron hydrogenase from *Desulfovibrio gigas*. *Nature* 373, 580-587.

von Abendroth, G., Stripp, S., Silakov, A., Croux, C., Soucaillec, P., Girbal, L., Happe, T., 2008. Optimized over-expression of [FeFe] hydrogenases with high specific activity in *Clostridium acetobutylicum*. *Int. J. Hydrogen Energ.* 33, 6076-6081.

Webber, A.N., Su, H., Bingham, S.E., Kss, H., Krabben, L., Kuhn, M., Jordan, R., Schlodder, E., Lubitz, W., 1996. Site-directed mutations affecting the spectroscopic characteristics and midpoint potential of the primary donor in photosystem I. *Biochemistry* 35, 12857-12863.

Wiesenborn, D.P., Rudolph, F.B., Papoutsakis, E.T., 1988. Thiolase from *Clostridium acetobutylicum* ATCC 824 and its role in the synthesis of acids and solvents. *Appl. Environ. Microbiol.* 54, 2717-2722.

Xu, J., Bowden, E.F., 2006. Determination of the orientation of adsorbed cytochrome c on carboxyalkanethiol self-assembled monolayers by in situ differential modification. *J. Am. Chem. Soc.* 128(21), 6813-6822.

Yang, W.H., Schatz, G.C., van Duyne, R.P., 1995. Discrete dipole approximation for calculating extinction and Raman intensities for small particles with arbitrary shapes. *J. Chem. Phys.* 103, 869-875.

---

Zaugg, W.S., 1964. Spectroscopic characteristics and some chemical properties of N-methylphenazinium methyl sulfate (Phenazine methosulfate) and pyocyanine at the semiquinoid oxidation level. *J. Biol. Chem.* 239, 3964-3970.

## 7 Acknowledgements

Many people supported me during my Ph.D. and I wish to express my gratitude wholeheartedly.

I wish to thank my Ph.D. advisor, Joachim Heberle, for his motivating interest in my work all the time, for all the helpful advices, and fruitful discussions. I also wish to thank my other supervisor, Kenichi Ataka. He taught me the fundamental methods, which I used in my thesis, and he always had time to discuss my problems and ideas.

I enjoyed the work in our laboratory. The atmosphere fostered my scientific work. I want to thank all my colleagues for their interest in my work as well as for their talks and discussions about related topics. In particular, I want to thank Michael Schleegeer. His investigation of the cytochrome c oxidase was closely related to my work on photosynthesis and I highly value our discussions and joint projects.

Thanks to Uwe Güth and Sandra Gericke, whose help with administration and organization were indispensable. And they were irreplaceable with respect to our excellent working atmosphere.

I am deeply grateful for the work of our machine shop. Manfred Hoffmann and his colleagues constructed all the devices which I asked them for. The quality of their work was excellent, exceeded my expectation more than once, and was the basis for many of the measurements which I presented in this work.

Excellent and delightful collaborations were the key to success. I want to thank all my collaborators for adding new perspectives to our joint projects.

I started my first collaboration with the laboratory of Thomas Happe. Gregory von Abendroth and his successor Sven Stripp introduced me to hydrogenases and taught me all the small tricks to keep even traces of oxygen out of my samples. And, of course, I'm very grateful for the constant protein supply.

Thanks to the workgroup of Bärbel Friedrich. In particular, thanks to Alexander Schwarze for all the time and work he has spent to purify proteins for my measurements and for our fruitful discussions. I'm very grateful for our active knowledge exchange between microbiology and biophysics.

I want to thank Martina Havenith and her workgroup. I came to her lab for several weeks and really enjoyed my visits. Organization was perfect as well as the scientific collaboration with Ilona Kopf and Fouad Ballout.

Thanks to all members of the Kruse lab for the friendly and professional introduction to gas chromatography.

I also want to thank Norbert Sewald and his Ph.D. student Katrin Wollschläger for introducing me to surface plasmon resonance. The experiments complemented my previous work perfectly and were a milestone in my work.

I gratefully acknowledge financial support by the BMBF (Grundlagen für einen biotechnologischen und biomimetischen Ansatz der Wasserstoffproduktion). I want to thank the BMBF not only for paying my work but also for their interest in the field of renewable energies.

Thanks to Rolf Volles, my chemistry teacher during secondary school. I would not have started to study biochemistry without his inspiring chemistry lessons.

Thanks to all of my friends, they made the time at Bielefeld University unforgettable.

Mein größter Dank richtet sich an meine Eltern, Ruth und Eckhard Krassen. Ohne ihre Liebe und fortwährende Unterstützung in allen Formen würde es diese Doktorarbeit nicht geben.

## 8 Curriculum vitae

### Henning Krassen

Date of birth: 06.08.1981

Place of birth: Leverkusen (Germany)

Nationality: German



- Since 02'2006 Ph.D. thesis  
Bielefeld University  
Topic: "Biomimetic Hydrogen Production"  
Supervisor: Prof. Dr. Joachim Heberle
- 10'2001 – 01'2006 Studies of Biochemistry  
Bielefeld University  
Grading of diploma: "A"  
Topic of diploma thesis: "Field-induced pore formation in the membrane of single CHO-cells"  
Supervisor: Prof. Prof. h.c. Drs. h.c. Eberhard Neumann
- 07'2000 – 05'2001 Civilian service  
Hospital Düsseldorf-Benrath
- 07'1991 – 06'2000 Secondary school  
Annette-von-Droste-Hülshoff-Gymnasium  
Grading of diploma: "A" (1.1)
- 07'1987 – 06'1991 Primary school  
Städt. Gemeinschaftsgrundschule Düsseldorf

## 9 Supplementary information

### 9.1 Sample changer for transmission setup

The sample changer allows moving two transmission samples in and out of the IR beam. The position of the sample holder can be switched between two positions by an external trigger signal, while the sample changer remains in the purged sample chamber of the spectrometer. It is possible to exchange both samples as well as changing the position on the same sample. The sample holder is moved almost perpendicular to the optical path, but tilted by  $9^\circ$  in order to avoid internal reflections in the used sandwich samples. An overview of the construction is shown in Figure S1. The constructional drawings of the single parts are shown in Figure S2 to Figure S7.

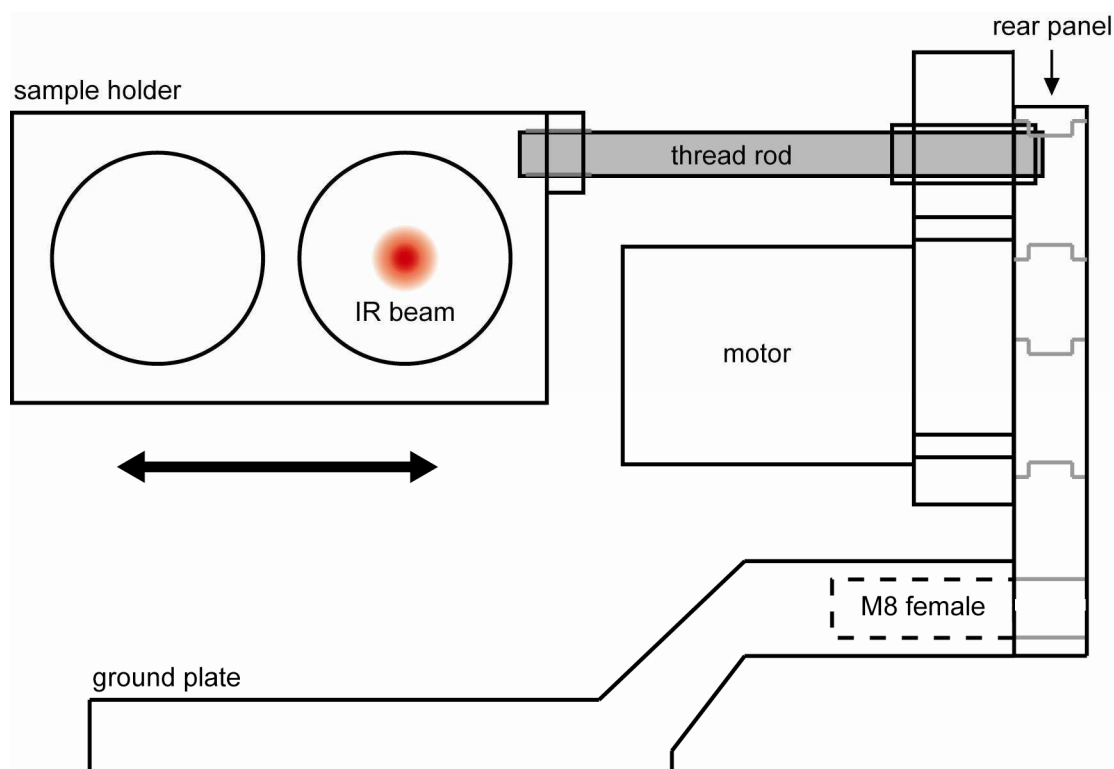


**Figure S1** Overview of the sample changer | The sample changer is shown without the slide rail of the sample holder for sake of visual clarity. The moving direction of the sample holder is indicated by an arrow and the position of the IR focus is marked by a red dot.



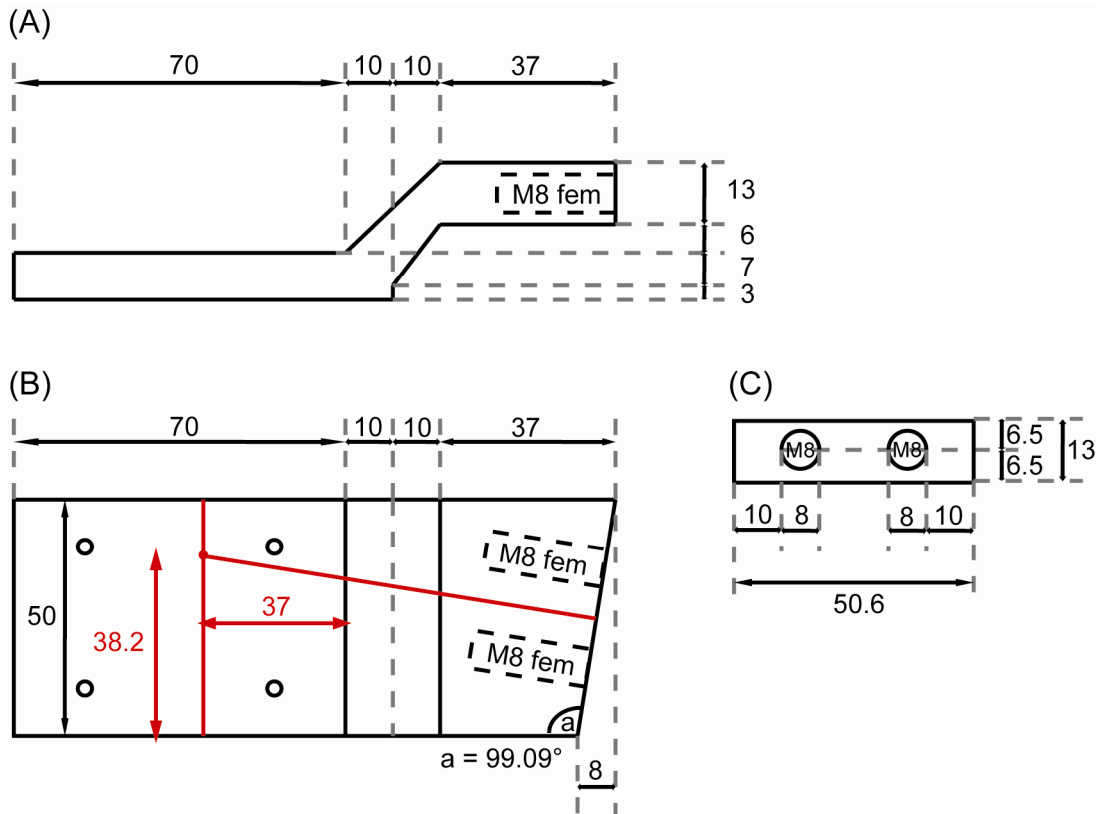


**Figure S2** Ground plate of the sample changer | (A) Side view. (B) Top view. (C) Rear view. All specification is given in millimeters.

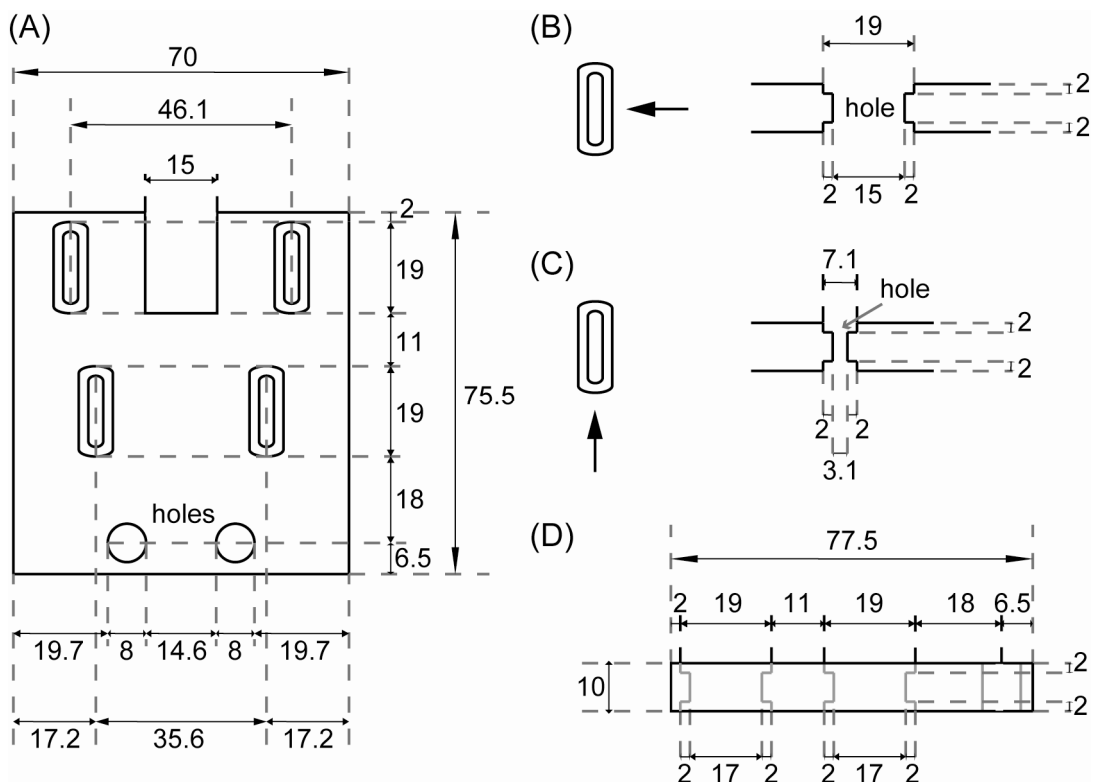


**Figure S3 Rear panel of the sample changer** / (A) Front view. (B) Side view of the long hole. The height of the motor is adjusted by the position of the screw in the long hole. (C) Side view of the long hole. Rotated by 90° with respect to (C). (D) Side view of the rear panel. All specification is given in millimeters.

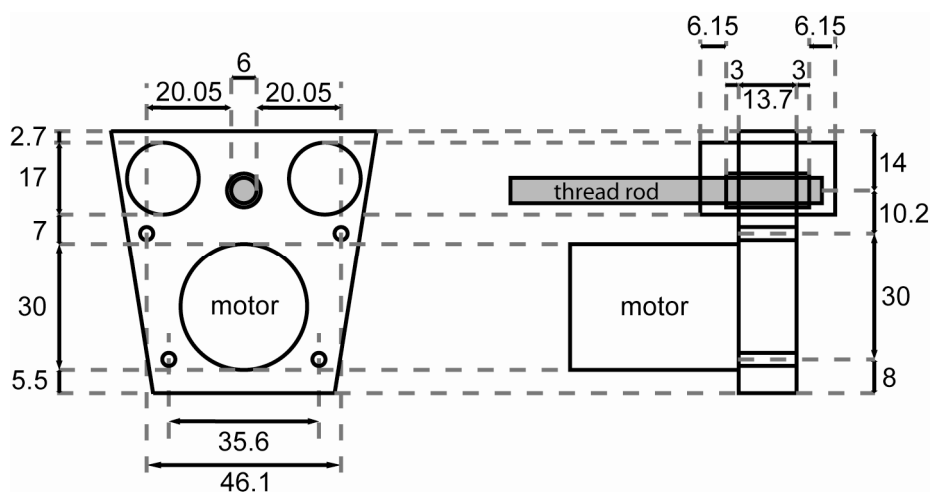


**Figure S4 Motor of the sample changer** / The motor is used to impel the thread rod. (A) Front view. (B) Side view.

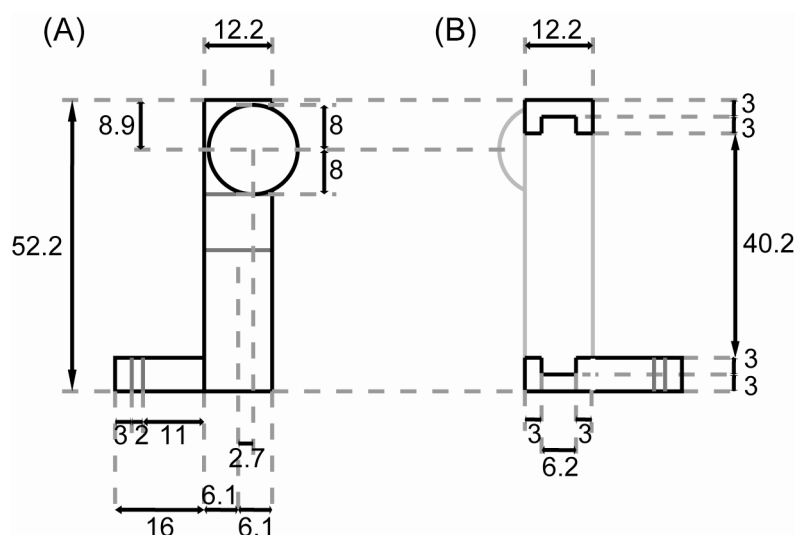


**Figure S5** Slide rail for the sample holder | The sample holder is moved along the notch. The slide rail is fixed perpendicular to the rear panel. (A) Rear view. (B) Front view.

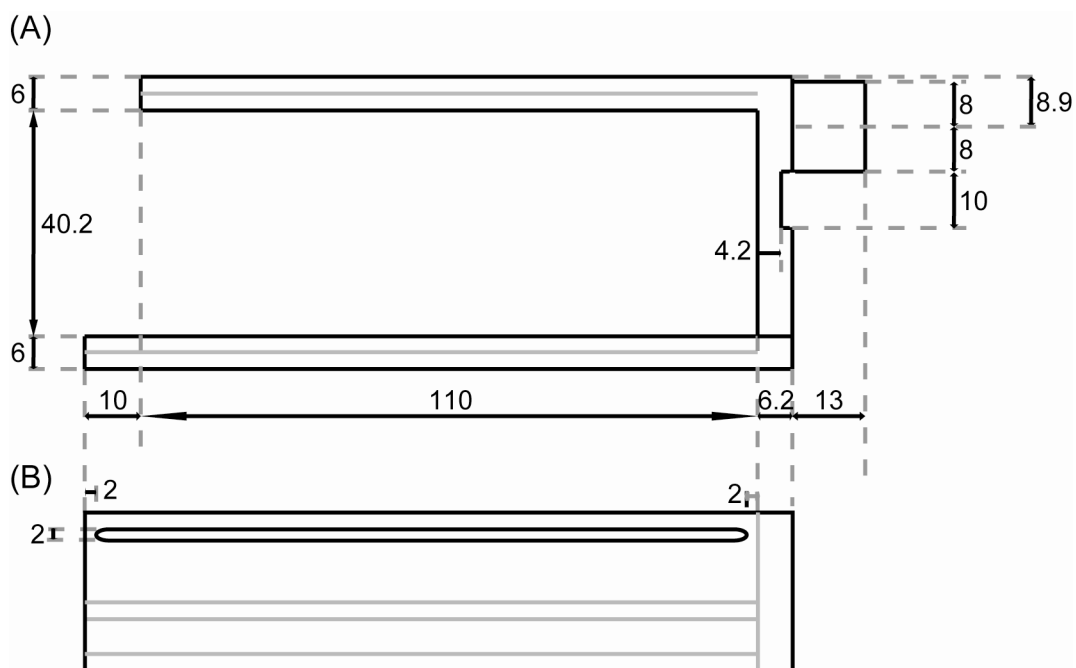


**Figure S6** Slide rail for the sample holder | (A) Side view. (B) Top view. The 2 mm cut-out is used to fix the electric contacts. The positions of the contacts define how far the sample holder is moved in each direction.

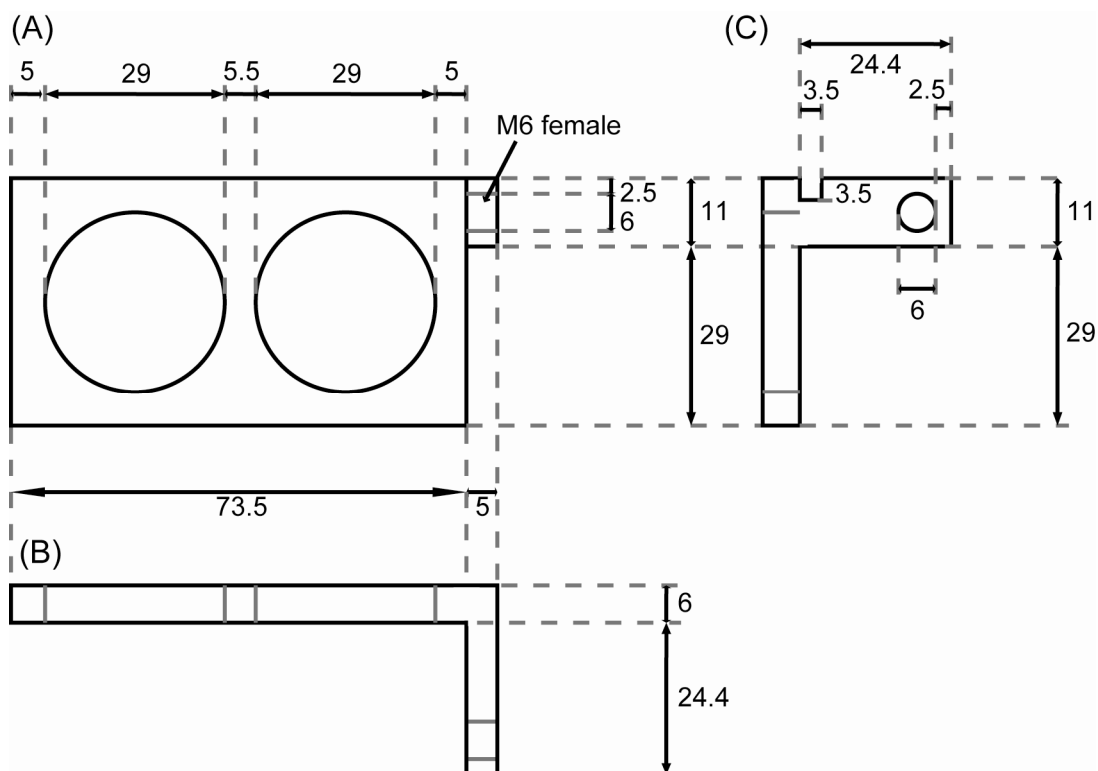


**Figure S7** *Sample holder* | Sandwich samples can be fixed in both holes. (A) Side view. (B) Top view. (C) Rear view.

## 9.2 Anaerobic SEIRAS setup

The SEIRAS optics was designed by Kenichi Ataka as shown in Figure S8. The IR beam is reflected by a mirror in an angle of  $30^\circ$ , totally reflected in the triangular silicon prism, and reflected towards the detector by a second mirror.

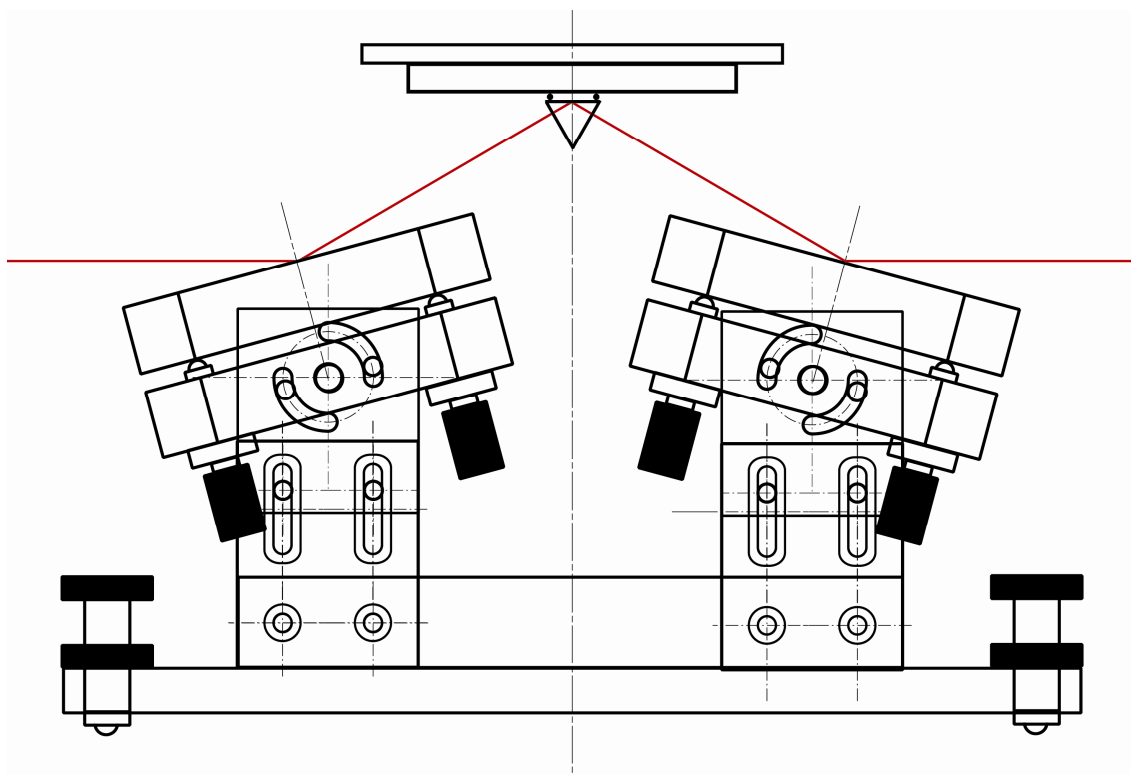


**Figure S8 SEIRAS optics** | The SEIRAS optics direct the IR beam through a triangular silicon prism. The height adjustment of the ground plate and the possibility to adjust height, position, and angle of the mirrors allow to optimize the optical throughput. The design of this optics was done by Kenichi Ataka.

In this work an oxygen-sensitive hydrogenase was investigated by SEIRA spectroscopy and the setup had to be sealed completely from the atmosphere. Thus, a glove bag was connected to the top of the sample chamber. Sample chamber and glove bag were purged with argon to avoid the intrusion of oxygen. Here, a lid (Figure S9) was designed, which fits to the sample chamber of a Bruker IFS 66v/S spectrometer and allows the connection of an exchangeable glove bag holder (Figure S10).

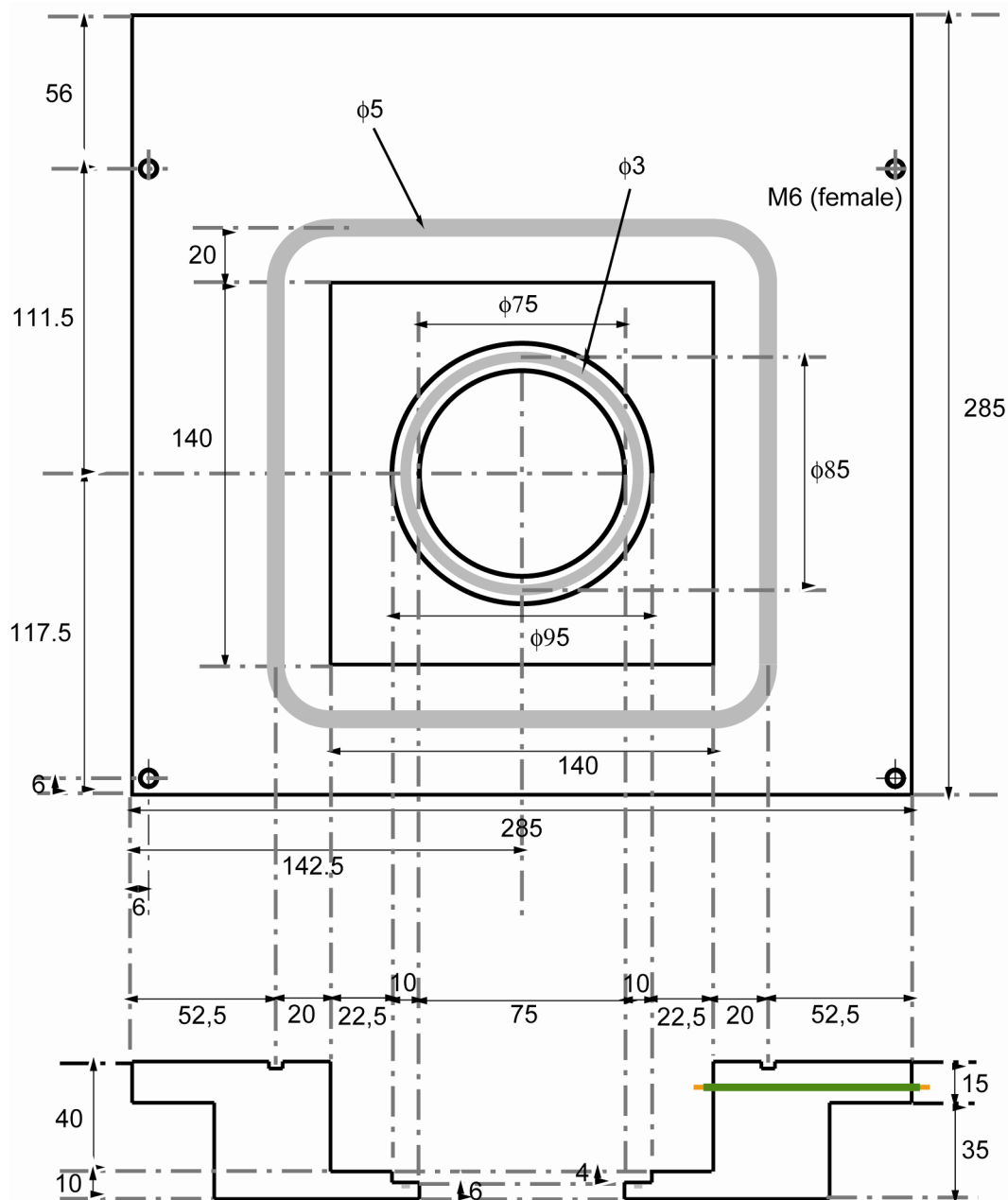


**Figure S9 SEIRA lid for the spectrometer chamber** | The lid fits to the top of the sample chamber of the Bruker IFS 66v/S spectrometer. The SEIRAS cell is placed on the central ring, bringing the silicon prism into the IR focus. Three wires are embedded in the lid to connect the SEIRAS cell (position marked in green).

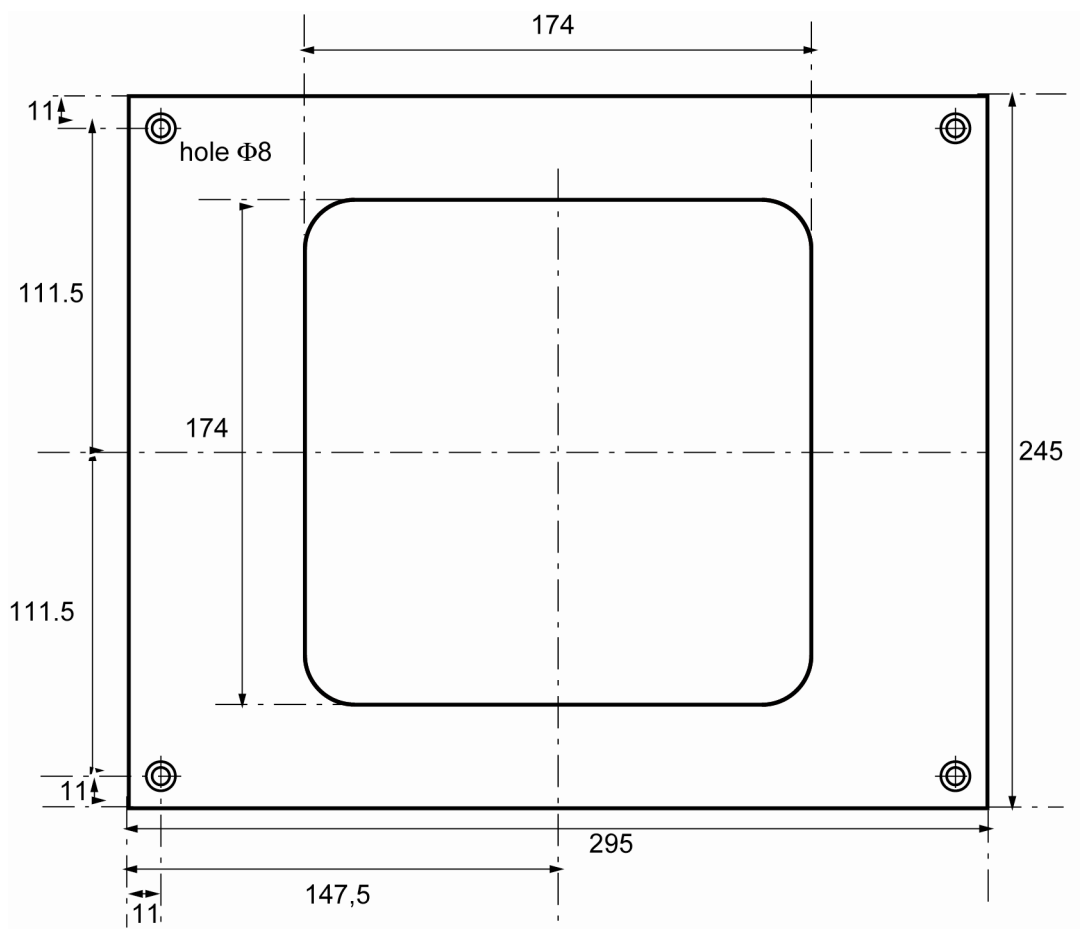


**Figure S10** *Glove bag holder for the sample changer* / The glove bag holder is screwed to the SEIRAS lid. A 3 mm Viton® O-seal is placed between both parts.

A glove bag (Sekuroka Glove Bag 45x45 cm, Carl Roth GmbH, Karlsruhe, Germany) was taped to the top of the bag holder. The latter was screwed to the SEIRAS lid. The sealing between was made from Viton, an elastic material which is impermeable for oxygen. Viton was used for all other sealings as well. In particular important was the sealing between silicon prism and glass cell (Figure 9). Although the SEIRAS cell was completely surrounded by argon, the oxygen, which was desorbed from the rubber sealing during the experiments was sufficient to inactivate the hydrogenase.

## 10 Lists

### 10.1 List of Tables

Table 1	Protein binding conditions
Table 2	Protein buffers
Table 3	IR frequencies of BBP
Table 4	Redox-induced IR frequencies of BBP
Table 5	Redox-induced IR frequencies of BBP at low potentials
Table 6	Hydrogen evolution rates
Table 7	IR frequencies of <i>CrHydA1</i> in the CO/CN region
Table 8	IR frequencies of a <i>CrHydA1</i> solution during drying

### 10.2 List of Figures

Figure 1	Light reaction of photosynthesis
Figure 2	Active site of [FeFe]-hydrogenases
Figure 3	Self-assembled monolayer
Figure 4	His-tag binding to Ni-NTA
Figure 5	Reconstitution of a membrane protein in a lipid bilayer
Figure 6	Transmission setup
Figure 7	Attenuated total reflection setup
Figure 8	Chemical gold film deposition
Figure 9	Electrochemical SEIRAS setup
Figure 10	Evanescent wave
Figure 11	Waveform for cyclic voltammetry
Figure 12	Gas chromatography setup
Figure 13	Atomic force microscopy setup



- 
- Figure 14      Template-stripped gold
- Figure 15      Scanning near-field infrared microscopy setup
- Figure 16      *CrHydA1* on a mercaptopropionic acid monolayer
- Figure 17      Surface charges of *CrHydA1*
- Figure 18      SEIRA spectra of the binding of *CrHydA1*
- Figure 19      Cyclic voltammograms of *CrHydA1* on an MUA-SAM and a bare gold electrode
- Figure 20      Cyclic voltammograms of *CrHydA1* during CO inhibition
- Figure 21      Cyclic voltammograms of *CrHydA1* on a MPA-SAM
- Figure 22      Cyclic voltammograms of 100  $\mu$ M MV on different surfaces
- Figure 23      Surface plasmon resonance signal during the binding of *CrHydA1* on an MPA-SAM
- Figure 24      Hydrogen production from *CrHydA1* on a MPA-SAM
- Figure 25      *CrHydA1* on a redox-active monolayer
- Figure 26      Chemical structure of BBP
- Figure 27      BBP binding to a bare gold surface
- Figure 28      Cyclic voltammogram of a BBP monolayer
- Figure 29      Potential-induced difference spectra of a BBP monolayer
- Figure 30      Potential-induced difference spectra of a BBP monolayer
- Figure 31      *CrHydA1* binding to a BBP monolayer
- Figure 32      Binding kinetics of *CrHydA1* on different surfaces
- Figure 33      Cyclic voltammograms of *CrHydA1* on a BBP monolayer
- Figure 34      Amperometry of *CrHydA1* on BBP during CO inhibition
- Figure 35      Hydrogen production from *CrHydA1* on a BBP-SAM
- Figure 36      Hydrogen evolution potential on different surfaces
- Figure 37      Coupling concept of hydrogenase and photosystem I
- Figure 38      Electron flow for light-induced hydrogen production
- Figure 39       $PS1_{\Delta PsaE}$  binding to a Ni-NTA monolayer

- 
- Figure 40 Binding kinetics of PsaE to its native position in PS1
- Figure 41 Binding of the fusion protein MBH<sub>PsaE</sub> to different modified surfaces
- Figure 42 Surface plasmon resonance signal during the assembly of MBH<sub>PsaE</sub>
- Figure 43 Cyclic voltammogram of PMS
- Figure 44 Photocurrent measurement of the hybrid complex PS1-MBH
- Figure 45 Action spectrum of PS1 monolayers
- Figure 46 pH dependence of the photocurrent of PS1-MBH
- Figure 47 Potential dependence of the photocurrent of PS1-MBH
- Figure 48 SEIRA spectrum of the reconstitution process
- Figure 49 Stability of the surface-tethered hybrid complex
- Figure 50 Reconstituted membrane protein – investigated by SNIM
- Figure 51 Structural model of the CcO layer
- Figure 52 AFM image of reconstituted cytochrome c oxidase
- Figure 53 SEIRA spectra of CcO binding and DMPC reconstitution
- Figure 54 SNIM images of reconstituted cytochrome c oxidase
- Figure 55 Near-field scatter plots
- Figure 56 Near-field contour plots
- Figure 57 Improved model of the CcO layer
- Figure 58 Infrared absorption spectra of different *CrHydA1* states
- Figure 59 Infrared ATR spectra of *CrHydA1* during drying
- Figure 60 Infrared ATR spectra of the CO/CN region of *CrHydA1*
- Figure 61 SEIRA spectra of immobilized *CrHydA1*
- Figure 62 Potential-induced SEIDA spectrum of immobilized *CrHydA1*
- Figure S1 Overview of the sample changer
- Figure S2 Ground plate of the sample changer
- Figure S3 Rear panel of the sample changer
- Figure S4 Motor of the sample changer
- Figure S5 Slide rail for the sample holder

---

Figure S6	Slide rail for the sample holder
Figure S7	Sample holder
Figure S8	SEIRAS optics
Figure S9	SEIRA lid for the spectrometer chamber
Figure S10	Glove bag holder for the sample changer

### 10.3 List of Abbreviations

AFM	Atomic force microscopy
ANTA	N <sub>α</sub> ,N <sub>α</sub> -Bis(carboxymethyl)-L-lysine
ATR	Attenuated total reflection
BBP	1-(10-Mercaptodecyl)-1'-benzyl-4,4'-bipyridinium-dibromid
CpI	[FeFe]-Hydrogenase from <i>Clostridium pasteurianum</i>
CrHydA1	[FeFe]-Hydrogenase from <i>Chlamydomonas reinhardtii</i>
DDM	β-Dodecyl-maltoside
DMPC	Dimyristoyl-phosphatidylcholine
DTSP	Dithio-bis(succinimidyl propionate)
Fd	Ferredoxin
IRE	Internal reflection element
IR	Infrared
MBH	Membrane-bound hydrogenase from <i>Ralstonia eutropha</i>
MBH <sub>PsaE</sub>	Fusion protein of membrane-bound hydrogenase and PsaE
MPA	3-Mercaptopropionic acid
MUA	11-Mercaptoundecanoic acid
MV	Methylviologen
MV <sup>0</sup>	reduced form of MV
MV <sup>2+</sup>	oxidized form of MV
NHE	Normal hydrogen electrode
Ni-NTA	Nickel nitrilotriacetic acid

---

P680	Special pair of chlorophyll <i>a</i> molecules in photosystem II
P680 <sup>+</sup>	oxidized form of P680
PC	Plastocyanin
Ph	Pheophytin
PMS	N-Methylphenazonium methyl sulfate
PQ	Plastoquinone
PQH <sub>2</sub>	Plastoquinol
PS1	Photosystem I
PS1 <sub>ΔPsaE</sub>	PsaE-free photosystem I
PS1-MBH	Hybrid complex of photosystem I and membrane-bound hydrogenase
PS2	Photosystem II
PsaE	Subunit of photosystem I,
SAM	Self-assembled monolayer
SEIDA	Surface-enhanced infrared difference absorption
SEIDAS	Surface-enhanced infrared difference absorption spectroscopy
SEIRA	Surface-enhanced infrared absorption
SEIRAS	Surface-enhanced infrared absorption spectroscopy
SNIM	Scanning near-field infrared microscopy
SPR	Surface plasmon resonance
TSP	Thiosuccinimidyl propionate